Spring 1-1-2016

Optimization of GPS Interferometric Reflectometry for Remote Sensing

Qiang Chen
University of Colorado Boulder, qiang.chen@colorado.edu

Optimization of GPS Interferometric Reflectometry for Remote Sensing

by

Qiang Chen

B.S., Tsinghua University, 2008

M.S., Tsinghua University, 2011

A thesis submitted to the

Faculty of the Graduate School of the

University of Colorado in partial fulfillment

of the requirements for the degree of

Doctor of Philosophy

Department of Aerospace Engineering Sciences

2016

This thesis entitled:
Optimization of GPS Interferometric Reflectometry for Remote Sensing
written by Qiang Chen
has been approved for the Department of Aerospace Engineering Sciences

_____

Prof. Dennis Akos

_____

Prof. Eric Small

Date _____

The final copy of this thesis has been examined by the signatories, and we find that both the content and the form meet acceptable presentation standards of scholarly work in the above mentioned discipline.

Chen, Qiang (Ph.D., Aerospace Engineering Sciences)

Optimization of GPS Interferometric Reflectometry for Remote Sensing

Thesis directed by Prof. Dennis Akos

GPS Interferometric Reflectometry (GPS-IR), a passive microwave remote sensing technique utilizing GPS signal as a source of opportunity, characterizes the Earth's surface through a bistatic radar configuration. The key idea of GPS-IR is utilizing a ground-based antenna to coherently receive the direct, or line-of-sight (LOS), signal and the Earth's surface reflected signal simultaneously. The direct and reflected signals create an interference pattern of the Signal-to-Noise Ratio (SNR), which contains the information about the Earth's surface environment. GPS-IR has proven its utility in a variety of environmental remote sensing applications, including the measurements of near-surface soil moisture, coastal sea level, snow depth and snow water equivalent, and vegetation biophysical parameters.

A major approach of the GPS-IR technique is using the SNR data provided by the global network of the geodetic GPS stations deployed for tectonic and surveying applications. The geodetic GPS networks provide wide spatial coverage and have no additional cost for this capability expansion. However, the geodetic GPS instruments have intrinsic limitations: the geodetic-quality GPS antennas are designed to suppress the reflected signals, which is counter to the requirement of GPS-IR. As a result, it is desirable to refine and optimize the instrument and realize the full potential of the GPS-IR technique.

This dissertation first analyzes the signal characteristics of four available polarizations of the GPS signal, and then discusses how these characteristics are related to and can be used for remote sensing applications of GPS-IR. Two types of antennas, a half-wavelength dipole antenna and a patch antenna, are proposed and fabricated to utilize the desired polarizations. Four field experiments are conducted to assess the feasibility of the design criteria and the performance of the proposed antennas. Three experiments are focused on snow depth measurement. The Table

Mountain experiment data shows a more distinct interference pattern of SNR and yields a more precise snow depth retrieval. The Marshall experiment data reveals the effect of the underlying soil medium on snow depth retrievals, which benefits from the improved sensitivity of the dipole antenna to snow depth change. The experimental data of the third snow experiment conducted at a mountain-top location shows that a variant surface tilt angle can result in considerable retrieval errors of snow depth. An algorithm utilizing the estimated surface tilt angle is proposed to calibrate the retrieved snow depth. The calibration algorithm significantly improves the accuracy and precision of snow depth retrievals. The last experiment provides an opportunity to evaluate the dipole antenna as applied to the measurements of vegetation biophysical parameters and near-surface soil moisture. The normalized SNR amplitude shows a negatively linear relationship with *in situ* measurements of vegetation water content over a range of 0-6 kg/m^2, which is much greater than the range from the geodetic antenna data (0-1 kg/m^2). The normalized SNR amplitude also shows a positive linear relationship with the near-surface soil moisture measurements, indicating its potential as a soil moisture sensor.

Dedication

This dissertation is dedicated to my parents and wife, for their endless love, support, and encouragement.

Acknowledgements

First, I would like to express my deepest gratitude to my advisor and committee chair Prof. Dennis Akos for the continuous support of my Ph.D. research. His patience, knowledge, and guidance helped me in all the time of research. Without him, this dissertation cannot have been finished.

Besides my advisor, I would like to thank the rest of my committee: Prof. Eric Small, Prof. Kristine Larson, Prof. William Emery, and Dr. Valery Zavoronty, for their insightful input, guidance, and encouragement. Their expertise in the field of GPS-IR is invaluable to my research.

My sincere thanks also go to Dr. Staffan Backen, Dr. Tianxing Chu, Dr. Ningyan Guo, and Sara Hrbek, for their company during my time in the GNSS Lab. I would also like to thank Professor Jie Xu of University of Miami, Dr. Erin Griggs, and Dr. Hanzeng Li for reviewing my dissertation and providing insightful suggestions.

Contents

Chapter

Tables

Table

Figures

Figure

Chapter 1

Introduction

The Global Positioning System (GPS), developed by the United States Department of Defense, has been providing continuous, real-time, global-coverage, and all-weather timing, positioning, and navigation services since it was declared operational in 1993 (Misra and Enge, 2006). Almost at the same time, the GPS signal was recognized as a source of opportunity for the Earth's surface remote sensing applications using the GPS reflectometry (GPS-R) technique in a bistatic radar configuration. The European Space Agency (ESA) was the first to propose the use of the L-band signals broadcast by the GPS satellites in a bistatic radar configuration, which Hall and Cordey realized as an ocean scatterometer (Hall and Cordey, 1988). Marti-Neira (1993) proposed an altimeter system using GPS reflections from the ocean surface to measure the sea surface height. Then GPS-R was extended to other ocean and land surface remote sensing applications, such as sensing wind speed and wind direction of the ocean surface, soil moisture, and snow and ice thickness (Garrison and Katzberg, 1997; Zavorotny and Voronovich, 2000b; Komjathy et al., 2000a; Masters et al., 2004; Katzberg et al., 2006). In the past decade, the concept of satellite based navigation has extended from GPS to the Global Satellite Navigation System (GNSS), a multinational system that consists of other global or regional satellite navigation constellations. As a result, the concept of GPS-R has also evolved to GNSS Reflectometry (GNSS-R), which aims to utilize the new navigation signals from the emerging navigation satellite constellations.

A subset of GNSS-R is the GPS Interferometric Reflectometry (GPS-IR) technique, which was first proposed by Kavak et al. (1998) to measure the ground complex permittivity. The key idea

of GPS-IR is utilizing a single antenna to coherently receive the direct, or line-of-sight (LOS), signal and the surface reflected signal simultaneously. The direct and reflected signals create an interference pattern of the Signal-to-Noise Ratio (SNR), which contains information about the Earth's surface environment. Although extensive studies have been made to the model formulation and applications of GPS-IR, little research is focused on the optimization of the GPS-IR instrument (i.e. GPS antenna and receiver) to achieve the best possible performance. This dissertation analyzes the signal characteristics and summarizes the requirements on instrument design for several typical remote sensing applications. Four field experiments are conducted to explore and verify the performance of the proposed and developed antennas in various applications.

This chapter provides a brief review of the GNSS signals, focusing on the auto-correlation properties of the ranging code. The concepts and typical applications of GNSS-R and GPS-IR are also described, respectively. Their relationship and key differences are emphasized. This introduction concludes with a summary of contributions made to GPS-IR for remote sensing applications.

1.1 Introduction of Global Navigation Satellite System

Because of the great commercial and military values of satellite navigation, Russia, the European Union, and China are building or upgrading their own global satellite navigation systems, which are respectively known as GLObal NAvigation Satellite System (GLONASS), Galileo, and BeiDou. These three global navigation systems, together with the GPS, are collectively referred to as GNSS. GNSS also includes several local augmentation systems, including the Wide Area Augmentation System (WAAS) by the United States, the Quasi-Zenith Satellite System (QZSS) by Japan, and Indian Regional Navigation Satellite System (IRNSS) by India. In this section, the structures and properties of the GPS L1 course acquisition (C/A) code are shown here as a representative of all constellations because it is the most widely used civil signal in navigation and remote sensing. Most of the contents in this section are from Misra and Enge (2006) and Kaplan and Hegarty (2005).

The GPS satellites are continuously broadcasting navigation signals in orbit at an altitude of

approximately 20,200 km. Currently there are 32 GPS satellites distributed in six orbital planes at an inclination angle of 55°. To solve for the three-dimensional position and time, a GPS receiver needs to know the positions of and geometrical distances to at least four GPS satellites, which are all derived from the navigation signals. The navigation signals of GPS are comprised of three components: the carrier, the ranging code, and the navigation message bits. GPS satellites broadcast right-handed circularly polarized (RHCP) navigation signals in three L-band frequencies:

$$L1 : f_{L1} = 1575.42\ MHz,$$

$$L2 : f_{L2} = 1227.60\ MHz,$$

$$L5 : f_{L5} = 1176.45\ MHz$$

The C/A signal is modulated on the L1 frequency and available for all 32 GPS satellites. The new civilian navigation signals on L2 and L5 frequencies are only available for a subset of current GPS constellation. At the time of this dissertation (May 2016), there are 19 satellites broadcasting the L2 civilian signal (L2C) and 12 satellites broadcasting L5 civilian signal (National Coordination Office, 2016).

The C/A code is a pseudo-random noise (PRN) code and serves as the ranging code of L1 frequency. The modulo-2 addition of the C/A code and the navigation message bits is modulated in the L1 carrier in Binary Phase Shift Keying (BPSK). The C/A code has a period of 1 ms and consists of 1023 code chips; thus each C/A chip has a duration of approximately 0.978 μs. The most important property of C/A code is the auto-correlation function, defined as (Misra and Enge, 2006)

$$R(\tau) = \frac{1}{T_{code}} \int_0^{T_{code}} x^k(t) x^k(t-\tau)\ \mathrm{d}t \tag{1.1}$$

where τ is the code phase offset, $x^k(t)$ is the C/A code of the *k-th* GPS satellite, T_{code} is the length of C/A code in seconds. The shape of the auto-correlation function $R(\tau)$ is ideally triangular at $\tau = 0$ (see Figure 1.1), where $R(\tau)$ reaches it peak value, then linearly decreases to zero if the offset is larger than one chip. This characteristic makes C/A code (or PRN code) suitable for signal

synchronization: only when the local C/A code aligns with the received signal that will a peak value be obtained. Otherwise, the correlation values obtained appear noise-like. The navigation message bit rate is much slower than the ranging code chip rate. If the C/A code is synchronized, then the navigation message bits, which contain the GPS satellite's position and timing information, can be demodulated. Therefore, the synchronization of C/A code is an important aspect of the GPS receiver's PVT (Position, Velocity, Time) solution algorithm.

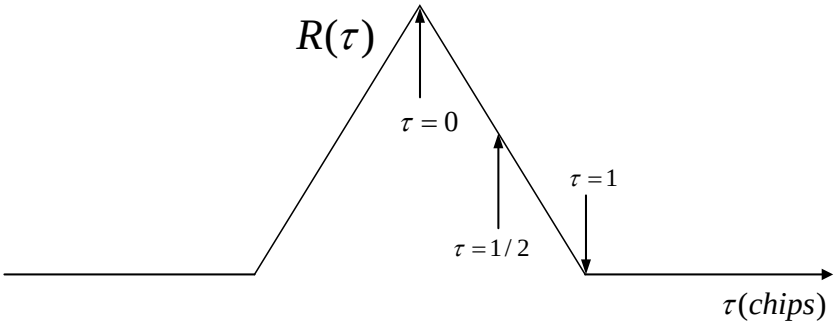

Figure 1.1: Ideal auto-correlation function for the GPS C/A code. In reality, the auto-correlation function is not perfectly triangular because of the limitation of the front-end bandwidth. Additionally, the auto-correlation value is not zero, but rather has small side peaks when $|\tau| > 1$ chip. However, these side peaks are much smaller than the main peak – at least 23 dB smaller – so side peaks are often ignored for simplicity in non-receiver design field.

For each GPS satellite in view, the GPS receiver maintains a local replica of its C/A code (designated as the Prompt code), which it continuously adjusts to synchronize the local code phase with the received signal. To facilitate the code synchronization, two more code replicas are utilized. One replica code maintains an advanced code phase with respect to the Prompt code (designated as the Early code), while the other replica's code phase lags behind the Prompt code (designated as the Late code). Generally the Early, Prompt, and Late codes are offset by a half code chip and correlate with the incoming signal. If the Prompt code is aligned with the incoming signal, the Prompt correlation value reaches a maximum, and the Early and Late correlation values are both approximately half of the Prompt correlation value. Otherwise, the Early and Late correlation values are not equal, and the code loop adjusts the code phases of the three replica codes until a balance is reached (see Figure 1.2).

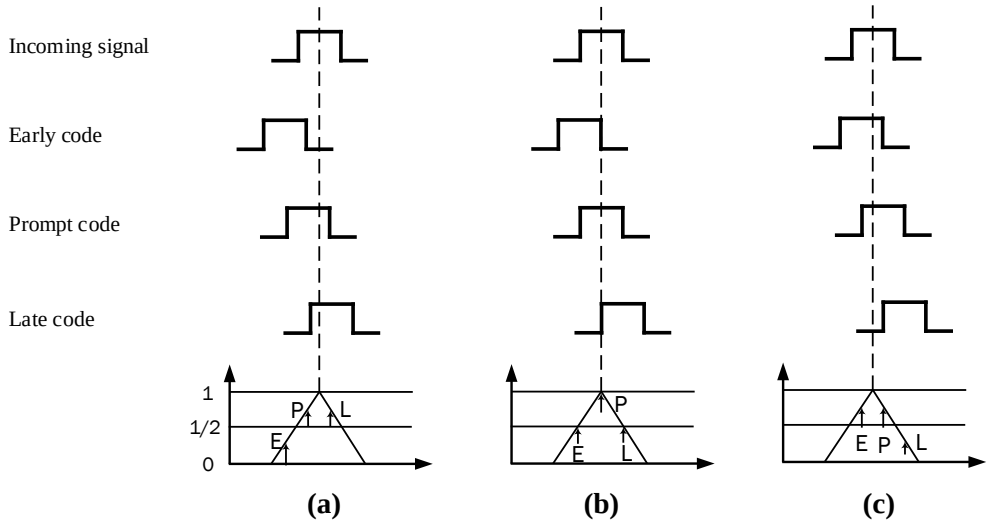

Figure 1.2: Three code correlation phases: (a) Prompt code 1/4-chip early, (b) Prompt code aligned, (c) Prompt code 1/4-chip late. When the Prompt code aligns with the incoming signal, the Early and Late correlation values are approximately the same; otherwise the code loop adjusts the code phases of the Early, Prompt, and Late correlators until they are aligned.

An accurate estimation of the carrier frequency and phase of the incoming signal is also required so that the carrier can be completely removed from the incoming signal. An inaccurate estimation of the carrier parameters would degrade the auto-correlation values of the three correlators. The correlation values of the Early, Prompt, and Late correlators are given by (Misra and Enge, 2006)

$$|V_P(\tau, \delta f)| = \sqrt{P} R(\tau) \left| sinc(\delta f T_{coh}) \right| + n_P \tag{1.2}$$

$$|V_E(\tau, \delta f)| = \sqrt{P} R(\tau - W/2) \left| sinc(\delta f T_{coh}) \right| + n_E \tag{1.3}$$

$$|V_L(\tau, \delta f)| = \sqrt{P} R(\tau + W/2) \left| sinc(\delta f T_{coh}) \right| + n_L \tag{1.4}$$

where $R(\tau)$ is the auto-correlation function defined in Eq. (1.1) and τ is the code phase offset between the incoming signal and the local Prompt code, δf is the frequency offset between the incoming signal and the local carrier frequency, P is the signal power, W is the distance in chips between the Early and Late correlators, n_P, n_E, and n_L are noise terms, which are Rayleigh distributed if the signal component does not exist, or Rice distributed if the signal component exists. The code and carrier loops minimize the estimation errors of the code phase and carrier

frequency/phase by adjusting the local code phases and carrier frequencies.

1.2 GNSS Reflectometry

GNSS-R, a passive microwave remote sensing technique, characterizes the Earth's surface through a bistatic radar configuration. Bistatic radar means that the transmitting antenna and the receiving antenna are not co-located, as opposed to a typical monostatic radar configuration. GNSS-R utilizes two radio-links: the GPS signal that propagates through the atmosphere and arrives at the antenna from the upper hemisphere, referred to as the direct radio link; and the signal that is reflected off the Earth's surface onto the bottom hemisphere of the antenna, referred to as the reflected radio link. The GNSS-R technique utilizes a dual-antenna configuration to receive the direct and scattered signals respectively; a zenith-looking RHCP antenna receives the direct signal while a nadir-looking left-handed circularly polarized (LHCP) antenna receives the reflected signal. The antenna and receiver can be airborne, space-borne, or ground-based at a relatively high altitude above the Earth's surface (see Figure 1.3).

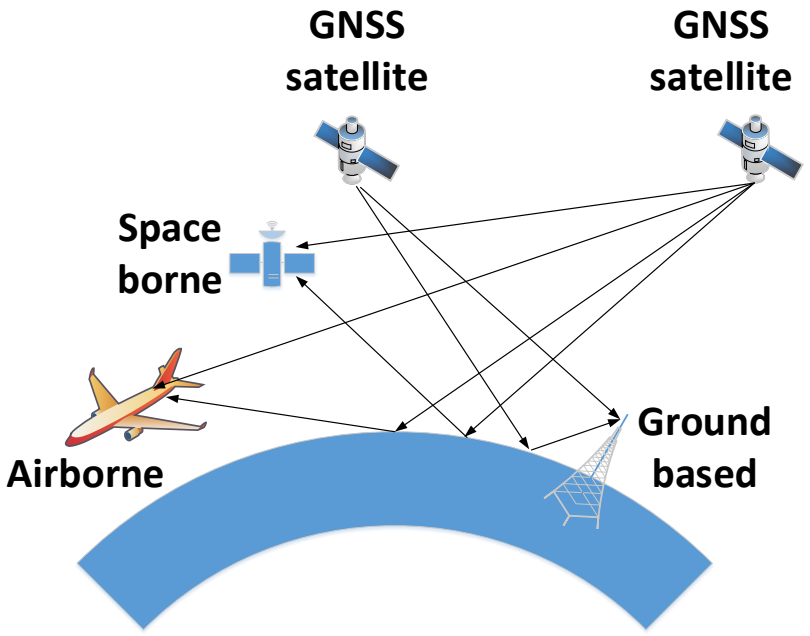

Figure 1.3: GNSS-R: the airborne, space-borne, and ground-based GNSS receivers receive the direct signal and the Earth's surface reflected signal.

If the Earth's surface is smooth, the nadir-looking antenna only collects the signal reflected from the specular reflection point. In reality, the nadir-looking antenna collects the reflected signal from an enlarged area surrounding the specular reflection point, known as the glistening zone, because of the roughness of the Earth's surface. The size of the glistening zone depends on the bistatic geometry and surface roughness. The observable of GNSS-R is the cross-correlation waveform or delay maps (DM). The DM shows a full description of the cross-correlation waveform by displaying the correlation results between the reflected signal and the local replicas at different delays using dozens of correlators. The direct signal is used to give the receiver position information as well as the reference code phase and carrier frequency. The cross-correlation waveform is no longer an ideal triangle, but the trailing edge decays at a slower slope than the leading edge. Several Earth's surface characteristics can be derived from the cross-correlation waveform (see Figure 1.4). More detailed discussion of the GNSS-R technique is provided in Jin and Komjathy (2010), Jin et al. (2011), and Cardellach et al. (2011).

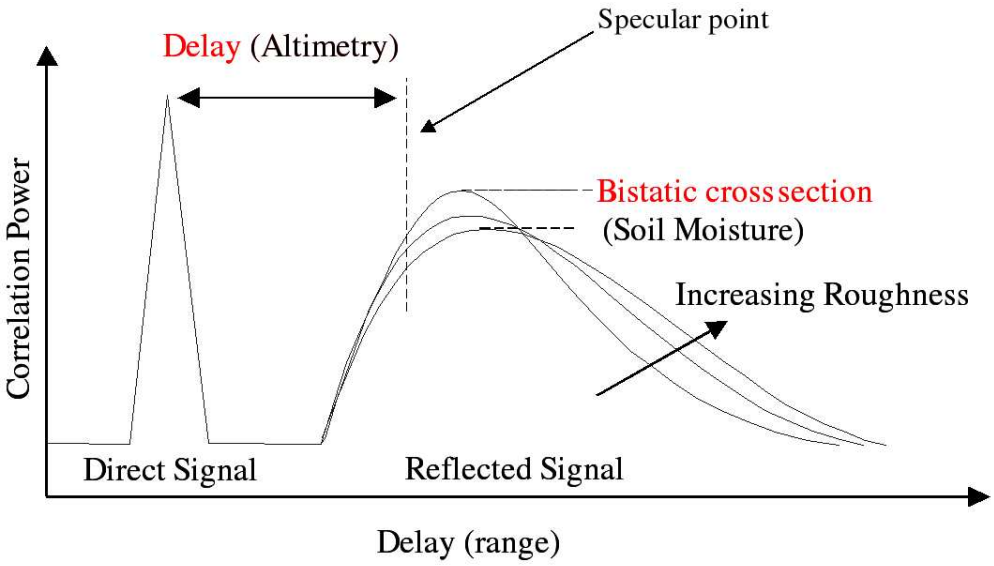

Figure 1.4: Cross-correlation waveform of GNSS-R: the characteristics of the cross-correlation waveform (code delay, reflection power, slope of trailing edge) are related to the Earth's surface parameters (surface height, soil moisture, surface roughness). Image courtesy of D. Masters (Masters et al., 2004).

The applications of GNSS-R are categorized as follows:

(1) Ocean altimetry

As mentioned previously, one of the first attempts of GNSS-R was an ocean altimetry mission proposed by Marti-Neira (1993), which was subsequently followed by other altimetric missions and experiments (Ruffini et al., 2004; Soulat et al., 2004; Alonso-Arroyo et al., 2015). Ocean altimetry aims to resolve the vertical distance between the antenna and the specular reflection point with respect to a reference ellipsoid or geoid. The difference between the propagation distances of the direct and reflected signals can be measured by the delay of code in the reflected signal with respect to the direct link. The range difference can be mapped to the vertical distance using the geometry. When compared to the conventional space-borne radar altimetry, GNSS-R has the advantages of high temporal and spatial resolution (Jin and Najibi, 2014), and thus serves as a good complement to traditional altimetric measurements.

(2) Ocean wind and roughness

The first attempts of GNSS-R, as applied to ocean wind and roughness, were made by Garrison and Katzberg (Garrison and Katzberg, 1997; Garrison et al., 1998, 2002). The shape of the cross-correlation waveform, primarily the trailing edge, is dependent on the roughness of the ocean surface, which further relates to the surface wind speed and direction parameters. Numerous experiments were carried out for ocean roughness and wind direction retrievals (Lin et al., 1999; Komjathy et al., 2000b, 2004; Germain et al., 2004; Gleason et al., 2005). In Komjathy et al. (2004), the retrieved wind speed measurements using GNSS-R showed an agreement of better than 2 m/s with the independent measurements made by the TOPEX/Poseidon altimetry satellite and nearby balloon. The wind direction measurements also agreed with the results obtained from buoys.

(3) Soil moisture

Zavorotny and Voronovich (2000a) extended the scattering model developed for ocean sur-

face remote sensing to land surface applications, aiming for soil moisture retrievals. The SNR or the cross-correlation waveform peak served as an indicator of the reflection power in the land surface soil moisture applications. The reflection power is sensitive to the dielectric property of the land surface, which is further determined by the volumetric soil moisture. L-band is regarded as the optimal frequency band for near-surface soil moisture extraction, primarily because its contribution/penetration depth is less than 5 cm. Masters and Katzberg conducted the first soil moisture oriented GNSS-R experiment, known as Soil Moisture Experiment 2002 (SMEX02), where the experimental results showed that there was a correlation between the GPS reflectivity and the top 1-cm of soil moisture data (Masters et al., 2004; Katzberg et al., 2006). Egido et al. (2012, 2014) proposed a polarimetric observable, which was defined as the ratio of the LHCP power to the RHCP power, to measure the soil moisture. The primary advantage of the polarimetric observable was that it excluded the effect of soil roughness variations on the soil moisture retrieval provided that the surface roughness was below a threshold of 3.0 cm.

(4) Ice and snow

Komjathy et al. (2000a) proposed to use reflection power of GPS signals to infer sea ice conditions. There was a strong relationship between the reflection power and back-scattered RADARSAT data. The behaviour of the reflected power indicated the potential of sensing ice conditions, including ice composition, density, temperature, and salinity, among other characteristics. Cardellach et al. (2012) investigated the application of GNSS-R to dry snow sub-structure characterization in the Antarctic area, using a lag-hologram observable. The experimental results showed that the penetration depth of GPS L-band signals can be as large as 200-300 m.

1.3 GPS Interferometric Reflectometry

GPS Interferometric Reflectometry (GPS-IR) has stemmed from GNSS-R and has been applied to a variety of remote sensing applications. The most distinct difference between GPS-IR and conventional GNSS-R is that GPS-IR uses a single antenna to receive the direct and reflected signals simultaneously (see Figure 1.5). Rather than using the cross-correlation waveform, GPS-IR utilizes the interference pattern of the SNR as an observable. The antenna height is usually several meters above the reflecting surface, and thus the sensing area is not the glistening zone but the much smaller first Fresnel zone (Katzberg et al., 2006).

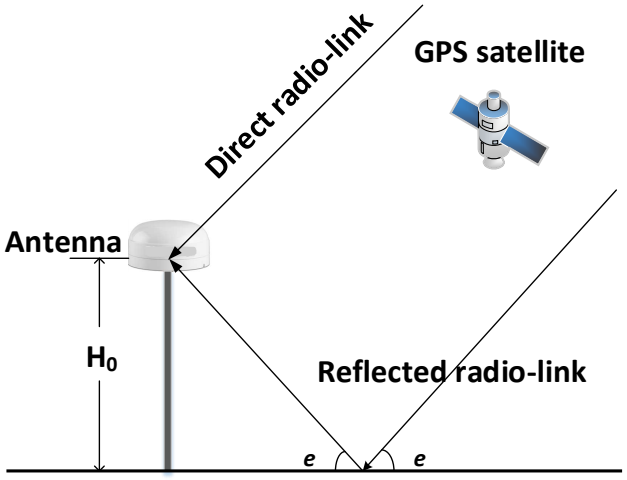

Figure 1.5: Geometry of GPS-IR. H_0 is the antenna's apparent height above the reflector, and e is the elevation angle of the GPS satellite. The antenna receives the direct and coherently reflected signals simultaneously. As the GPS satellite ascends or descends, the propagation difference between direct and reflected signals varies, resulting in an interference pattern of the SNR.

GPS-IR was first proposed by Kavak et al. (1998) for the measurement of land surface permittivity, but was not investigated extensively until recently. From 2008, Larson, Small, Zavorotny et al. proposed to use the SNR data from the global network of geodetic GPS stations deployed for tectonic and surveying applications to infer the Earth's surface environmental parameters, such as snow depth (Larson et al., 2009; Larson and Nievinski, 2013; Najibi and Jin, 2013), near-surface soil moisture (Zavorotny et al., 2010; Larson et al., 2010; Larson and Small, 2014), coastal sea level (Lof-

gren et al., 2011a,b), and vegetation biophysical parameters (Small et al., 2010; Rodriguez-Alvarez et al., 2012b; Larson et al., 2013; Small et al., 2014; Chew et al., 2015). The widely distributed geodetic networks (e.g. Continuously Operating Reference Station (CORS) operated by National Geodetic Survey (NGS) and the EarthScope Plate Boundary Observatory (PBO) operated by National Science Foundation (NSF)) provide wide spatial coverage, and have no additional cost for this remote sensing capability expansion.

Instead of using geodetic antennas, some research groups utilized specifically designed antennas optimized for the corresponding remote sensing applications. Rodriguez-Alvarez et al. (2009, 2011a,b) proposed a vertically-polarized antenna for soil moisture measurement, and then extended its application to other geophysical parameters (e.g. surface topography, vegetation height, snow thickness). Jacobson (2008, 2010a,b) conducted several experiments aiming at snow thickness and snow water equivalent (SWE) measurements utilizing a tilted, horizon-looking geodetic GPS antenna. A nonlinear least-square method was used to solve for the snow thickness and SWE. However, the method required a priori knowledge of the environment and it might converge to different solutions depending on the accuracy of the a priori knowledge.

1.4 Summary of Research

The dissertation contributes to the field of GPS-IR by addressing the following key questions to the instrument optimization: (1) What kinds of signals (polarizations) and what characteristics are beneficial to the GPS-IR remote sensing? (2) What types of instrument can provide the desired characteristics? (3) Does field experiment data support the analysis and proposed instrument design?

1.4.1 Research Motivation

As mentioned in Section 1.3, a majority of the GPS-IR applications are utilizing geodetic-quality GPS antennas and receivers to make use of the existing geodetic GPS networks. Although the geodetic networks have the advantages of wide spatial coverage and zero additional hardware

cost, they are not optimal for remote sensing of GPS-IR. The geodetic GPS antennas are designed to suppress the reflected signal (known as multipath in GPS precise positioning). Figure 1.6 depicts the gain pattern of a typical geodetic GNSS antenna. Generally the RHCP gain of the antenna is several orders of magnitude larger than the LHCP gain at high elevation angles, which aims to suppress the reflected signal. Moreover, the RHCP gain is optimized for the zenith direction and minimized for the bottom hemisphere, which is another design feature that suppresses the ground reflected signal. The limitations of the geodetic antennas are detailed in Zavorotny et al. (2010).

To overcome the limitations of the geodetic GPS antenna, researchers have tried to utilize specifically designed antennas for various GPS-IR remote sensing applications. Rodriguez-Alvarez et al. proposed to utilize the vertically-polarized components of both the direct and reflected signals to measure the near-surface soil moisture (Rodriguez-Alvarez et al., 2009, 2011a,b). The vertical polarization has an important feature known as the Brewster's angle: the angle at which the incident electromagnetic wave completely penetrates the bottom media and is not reflected at all. Although in reality, the reflection power cannot be zero because of the inhomogeneities and roughness of the soil; the notch in the SNR interference pattern is still detectable. This approach was later extended to other land geophysical remote sensing applications, such as topography and vegetation height (Rodriguez-Alvarez et al., 2011a,b).

The utilization of the vertical polarization sheds insight on the field of instrument optimization for GPS-IR technique. Prior to this work, no systematic analysis was performed to characterize the various polarizations and their potential applications. It is desirable to investigate the characteristics and potentials of the various polarizations, which also provides guidance for the instrument design. With the selected polarization and specifically designed instrument, it is desirable to investigate how much performance improvement can be achieved by utilizing these optimized instrument. In addition, the optimized instrument might extend the GPS-IR technique to new applications that are not achievable by a geodetic-quality instrument. In short, the research motivation of this dissertation is to realize the full potential of GPS-IR through the use of a specially designed, optimized instrument.

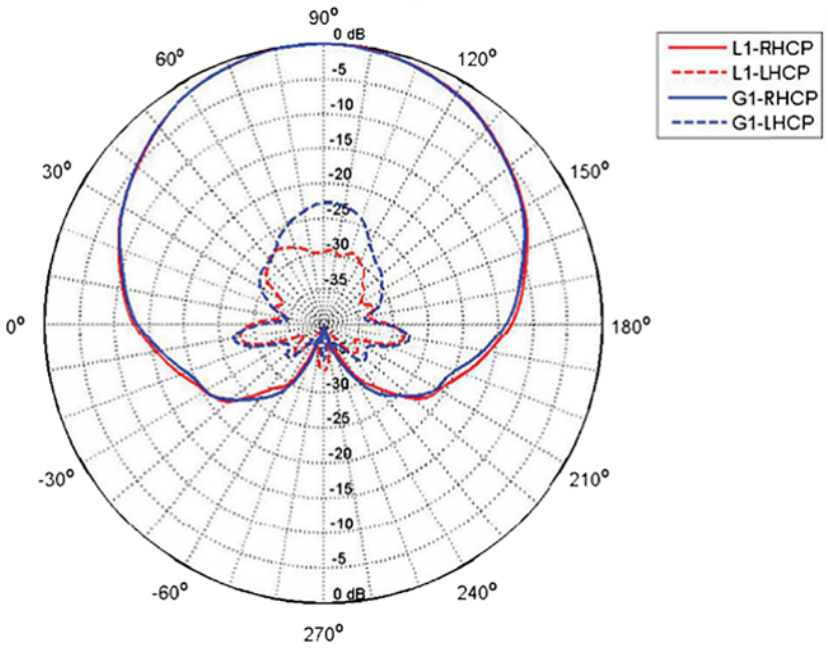

Figure 1.6: Novatel GPS-702-GG pinwheel antenna gain pattern (http://www.navtechgps.com/assets/). The solid red and blue curves are the RHCP gains of GPS L1 (1575.42 MHz) and GLONASS G1 (1602 MHz), respectively. The dashed red and blue curves are the LHCP gains of L1 and G1, respectively.

1.4.2 Research Contributions

The research contributions of this dissertation are summarized as follows:

(1) The original forward model of GPS-IR developed for a geodetic GPS antenna is simplified to accommodate an antenna with a single dominant polarization. With the simplified model, the signal characteristics of various polarizations and their potential applications in remote sensing are discussed and summarized. In addition, the requirements on antenna design are discussed (Chapter 2).

(2) Two linearly-polarized antenna types (dipole antenna and patch antenna) are designed and fabricated for a series of GPS-IR experiments. The proposed antennas can be configured to work with either horizontal polarization or vertical polarization, and thus provide the flexibility of assessing the performance of different polarizations in various remote sensing

applications (Chapter 3).

(3) A two-day experiment was conducted on the Table Mountain plateau aiming to assess the performance of the dipole antenna for measurement of snow depth. The dipole antenna was configured to work with horizontal polarization. This is the first GPS-IR experiment to utilize horizontal polarization for snow depth measurement. The SNR data collected with the dipole antenna shows a more distinct interference pattern than the geodetic SNR, especially at high elevation angles. Therefore, the footprint of the sensing area is extended, and higher precision is achieved for the reflector height and snow depth retrievals (Chapter 4).

(4) A longstanding experiment was conducted in the Marshall Field covering the entire snow season of the 2013-2014 water year. This experiment provides the opportunity to comprehensively evaluate the performance of the dipole antenna for measurement of snow depth. In general, the GPS-derived snow depth and *in situ* measurements match up well. However, anomalies in snow depth measurements are occasionally observed. A dual-interface model is proposed to account for the measurement anomalies. The distribution of the experimental results matches well with theoretical simulations. The experimental data and the proposed model provide insight into the propagation of the electromagnetic wave in layered medium (Chapter 5).

(5) A mountain-top experiment was conducted to evaluate the feasibility of the GPS-IR techniques as applied to snow depth measurement in an alpine environment. A horizontally polarized patch antenna was used in the experiment to suppress undesired reflections from the building structure. The GPS-IR model is adapted to include the slope angle of the terrain, which is then used to calibrate the retrieved reflector height. The model is used to process data collected from alpine areas. The calibrated snow depth agree well with the *in situ* measurements with a RMSE of 14 cm(Chapter 6).

(6) A vegetation experiment was carried out at an alfalfa farm to evaluate the performance of various polarizations. The experiment results show that with the optimized dipole antenna, the measurement range of the vegetation water content is greatly extended from 0-1.0 kg/m^2 to 0-6 kg/m^2 (Chapter 7).

Chapter 2

Signal Characteristic and Polarization Selection

This chapter discusses the forward model of SNR and the parameter retrieval algorithms. The Fresnel reflection coefficient, especially its relationship with the GPS-IR metrics, is emphasized. Two reflection models and the reflection coefficients for various polarizations are presented. Finally, the signal characteristics of various polarizations and their potential applications in GPS-IR are discussed. It is concluded that the horizontal polarization is suitable for all considered applications. This chapter serves as the theoretical foundation for the antenna design described in Chapter 3.

2.1 GPS-IR Forward Model

As stated in Chapter 1, the SNR is the primary observable used in GPS-IR technique to retrieve the Earth's surface environmental parameters. The forward model of GPS SNR is discussed in detail elsewhere (Zavorotny et al., 2003; Nievinski and Larson, 2014a,b,c,d). However, previous studies are mainly focusing on geodetic-quality GPS antennas. Although it is natural to extend the theory and formulations developed from the geodetic-quality GPS antenna to other antenna types, some modifications have to be adopted. As illustrated in Figure 1.6, the geodetic-quality GPS antenna has comparable RHCP and LHCP gains at low elevation angles, so both co-polarized (RHCP) and cross-polarized (LHCP) reflections have to be accounted for in the formulation of the forward model. In addition, the phase responses to RHCP and LHCP electromagnetic (EM) waves of the geodetic-quality antenna are generally not the same, but have a phase difference of approximately 90° (Zavorotny et al., 2010). As a result, the effects of the surface reflection and

antenna response on the reflected wave cannot be isolated.

SNR is defined as the ratio of the received signal power P_s to the noise power P_n, and serves as an indicator of the signal strength. In a GPS receiver, the Carrier-to-Noise density Ratio (C/N_0), which is defined as the ratio of signal power P_s to the noise power spectral density N_0, is more often used to exclude the effect of the noise bandwidth that is receiver dependent. The relationship between SNR and C/N_0 is described by:

$$SNR = \frac{C/N_0}{B_n} \tag{2.1}$$

where B_n is the noise bandwidth in the GPS receiver. In fact, there is only a constant bias between P_s and C/N_0 in decibels under the assumption that N_0 and B_n are constant during the observation period. In the following discussion, we do not discriminate between P_s, SNR, or C/N_0, and use SNR as the observable of GPS-IR.

Considering the reflected signal, the composite SNR is formulated as

$$SNR = \frac{P_d + P_r + 2\sqrt{P_d P_r}\cos\phi_i}{P_n} \tag{2.2}$$

where P_d and P_r are the power of the direct and reflected signals respectively, and ϕ_i is the interference phase that amounts to the excess of the reflected wave with respect to the direct wave.

The change of ϕ_i determines the positions of the maxima and minima of the interference pattern of the observed SNR, and the modulation amplitude (null depth) is determined by the factor $2\sqrt{P_d P_r}$. For a geodetic-quality GPS antenna, the interference phase ϕ_i is formulated as

$$\phi_i = \phi_g - \Phi_d^R + \phi_X \tag{2.3}$$

where the first term

$$\phi_g = \frac{4\pi h \sin e}{\lambda} \tag{2.4}$$

is the interference phase introduced by the geometric propagation difference between the reflected and direct signals (see Figure 2.1), h is the geometric antenna height above the reflecting surface, λ is the wave length of the electromagnetic wave (L1 = 1575.42 MHz, λ_{L1} = 19.0 cm; L2 = 1227.6

MHz, $\lambda_{L2} = 24.4$ cm), and e is the elevation angle of the GPS satellite. The second term Φ_d^R is the phase response of the geodetic-quality GPS antenna to the direct GPS signal. The superscript R indicates RHCP and the subscript d indicates the direct signal. The third term $\phi_X = arg(X)$ accounts for the surface and antenna effects on the reflections, where X is the complex sum of the co-polarized and cross-polarized electric field vectors incorporating the antenna's phase response:

$$X = R_S\sqrt{G_r^R}\exp\left(j\Phi_r^R\right) + R_X\sqrt{G_r^L}\exp\left(j\Phi_r^L\right) \tag{2.5}$$

where R_S is the Fresnel reflection coefficient for RHCP (co-polarization), R_X is the Fresnel reflection coefficient for LHCP (cross-polarization), j is the imaginary unit, G_r^R is the amplitude response and Φ_r^R is the phase response of the antenna to the RHCP component in the reflected electromagnetic wave, G_r^L is the amplitude response and Φ_r^L is the phase response of the antenna to the LHCP component in the reflected electromagnetic wave.

If we assume that the receiving antenna is working on a single dominant polarization, then the polarization notation can be discarded and X is simplified to:

$$X = R\sqrt{G_r}\exp\left(j\Phi_r\right) \tag{2.6}$$

In this situation, the interference phase ϕ_i is simplified to

$$\phi_i = \phi_g + \phi_r + \phi_a \tag{2.7}$$

where $\phi_r = \arg\left(R\right)$ is the phase of the complex Fresnel reflection coefficient, $\phi_a = \Phi_r - \Phi_d$ reflects the possible different phase responses of the antenna at different elevation angles.

Substituting $x = \sin e$, $f_m = 2h/\lambda$, and Eq. (2.7) into Eq. (2.2), the SNR is

$$SNR = \left(P_d + P_r + 2\sqrt{P_d P_r}\cos(2\pi f_m x + \phi_r + \phi_a)\right)/P_n \tag{2.8}$$

Several algorithms can be used to estimate the frequency f_m (Alonso-Arroyo et al., 2015), among which the Lomb-Scargle Periodogram (LSP) is the simplest and most widely used (Lomb, 1976). The LSP is similar to the Fast Fourier Transform (FFT) but does not require evenly spaced sampling. The estimated f_m (denoted as f_{eff}) and the reflector height are related by

$$h_{eff} = \frac{\lambda f_{eff}}{2} \tag{2.9}$$

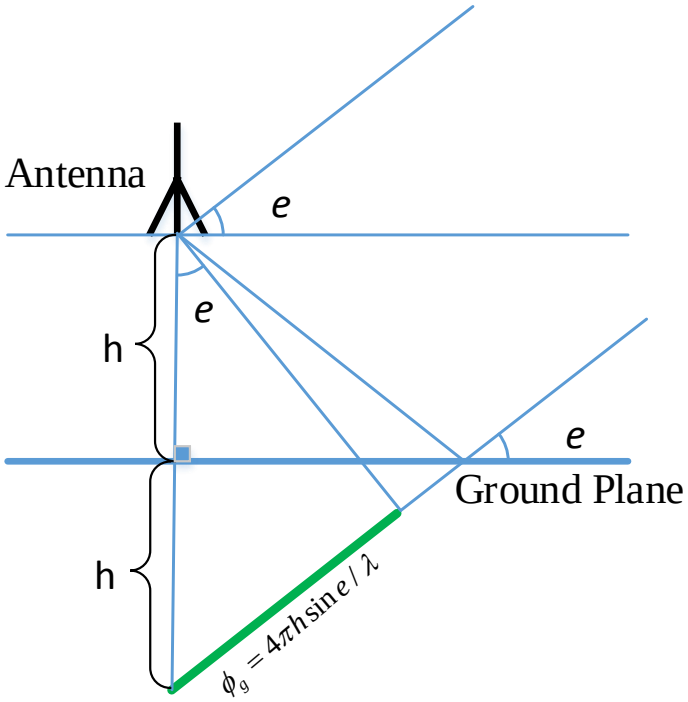

Figure 2.1: The geometric path difference between direct and reflected signals is $2\pi h \sin e$, and thus the phase difference $\phi_g = 4\pi h \sin e/\lambda$. h is the geometric antenna height above reflector (assumed to be horizon), e is the elevation angle of the GPS satellite.

For the geodetic-quality GPS antenna, the retrieved reflector height h_{eff} is not always equal to the geometric reflector height h and is referred to as the effective reflector height (Larson et al., 2010; Wan et al., 2015). It is demonstrated that h_{eff}, with a geodetic-quality GPS antenna, can have a 0-5 cm offset to the geometric reflector height h for bare soil conditions depending on the soil moisture level (Zavorotny et al., 2003; Chew et al., 2014). If the change of the interference phase is completely due to the movement of GPS satellite, i.e. $\Delta\phi_i = \Delta\phi_g$, then the retrieved reflector height is equal to the geometric reflector height, i.e. $h_{eff} = h$. If ϕ_r is not constant but changing with elevation angle e, then a reflector height estimation bias $\delta h = h_{eff} - h$ is brought in (assume $\phi_a = 0$) and formulated by

$$\delta h = \frac{\lambda}{4\pi}\frac{d\phi_r}{dx} \tag{2.10}$$

For the geometry-driven applications (e.g. snow depth and water level), it is essential to keep ϕ_r and ϕ_a constant so that the estimated h_{eff} is unbiased. As will be illustrated later, the error term δh is non-negligible if the receiving antenna is vertically polarized.

For the non-geometry-driven applications (e.g. near surface soil moisture and vegetation biophysical parameters), the amplitude of the interference pattern plays an important role in corresponding environmental parameters retrievals. The modulation amplitude A is formulated by

$$A = 2\,|RS|\,\sqrt{G(e)G(-e)}P_{d,iso}/P_n \tag{2.11}$$

where $P_{d,iso}$ is the received power of the direct GPS signal by an isotropic antenna (about -160 dBW above the Earth's surface), $G(e)$ is the gain pattern, i.e. the magnitude of the complex radiation pattern, of the receiving antenna at e. For a surface reflector, S is the attenuation factor caused by the surface roughness and can be computed by (Beckmann and Spizzichino, 1987)

$$S = e^{-2k^2s^2\sin^2 e} \tag{2.12}$$

where $k = 2\pi/\lambda$ is the wave number in free space; s is the standard deviation of ground surface height. The modulation bias of the interference pattern, i.e. $P_d + P_r$, is usually ignored or removed using a low-order polynomial fit because it does not contain the desired environmental information. It is worth noting that P_r in the bias term consists of both the coherent component and the non-coherent component of the reflected signal, while P_r only contributes the coherent component to the modulation amplitude A.

Both the reflection coefficient R and antenna gain $G(e)$ are polarization dependent. Typically a geodetic-quality GPS antenna works on RHCP, and the LHCP gain is at least 15 dB smaller for high elevation angles (Zavorotny et al., 2010). However, at low elevation angles the LHCP gain is comparable or even exceeds the RHCP gain. In fact, the discrepancy between h_{eff} and h is primarily due to the non-negligible LHCP gain at low elevation angles. Although P_d and P_r are affected by various factors (e.g. R, S, and $G(e)$), the difficulty of retrieving f_{eff} (and thus h_{eff}) is not obviously increased because their changes are much slower than those caused by the change of interference phase ϕ_i.

2.2 Reflections: Single-interface Model and Dual-interface Model

As demonstrated previously, the complex Fresnel reflection coefficient R affects both the interference phase ϕ_i and the modulation amplitude A. In this section, we present the characteristics of reflection coefficients for various polarizations and environmental conditions. Two reflection models, the single-interface model and the dual-interface model, are presented here and utilized to calculate the Fresnel reflection coefficients for different applications.

2.2.1 Single-interface Model

As shown in Figure 2.2, the single-interface model assumes two media layers, the top medium and bottom medium, each of which occupies one entire half space. The single-interface model is the simplest reflection model but is effective in many environmental sensing applications. The horizontal, vertical, RHCP to RHCP, and RHCP to LHCP reflection coefficients are formulated by (Balanis, 2012)

$$R_h = \left(\cos\theta_i - \sqrt{\epsilon_r - \sin^2\theta_i}\right) / \left(\cos\theta_i + \sqrt{\epsilon_r - \sin^2\theta_i}\right) \tag{2.13}$$

$$R_v = \left(\epsilon_r\cos\theta_i - \sqrt{\epsilon_r - \sin^2\theta_i}\right) / \left(\epsilon_r\cos\theta_i + \sqrt{\epsilon_r - \sin^2\theta_i}\right) \tag{2.14}$$

$$R_{rr} = \frac{1}{2}\left(R_v + R_h\right) \tag{2.15}$$

$$R_{rl} = \frac{1}{2}\left(R_v - R_h\right) \tag{2.16}$$

where θ_i is the angle of incidence, ϵ_r is the complex permittivity of the bottom medium and the top medium is air ($\epsilon_{r,air} = 1$).

The reflection coefficients of four polarizations with the single-interface model for wet soil ($\epsilon_r = 12 + 1.5j$), dry soil ($\epsilon_r = 4.5 + 0.5j$), and snow ($\epsilon_r = 1.5 + 0.001j$) together with the reflector height bias δh calculated using Eq. (2.10) are illustrated in Figure 2.3. From Figure 2.3, R_h has the following characteristics:

- It has a large reflection coefficient magnitude, which is desired for distinct interference pattern (large modulation amplitude A). The magnitude of the horizontal reflection coef-

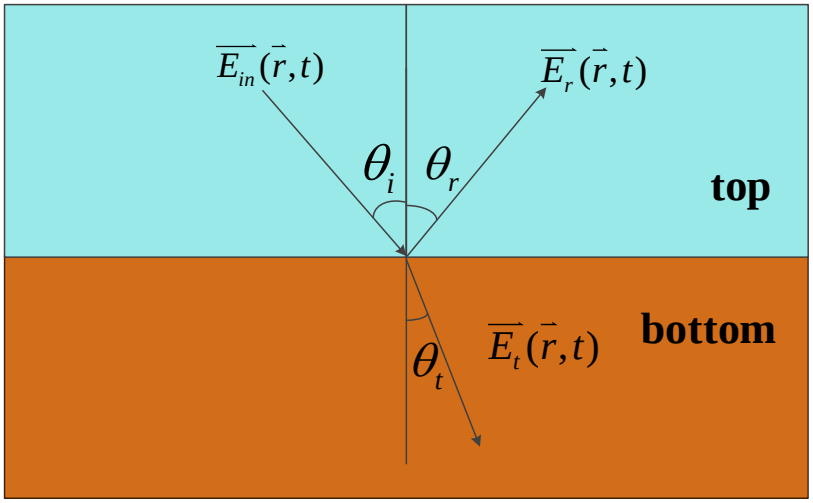

Figure 2.2: Single-interface model. The top medium (air) and bottom medium (soil, snow, water, etc) occupy the entire half space, respectively. $\vec{E}_{in}$ is the incident EM wave, $\vec{E}_r$ is the reflected EM wave, $\vec{E}_t$ is the refracted EM wave.

ficient $|R_h|$ decreases as elevation angle increases. The decreasing curve is determined by the permittivity of the bottom medium ϵ_r.

- The phase of the horizontal reflection coefficient $arg(R_h)$ changes very slightly (within 5°) as the elevation angle increases. As a result, the retrieved reflector height bias δh is just several mm which can be neglected in most environmental remote sensing applications.

The vertical reflection coefficient R_v has the following characteristics:

- There is a minimum in the curve of $|R_v|$. The magnitude approaches to zero around a particular angle, which is referred to as Brewster's angle. The position of the Brewster's angle is determined by the permittivity of the bottom medium.

- The reflection coefficient phase of vertical polarization $arg(R_v)$ changes sharply around the Brewster's angle (almost 180°). This characteristic results in a considerable retrieved reflector height bias δh.

The reflection coefficient of RHC to RHC polarization R_{rr} has the following characteristics:

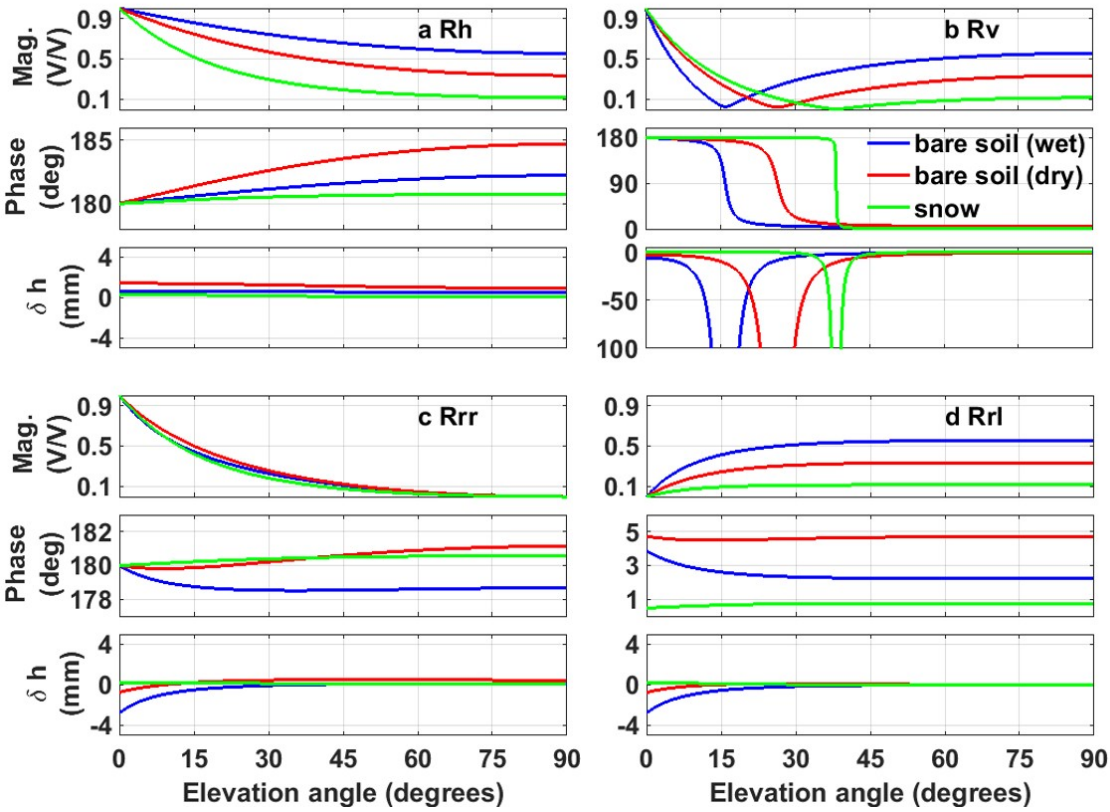

Figure 2.3: Fresnel reflection coefficients of (a) horizontal, (b) vertical, (c) RHC to RHC, (d) RHC to LHC polarizations. For each polarization, the reflection coefficients are calculated for three kinds of media: wet soil, dry soil, and snow. For each plot, the top and middle panels are the magnitude and phase of the reflection coefficient. The bottom panel is the retrieved reflector height bias δh as a result of the change of the reflection coefficient phase.

- Like $|R_h|$, the magnitude $|R_{rr}|$ decreases as the elevation angle increases, but more rapidly. The decreasing curve is almost not affected by the permittivity of the bottom medium.

- The reflection coefficient phase of RHC to RHC polarization $arg(R_{rr})$ also changes very slightly (within 2°) as elevation angle increases. The retrieved reflector height bias δh is also negligible.

The reflection coefficient of RHC to LHC polarization R_{rl} has the following characteristics:

- The magnitude $|R_{rl}|$ increases as the elevation angle increases. The rising curve is determined by the permittivity of the bottom medium.

- The reflection coefficient phase of RHC to LHC polarization $arg(R_{rl})$ also changes very slightly (within 5°) as elevation angle increases. The retrieved reflector height bias δh is also negligible.

2.2.2 Dual-interface Model

The single-interface model might not be accurate enough to describe the actual environmental conditions for some applications, e.g. vegetation biophysical parameters. The derived permittivity of vegetation canopy is smaller than 1.1, which is not large enough to make the vegetation canopy overshadow the effect of the underlying soil. The effect of soil has to be taken into account in vegetation sensing applications. Here a dual-interface model, which is adapted from the single-interface model by adding another layer beneath the bottom medium, is presented here (see Figure 2.4).

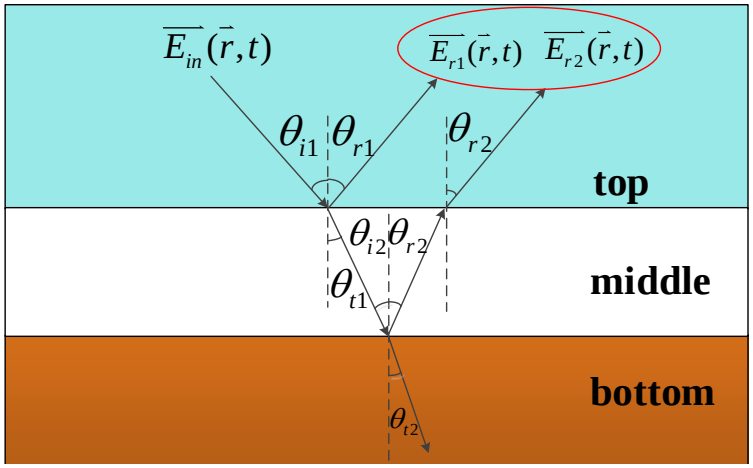

Figure 2.4: Dual-interface model. Two leading reflections occur at the top-middle and middle-bottom interfaces. In the top half space, the two reflected waves add up coherently.

From Figure 2.4, the top and bottom medium occupy the entire half space and have a medium layer in the middle. If we only account for the leading two reflections occurring at the top-middle and middle-bottom interfaces and neglect the high-order bounces between the interfaces, then the two bounced back electromagnetic waves, $\vec{E}_{r1}(\vec{r},t)$ and $\vec{E}_{r2}(\vec{r},t)$, add up coherently and result in a

composite reflection coefficient, which is defined as

$$R^x_{comp} = \frac{\vec{E}_{r1}(\vec{r},t) + \vec{E}_{r2}(\vec{r},t)}{\vec{E}_{in}(\vec{r},t)} \tag{2.17}$$

where $\vec{E}_{in}(\vec{r},t)$ is the incident electromagnetic wave, and x indicates the polarization. The composite reflection coefficient is computed by (Born and Wolf, 1999)

$$R^x_{comp} = \frac{R^x_{(1)} + R^x_{(2)}Q}{1 + R^x_{(1)}R^x_{(2)}Q} \tag{2.18}$$

where the term

$$R^x_{(1)} = \begin{cases} \left(\cos\theta_i - \sqrt{\epsilon_{r1} - \sin^2\theta_i}\right) / \left(\cos\theta_i + \sqrt{\epsilon_{r1} - \sin^2\theta_i}\right), & x = h \\ \left(\epsilon_{r1}\cos\theta_i - \sqrt{\epsilon_{r1} - \sin^2\theta_i}\right) / \left(\epsilon_{r1}\cos\theta_i + \sqrt{\epsilon_{r1} - \sin^2\theta_i}\right), & x = v \\ \left(R^v_{(1)} + R^h_{(1)}\right)/2, & x = rr \\ \left(R^v_{(1)} - R^h_{(1)}\right)/2, & x = rl \end{cases} \tag{2.19}$$

is the regular Fresnel reflection coefficient for the interface 1, θ_i is the angle of incidence, ϵ_{r1} is the permittivity of the middle medium. The term

$$R^x_{(2)} = \begin{cases} \left(\sqrt{\epsilon_{r1} - \sin^2\theta_i} - \sqrt{\epsilon_{r2} - \sin^2\theta_i}\right) / \left(\sqrt{\epsilon_{r1} - \sin^2\theta_i} + \sqrt{\epsilon_{r2} - \sin^2\theta_i}\right), & x = h \\ \left(\epsilon_{r1}\sqrt{\epsilon_{r1} - \sin^2\theta_i} - \epsilon_{r2}\sqrt{\epsilon_{r2} - \sin^2\theta_i}\right) / \left(\epsilon_{r1}\sqrt{\epsilon_{r1} - \sin^2\theta_i} + \epsilon_{r2}\sqrt{\epsilon_{r2} - \sin^2\theta_i}\right), & x = v \\ \left(R^v_{(2)} + R^h_{(2)}\right)/2, & x = rr \\ \left(R^v_{(2)} - R^h_{(2)}\right)/2, & x = rl \end{cases} \tag{2.20}$$

is the regular Fresnel reflection coefficient for the interface 2, and ϵ_{r2} is the permittivity of the bottom medium. The term

$$Q = \exp\left(2jkH\sqrt{\epsilon_{r1} - \sin^2\theta_i}\right) \tag{2.21}$$

accounts for a phase shift and magnitude attenuation due to the propagation within the middle layer, where H is the thickness of the middle layer. The dual-interface model can be extended to multi-interface model using an iterative algorithm, as described in Fuks and Voronovich (2000) and Zavorotny et al. (2003).

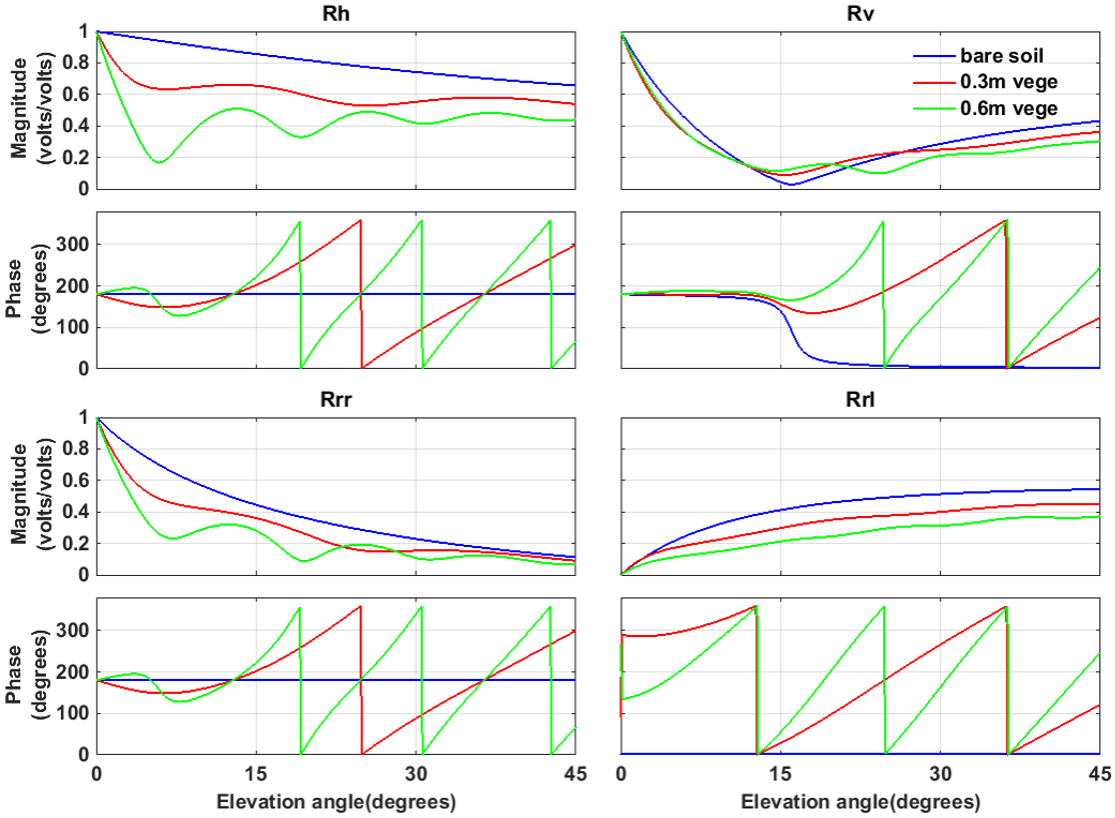

Figure 2.5: Composite Fresnel reflection coefficients for (a) horizontal, (b) vertical, (c) RHC to RHC, and (d) RHC to LHC polarizations. For each polarization, the reflection coefficients are calculated for three cases: soil, 30-cm vegetation on top of soil, and 60-cm vegetation on top of soil. For each figure, the top panel is the magnitude and the bottom panel is the phase of corresponding reflection coefficient.

In Figure 2.5, the composite Fresnel reflection coefficients with the dual-interface model are simulated for horizontal, vertical, RHC to RHC, and RHC to LHC polarizations. The permittivities of the middle and bottom layers are $1.05 + 0.013j$ and $12 + 1.05j$, which are typical values of heavy water vegetation (e.g. alfalfa) and agricultural soil (Elrayes and Ulaby, 1987; Burke et al., 2005; Chew et al., 2015). Compared to the single-interface model, the reflection coefficients with the dual-interface model show new characteristics.

For vegetation-covered soil, the magnitude of the horizontal reflection coefficient $|R_h|$ decreases as the vegetation grows. However, the decreasing trend of $|R_h|$ does not exhibit a monotonic change but has small variations. These variations are caused by the layering effect – the magnitude

of the horizontal reflection coefficient varies because the phase shift between the two reflections varies when the GPS satellite is rising or setting. The behaviours of $|R_{rr}|$ are also affected by vegetation growth, but the change of $|R_{rr}|$ is not as significant as $|R_h|$ – the curves of $|R_{rr}|$ for 0.3 m and 0.6 m vegetation almost coincide.

The vertical composite reflection coefficient is also different from the single-interface case. As illustrated before, under the single-interface model there is only one minimum, corresponding to the Brewster's angle, in the curve of $|R_v|$. As vegetation grows, there are more minima and their number/positions change with the vegetation canopy height. Again, these emerging minima are also the results of the layering effect.

The magnitude of the composite reflection coefficient for RHC to LHC polarization $|R_{rl}|$ shows a monotonic decreasing trend as the vegetation grows. However, $|R_{rl}|$ is smaller than $|R_h|$ for the same vegetation state. For example, $|R_{rl}|$ is about 0.5 when the elevation angle is around 20 degrees for the bare soil case while R_h is around 0.8 at the same elevation angle.

2.3 Applications of Various Polarizations

GPS-IR has been used and proven its feasibility in several remote sensing applications. The key idea is that the specific metric of GPS-IR (modulation frequency, amplitude, phase, or notches) is desired to be sensitive to the change of environmental parameters of interest. In this section, the relationship between environmental parameters and GPS-IR metrics is discussed. In the end, the requirements of several typical applications and corresponding suitable polarizations are summarized.

As mentioned in Chapter 1, the penetration depth of L-band signal is usually within 5 cm from the soil surface. This characteristic makes the single-interface model a good approximation to the actual soil conditions because the deep soil moisture, although could be very different from near-surface soil moisture, has little effect to the reflections of L-band signals. As demonstrated in Hallikainen et al. (1985) and Dobson et al. (1985), the soil permittivity is directly proportional to volumetric soil moisture (VSM), which further relates the GPS metric to VSM. From Figure

2.2, the magnitudes of horizontal and vertical reflection coefficients $|R_h|$ and $|R_v|$ show distinct behaviours corresponding to different soil permittivities (and also near-surface soil moisture). $|R_h|$ increases significantly as the soil moisture increases. The notch position in the curve of $|R_v|$ is also primarily determined by the soil moisture. As a result, the related metrics, modulation amplitude A and notch position, can be used for near-surface soil moisture retrievals. In Rodriguez-Alvarez et al. (2009), an instrument named the Soil Moisture Interference-pattern GNSS Observations at L-band (SMIGOL) is proposed for soil moisture retrieval. The key design of SMIGOL is utilizing a vertically-polarized (V-pol) patch antenna to exclusively receive the V-pol components from the direct and reflected signals. The horizontal polarization is also utilized for soil moisture retrieval in Alonso-Arroyo et al. (2014a), either as an independent measurement or an ancillary measurement.

RHCP is not suitable for soil moisture retrieval because $|R_{rr}|$ is almost not affected by soil permittivity. $|R_{rl}|$ is significantly affected by soil permittivity, and it has been used for soil moisture measurement in GNSS-R with a dual-antenna configuration (Masters et al., 2004; Katzberg et al., 2006). It is worth noting that the LHCP power is stronger at high elevation angles. However, GPS-IR usually focuses on low elevation angles for a large sensing footprint. Also a LHCP antenna would exclude the direct GPS signal. For these two reasons, LHCP is rarely used in GPS-IR.

The geometry-driven applications (e.g. snow depth and water level) mainly utilize the modulation frequency to infer the reflector height. The permittivity of water, either fresh water or sea water, is large enough to make water a dominant reflector. In most cases, snow permittivity is also large enough so that the effect of the underlying medium (soil) can be ignored. In Chapter 5, we will see that sometimes the existence of the underlying soil cannot be ignored for shallow snow. For now, we use the single-interface model to describe the characteristics of reflections off the snow surface. From Eq. (2.11), large reflection power, which is proportional to the magnitude of reflection coefficient, is required for a distinct interference pattern. Also the reflector height estimation error should be minimized, which requires a constant reflection coefficient phase ϕ_r. Obviously the horizontal polarization satisfies both requirements and hence is suitable for snow depth sensing.

As mentioned previously, the permittivity of the vegetation canopy is not large enough and the

Application	Snow depth, water level	Bare Soil Moisture	Vegetation Growth
Requirements	Large reflection power Constant reflection phase	Sensitive to change of ε_r	Large reflection power
Polarization	Horizontal	LHCP (amplitude) Horizontal (amplitude) Vertical (notch position)	Horizontal Vertical (notch positions)

Table 2.1: Requirements of GPS-IR applications and corresponding suitable polarizations

effect of the underlying soil has to be accounted for. From Figure 2.5, the magnitude of horizontal reflection coefficient R_h is significantly attenuated as vegetation grows. $|R_{rr}|$ also exhibits sensitivity to vegetation growth when vegetation height is low, but the sensitivity vanishes as vegetation grows higher. Vertical polarization has been used to retrieve vegetation height by utilizing the number and positions of the emerging notches (Rodriguez-Alvarez et al., 2011a,b). However, there is potential difficulty in detecting notches from the SNR considering the fact that the modulation amplitude A is small around the minima.

To summarize, we list the requirements of four typical remote sensing applications of GPS-IR and the suitable polarizations in Table 2.1. The horizontal polarization possesses several characteristics that make it suitable for all remote sensing applications discussed above. In the Chapter 3, we discuss the design and fabrication of two horizontally polarized antenna types. These two antenna types are used in the experiments presented in Chapters 4 to 7 of this dissertation.

Chapter 3

Antenna Design for GPS-IR

Antenna design is the key to improving the performance of GPS-IR as applied to remote sensing of the Earth's surface environmental parameters. In this chapter, several important antenna characteristics that are essential to understanding antenna design are first reviewed. Next, three linearly polarized antenna types are presented. Finally, two antenna prototypes, a half-wavelength dipole antenna and a patch antenna, are designed, optimized, and fabricated. These two antennas are used in the experiments presented in the following chapters.

3.1 Antenna Characteristics

An antenna, by definition, is a device that converts electric power into electromagnetic waves or converts received EM waves into electric power. An antenna is the essential component in almost all radio communication systems and applications. To better describe the performance of an antenna, some important characteristics are introduced here. The concepts and formulas are mostly from Balanis (2005).

(1) Spherical Coordinate

In antenna engineering, a spherical coordinate, rather than the Cartesian coordinate, is usually used to indicate the positions and directions (see Figure 3.1). ϕ is the azimuth angle within the range $0° \leqslant \phi < 360°$, and θ is the elevation angle within the range $0° \leqslant \theta < 180°$.

(2) Feed point

Feed point refers to the port at which the antenna is connected to a waveguide or transmission line to carry power to or from the antenna.

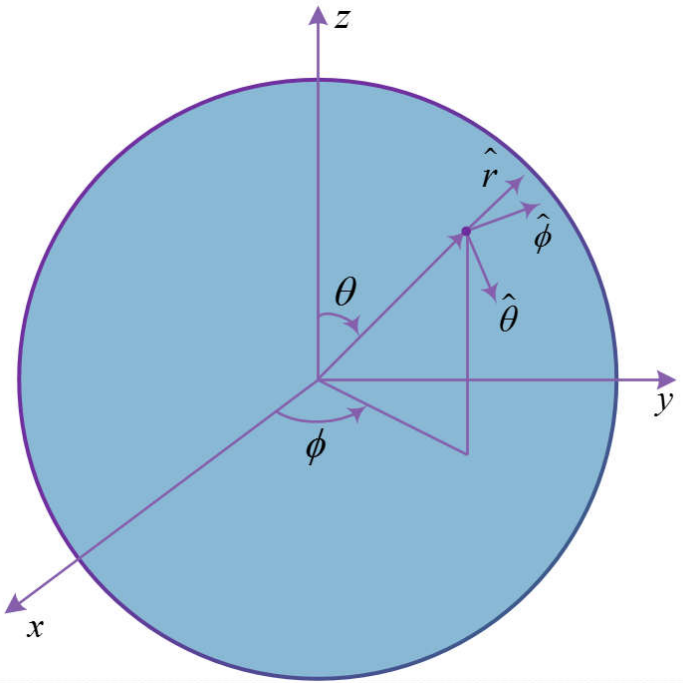

Figure 3.1: Spherical coordinate (r, θ, ϕ) for antenna engineering. The Cartesian coordinates x, y, z can be converted from the spherical coordinates by $x = r\sin\theta\cos\phi$, $y = r\sin\theta\sin\phi$, $z = r\cos\theta$.

(3) Radiation density $S(r,\theta,\phi)$ and radiation intensity $U(\theta,\phi)$

In reality, no antenna radiates radio wave power uniformly in all directions. In antenna engineering, radiation density $S(r,\theta,\phi)$ and radiation intensity $U(\theta,\phi)$ are used to describe the power distribution for a transmitting antenna. For time-harmonic EM waves, radiation density $S(r,\theta,\phi)$ is defined as the time average of the instantaneous Poynting vector in the radial direction, i.e.

$$S(r,\theta,\phi) = Re(\vec{E}\times\vec{H}^*)\cdot\hat{r} \quad W/m^2 \tag{3.1}$$

where $\vec{E}$ and $\vec{H}$ are the electric field and magnetic field, respectively, $\hat{r}$ is the unit vector

in the radial direction. With $S(r, \theta, \phi)$, the total radiated power P_{rad} is computed by

$$P_{rad} = \oint_S S(r, \theta, \phi) \mathrm{d}s \tag{3.2}$$

Usually the radiation intensity $U(\theta, \phi)$, which is only relevant to the direction parameters (θ and ϕ), is used to better describe the directional distribution of the radiated power. $U(\theta, \phi)$ is defined as the power radiated per solid angle Ω, i.e.

$$U(\theta, \phi) = \frac{dP_{tr}}{d\Omega} = S(r, \theta, \phi) r^2 \tag{3.3}$$

where the relationship $d\Omega = ds/r^2$ is used. The total radiated power P_{rad} is also computed by

$$P_{rad} = \int_0^{2\pi} \mathrm{d}\phi \int_0^{\pi} \sin\theta U(\theta, \phi) \mathrm{d}\theta \tag{3.4}$$

(4) Efficiency e

An antenna only converts a portion of the total input power to radio waves, and the ratio of radiated power to input power is defined as the antenna's efficiency e:

$$e = \frac{P_{rad}}{P_{total}} \tag{3.5}$$

The efficiency loss arises from two aspects: (1) as a one-port network component, the antenna reflects back a portion of the incident power because of impedance mismatch; (2) part of the power delivered to the antenna is dissipated as heat. Therefore, the overall efficiency is a product of two factors:

$$e = (1 - |\Gamma|^2)\ e_{rad} \tag{3.6}$$

where Γ is the reflection coefficient because of impedance mismatch, e_{rad} is the radiation efficiency, which is defined as the ratio of the radiated power to the delivered power.

(5) Directivity $D(\theta, \phi)$ and Gain $G(\theta, \phi)$

The radiation density and intensity of an isotropic antenna, which is an idealized antenna

that radiates power equally in all directions, are computed by

$$S_{iso} = \frac{P_{rad}}{4\pi r^2}, \quad U_{iso} = \frac{P_{rad}}{4\pi} \tag{3.7}$$

For a non-isotropic antenna, the directivity $D(\theta, \phi)$ is defined as

$$D(\theta, \phi) = \frac{S(r, \theta, \phi)}{S_{iso}} = \frac{U(\theta, \phi)}{U_{iso}} \tag{3.8}$$

The definition of Gain $G(\theta, \phi)$ is similar to directivity, but multiplied by its efficiency:

$$G(\theta, \phi) = e\ D(\theta, \phi) \tag{3.9}$$

From the definitions, the losses are taken into account in the gain, but not in the directivity. It is worth noting that the maximum directivity, D_0, can be of primary interest and is referred to as directivity for simplicity.

(6) Radiation pattern

The radiation pattern is a graphical description of the power emission by a transmitting antenna. Usually the radiation power in dB scale versus spatial angle is used. By definition, the radiation pattern is a three-dimensional power plot in all directions. However, a two-dimensional plot for a particular cut on elevation or azimuth is more popular in practical applications. Some features of a typical radiation pattern are shown in Figure 3.2. At some particular directions, radiation reaches to local maximum, referred to as a lobe, or decreases to zero, referred to as a null. The main lobe refers to the lobe that has the maximum power level. Other lobes are usually much smaller than the main lobe, and are referred to as side lobes. In the direction opposite to the main lobe, many antennas have a back lobe smaller than the main lobe but considerably larger than the side lobes.

(7) Polarization

The polarization of an antenna refers to the oscillation direction of the radiated electric field vector. Usually an antenna is either linearly (vertical or horizontal) or circularly (left-handed or right-handed) polarized. A radio wave is linearly polarized if the electric field

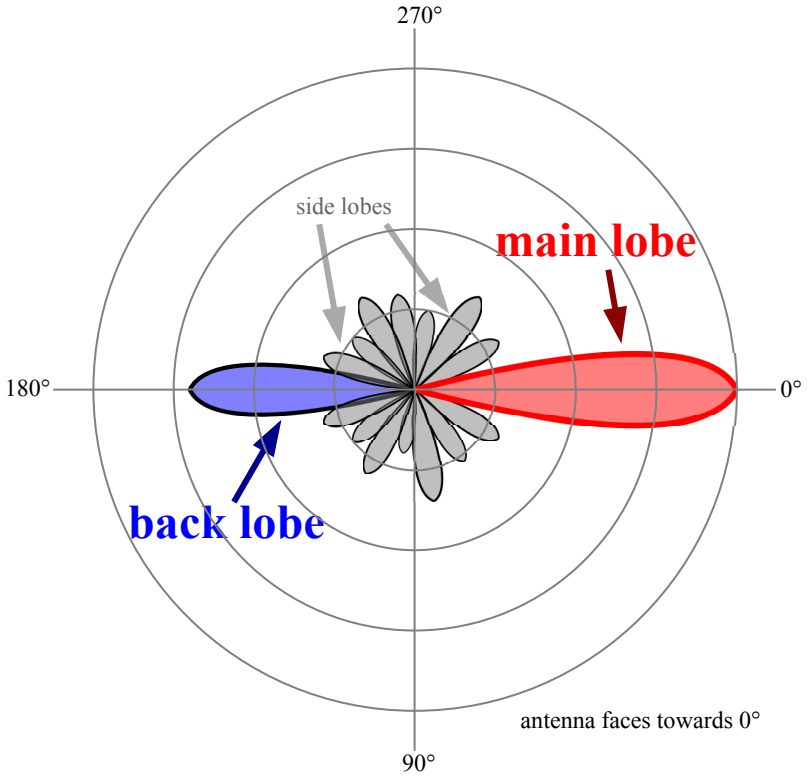

Figure 3.2: Typical features of a radiation pattern. The maximum lobe in the desired direction is the main lobe. The smaller lobes are side lobes. Many antennas have a back lobe that is smaller than the main lobe but larger than the side lobe. Figure courtesy of Wikipedia.

vector observed at a fixed location is always oriented along the same straight line at every instant of time. A radio wave is circularly polarized if the electric field vector observed at a fixed location traces a circle as a function of time. Seen into the propagation direction, it is right-handed circularly polarized if the electric field vector is rotating clockwise, or left-handed circularly polarized if the electric field is rotating counter-clockwise. Linearly polarized antennas are usually used in earth to earth communications (e.g. AM and FM radios); circularly polarized antennas are often used for satellite communication (e.g. GNSS).

(8) Beamwidth

There are a number of beamwidth definitions in antenna engineering. The most frequently

used is the half-power beamwidth (HPBW) or 3-dB beamwidth, defined as "in a plane containing the direction of the maximum of a beam, the angle between the two directions in which the radiation intensity is one-half value of the beam" (Balanis, 2005). Another important beamwidth is the angular separation between the first nulls of the pattern, referred to as the first-null beamwidth (FNBW). Even with the same definition, two different beamwidth values may be obtained depending the cut slice is in E-plane or H-plane. An approximate relationship between directivity and HPBW is given by :

$$D_0 \approx \frac{32000}{\theta_E \, \theta_H} \tag{3.10}$$

where θ_E and θ_H are the 3-dB beamwidths in the E- and H-planes in degrees, respectively.

(9) Effective length $\vec{l}_{eff}$ and effective area A

Effective length can be defined with either the transmitting antenna or the receiving antenna. For a transmitting antenna, we denote the electric field at position (r, θ, ϕ) by $\vec{E}(r, \theta, \phi)$. If we want to replace the antenna with an electric current element, a short wire of length $l \ll \lambda$ carrying a uniform current I_A at the feed point, such that the electric field radiated by the electric current element is the same as the original one, then a vector $\vec{l}_{eff} = l\hat{e}$ is obtained where $\hat{e}$ is the unit vector in the direction of electric field. The vector $\vec{l}_{eff}$ is referred to as the vector effective length. For a receiving antenna, the effective length is defined such that the open circuit voltage V_{oc} can be formulated by

$$V_{oc} = \vec{l}_{eff} \cdot \vec{E}_{inc} \tag{3.11}$$

where $\vec{E}_{inc}$ is the incident electric field at the feed point of the antenna. These two definitions are proved to be equivalent using the reciprocity theorem.

The effective area $A(\theta, \phi)$ is the defined as the ratio of received power to the incident power density, i.e.

$$A(\theta, \phi) = \frac{P_r}{S(\theta, \phi)} \tag{3.12}$$

The maximum effective area A_m and the maximum directivity D_0 for any antenna are related by

$$A_m = \frac{\lambda^2}{4\pi} D_0 \tag{3.13}$$

3.2 Antenna Types

As mentioned in Section 2.3, linearly polarized antenna is suitable for most environmental applications of GPS-IR. However, most commercial off-the-shelf (COTS) GPS/GNSS antennas are designed to be RHCP for precise positioning and timing purposes, and there are no readily available linearly polarized GPS/GNSS antennas. In this section, we introduce three linearly polarized antenna types that can be potentially used for GPS-IR remote sensing applications.

(1) Half-wavelength Dipole Antenna

A half-wavelength dipole antenna is just composed of two wires (see Figure 3.3) and is one of the most commonly used wire antennas. The length of the wires is equal to a half wavelength of the resonant frequency. Some characteristics of the half-wavelength dipole antenna are listed here.

- radiation density and intensity

  The radiation density and intensity of a half-wavelength dipole antenna is formulated as:

$$S(r, \theta, \phi) = \eta \frac{|I_0|^2}{8\pi^2 r^2} \sin^3 \theta \tag{3.14}$$

$$U(\theta, \phi) = \eta \frac{|I_0|^2}{8\pi^2} \sin^3 \theta \tag{3.15}$$

  where I_0 is the wire current, $\eta = 377\ \Omega$ is the intrinsic impedance of the air. Because $U(\theta, \phi)$ is only relevant to θ, so the half-wavelength dipole antenna is an omnidirectional antenna.

- vector effective length and polarization

The vector effective length of the half-wavelength dipole antenna is

$$\vec{l}_{eff} = -\hat{a}_\theta \frac{\lambda}{\pi} \frac{\cos\left(\frac{\pi}{2}\cos\theta\right)}{\sin\theta} \tag{3.16}$$

The direction of $\vec{l}_{eff}$ is aligned with the unit vector in θ direction $\hat{a}_\theta$, so by definition, the dipole antenna is vertically polarized.

- directivity and effective area

  The maximum directivity of the half-wavelength dipole antenna is

$$D_0 = 4\pi \frac{U_{max}}{P_{rad}} \approx 1.643 \tag{3.17}$$

We can see that the half-wavelength dipole antenna is not highly directive, which is beneficial for GPS-IR remote sensing because the GPS satellites are distributed in almost all azimuths. The corresponding maximum effective area is

$$A_m = \frac{\lambda^2}{4\pi} D_0 \approx 0.13\lambda^2 \tag{3.18}$$

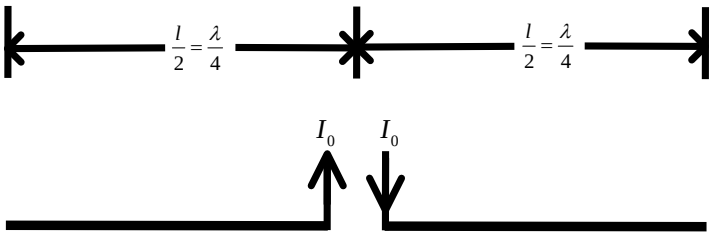

Figure 3.3: Structure of the half-wavelength dipole antenna. The length of wire is equal to a half wavelength of the resonant frequency.

(2) Loop Antenna

The loop antenna is another simple, inexpensive, and widely used wire antenna. A loop antenna may take different forms, such as rectangular, square, circle, ellipse, etc. The

circular loop antenna is the most commonly used loop antenna, so only the characteristics of the circular loop antenna are introduced here.

Loop antennas are usually classified into two categories: electrically small and electrically large. Electrically small means that the circumference or perimeter of the loop antenna is much smaller than the wavelength of the resonant frequency. Electrically large means that the antenna's circumference or perimeter is comparable to the wavelength of the resonant frequency. Electrically small loop antennas are mainly used for low-frequency bands, and usually electrically large loop antennas are used for L-band frequencies. The following characteristics are referring to electrically larger loop antenna unless otherwise specified.

- radiation density and intensity

  The radiation density and intensity of loop antenna is

$$S(r,\theta,\phi) = \frac{(a\omega\mu)^2|I_0|^2}{8\eta r^2} J_1^2(ka\sin\theta) \tag{3.19}$$

$$U(\theta,\phi) = \frac{(a\omega\mu)^2|I_0|^2}{8\eta} J_1^2(ka\sin\theta) \tag{3.20}$$

  where a is the radius of loop, $\omega = 2\pi f$ is the angular frequency, μ is the permeability, I_0 is the wire current, η is the intrinsic impedance of air, $J_1(z)$ is the Bessel function of the first kind of order one.

- vector effective length and polarization

  The vector effective length of loop antenna is

$$\vec{l}_{eff} = -\hat{a}_\phi j k_0 \pi a^2 \cos\phi \sin\theta \tag{3.21}$$

  The direction of $\vec{l}_{eff}$ is aligned with the unit vector in ϕ direction $\hat{a}_\phi$, so by definition, the dipole antenna is horizontally polarized.

- directivity and effective area

  The maximum directivity of loop antenna is

$$D_0 = 0.667\frac{C}{\lambda} \tag{3.22}$$

where $C = 2\pi a$ is the circumference. The corresponding maximum effective area is

$$A_m = \frac{\lambda^2}{4\pi}\left(0.667\left(\frac{C}{\lambda}\right)\right) \tag{3.23}$$

(3) Patch Antenna

A patch (microstrip) antenna is the most commonly used GPS/GNSS antenna type for low-cost GPS/GNSS solutions. It is widely used in satellite communication, GPS/GNSS, mobile communication, and military purposes for the advantages of compact size, flexibility in polarization configuration, ease of manufacturing using the printed-circuited technology. As shown in Figure 3.8(a), the patch antenna has a "sandwich" structure: top and bottom metallic surfaces with a substrate layer in the middle. The top patch has various shapes: square, rectangular, circular, ellipses, triangular, etc. The bottom metallic surface serves as the ground plane. The permittivity of the middle substrate affects the antenna's size and bandwidth. A large permittivity can reduce the antenna size but narrows the antenna's bandwidth. In this section, we only introduce the rectangular patch antenna's characteristics because it is flexible in terms of polarization configuration.

- radiation density and intensity

  The electric field radiated by a patch antenna is ($k_0 h \ll 1$):

$$E_\phi \approx j\frac{2V_0 \exp(-jk_0 r)}{\pi r}\left(\sin\theta\frac{\sin\left(\frac{k_0 W}{2}\cos\theta\right)}{\cos\theta}\right)\cos\left(\frac{k_0 L_e}{2}\sin\theta\sin\phi\right) \tag{3.24}$$

$$E_\theta \approx 0 \tag{3.25}$$

$$E_r \approx 0 \tag{3.26}$$

  where $V_0 = hE_0$, E_0 is the electric field at the patch margin, k_0 is the free space wave length, L_e is the effective length of the patch. With radiated electric field, the radiation density and intensity can be computed using Eq. (3.1) and (3.3).

- vector effective length and polarization

  The polarization of a patch antenna can be configured to be horizontal, vertical,

RHCP, or LHCP by adjusting the position of the feed point. The magnitude of the effective length is approximated by ($W \gg h$):

$$L_{eff} = L + 0.824h\frac{(\epsilon_{eff} + 0.3)\left(\frac{W}{h} + 0.264\right)}{(\epsilon_{eff-0.258})\left(\frac{W}{h} + 0.8\right)} \tag{3.27}$$

where

$$\epsilon_{eff} = \frac{\epsilon_r + 1}{2} + \frac{\epsilon_r - 1}{2}\left(1 + 12\frac{h}{W}\right)^{(-1/2)} \tag{3.28}$$

is the effective dielectric constant and ϵ_r is the permittivity of the substrate.

- directivity and effective area

  The maximum directivity D_0 of a patch antenna is:

$$D_0 = \begin{cases} 6.6 \approx 8.2\ dB; & W \ll \lambda_0 \\ 8\left(\frac{W}{\lambda_0}\right); & W \gg \lambda_0 \end{cases} \tag{3.29}$$

  The maximum effective area can be computed using Eq. (3.13).

3.3 Antenna Design and Fabrication

In Section 3.2, three antenna types that can be potentially used for the GPS-IR remote sensing are presented. Among the three types, the loop antenna has some intrinsic disadvantages that make it inappropriate for self-fabrication: the loop antenna usually has a low efficiency and thus a considerable portion of energy is dissipated as heat; the loop inductance, both internal and external, increases the difficulty of impedance matching. Therefore, in this section, the design and fabrication procedures of the other two antenna types, dipole antenna and patch antenna, are presented.

3.3.1 Dipole Antenna

As shown in Figure 3.3, the half-wavelength antenna consists of two wires and the length of each wire is approximately a quarter wavelength of the working frequency. In addition, a matching circuit needs to be included to reduce to the energy loss because of reflection. To simplify the

fabrication process, we use the structure proposed in Norberg (2011) to build a half-wavelength dipole antenna (see Figure 3.4(a)). Strictly speaking, it is not a dipole antenna but a "discone antenna with a wire mesh skirt". However, the polarization and gain pattern are very close to a half-wavelength dipole antenna. It is also referred to as a monopole antenna in some literature. In this dissertation, we name it the half-wavelength dipole antenna for simplicity unless otherwise specified. This design is made up of a hardline coaxial cable, stripped out of its outside copper layer to expose the inner pin. The length of the inner pin is around a quarter wavelength. On the outside copper layer, there are four copper wires soldered on it having two functions: (1) the vertical components of the currents on the four wires are combined together and serve as the other quarter wavelength wire of the half wavelength dipole antenna; (2) the bending angles of the four wires determine the inductance of the input impedance, and thus can be used for impedance matching. It is worth noting that the the length of the top pin is smaller than a quarter wavelength due to the dielectric substrate between the outside copper layer and inner pin. Therefore, both a precise model and actual measurement are required to assist the design and fabrication of the half-wavelength dipole antenna.

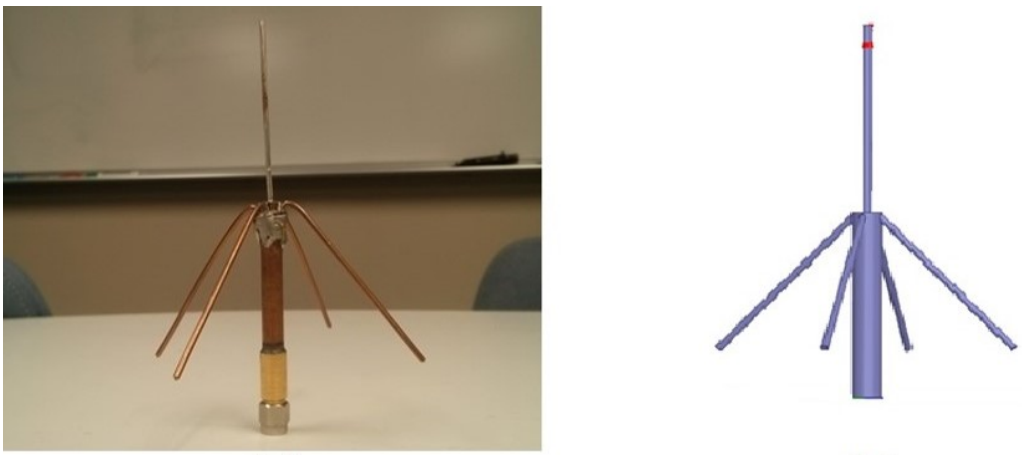

Figure 3.4: Fabricated half-wavelength dipole antenna and its HFSS model.

We use the simulation software of HFSS by Ansys Corp. to build the antenna model and simulate its characteristics. HFSS also provides a powerful optimization tool that allows user to

scan several key design parameters (e.g. pin length, bending angle) to find the optimal values. The design procedures are as follows:

(1) Create model in HFSS

The created HFSS model is shown in Figure 3.4(b). HFSS provides a variety of material models that provide the best approximation to real antennas. For example, the FR4 epoxy material in HFSS has the same dielectric properties with the substrate of the coaxial hardline. The radius of the inner pin and the thickness of copper layer in the model are also configured to be the the same values as the actual coaxial hardline.

(2) Optimize model parameters

The bending angles of the four wires primarily determine the impedance and are used for impedance matching. Here the magnitude of reflection coefficient $|S_{11}|$ are simulated corresponding to a series of bending angle values from 115 to 145 degrees, as shown in Figure 3.5.

With the optimized bending angle, we then adjust the pin length to make the null in $|S_{11}|$ located in L1 or L2 frequency. Again, a number of pin length values are simulated to find the optimal pin length, as shown in Figure 3.6. From the simulation results, pin length of 41.0 mm is the optimal value.

With the optimized parameters, the simulated radiation pattern of the dipole antenna is shown in Figure 3.7. The gain in the ϕ direction, corresponding to the gain of the horizontal polarization, is negligible compared to the gain in the θ direction corresponding to the gain of the vertical polarization. However, if the antenna is tipped, it is horizontally polarized around the direction of $\theta = 90^\circ$ (in the orthogonal direction). In the orthogonal direction, the gain is constant which does not change with the elevation angle. The half-wavelength dipole antenna provides the flexibility of working with either horizontal-polarization or vertical-polarization, which is very helpful to evaluate the performance of two polarizations using a single antenna type.

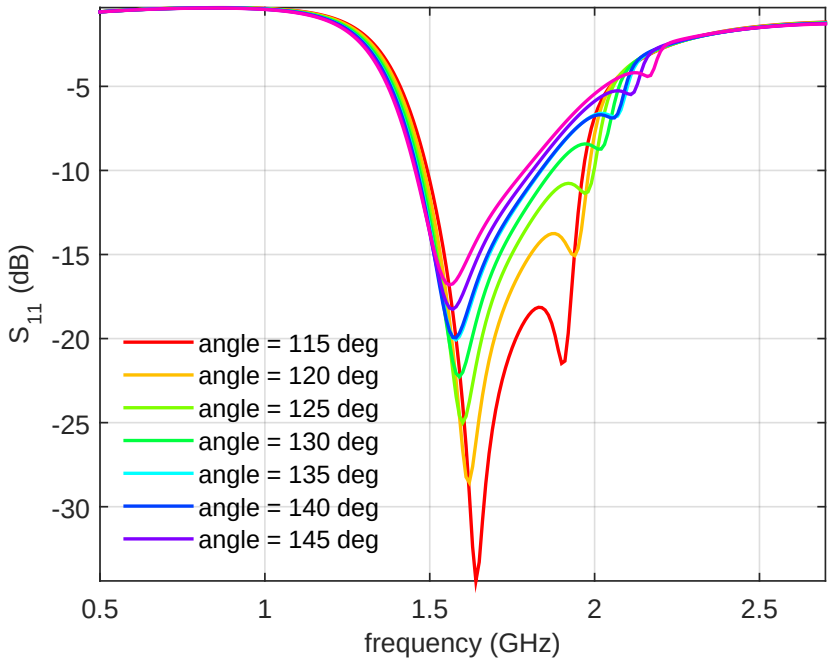

Figure 3.5: A number of bending angle parameters are scanned. The optimal bending angle is 115°.

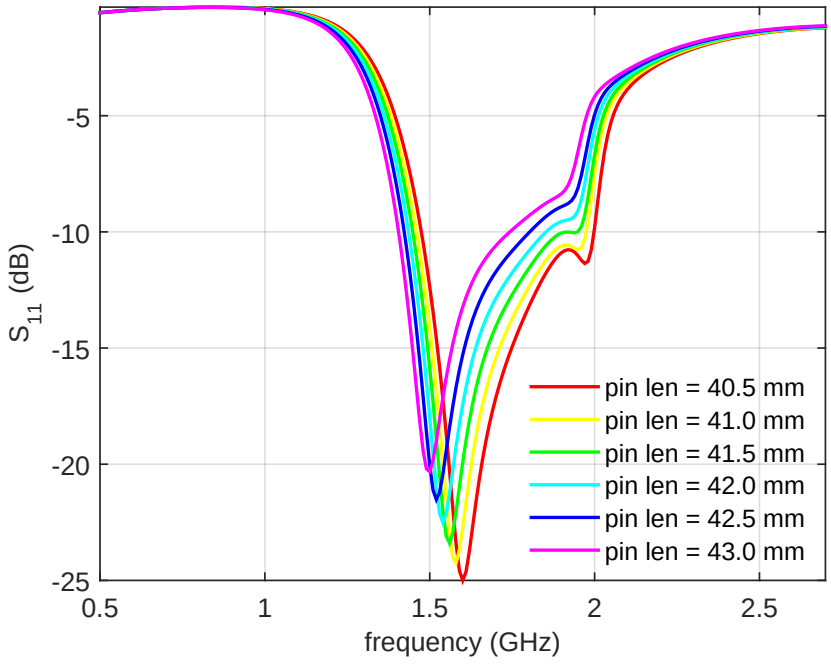

Figure 3.6: A number of pin length parameters are scanned. The optimal pin length is 40.5 mm.

(3) Final tuning

The preliminarily built half-wavelength dipole antenna using the optimized parameters needs final tuning to assure that the measured characteristics are the best possible achieved. A network analyzer is utilized to measure and adjust the reflection coefficient of the half-wavelength dipole antenna. The bending angle and pin length are further tuned to get the best possible performance.

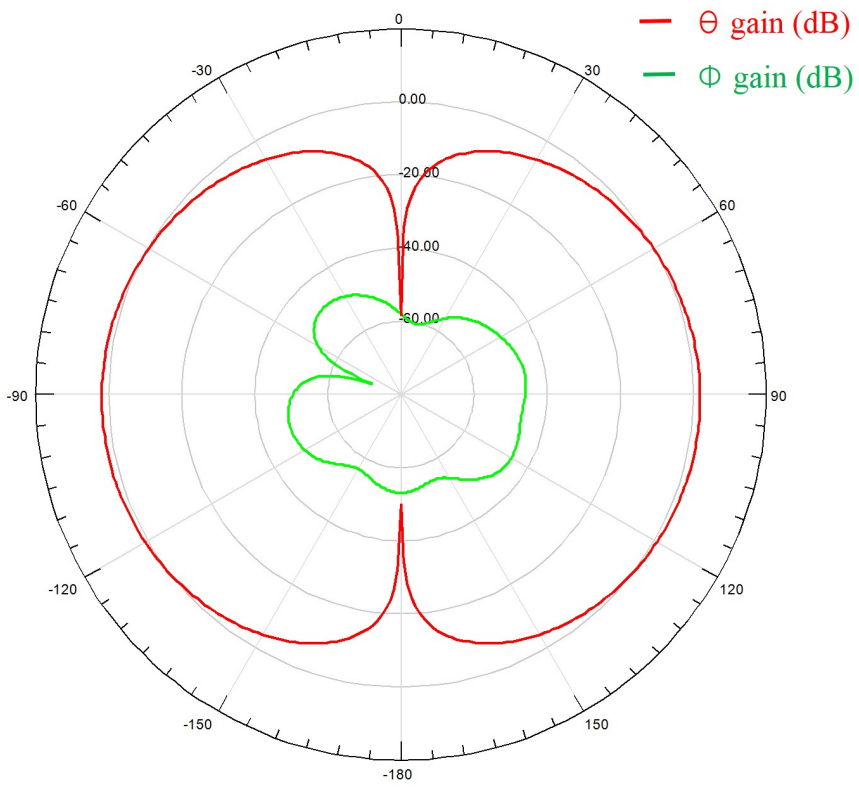

Figure 3.7: Radiation pattern of the proposed dipole antenna. The θ gain is several orders of magnitude greater than ϕ gain, so by definition, the half-wavelength dipole antenna is vertically polarized.

3.3.2 Patch Antenna

There are primarily three models to describe the patch antenna: transmission-line model, cavity model, and full-wave model. The transmission-line model gives good physical insight and

is easy to understand. It also provides a clear design procedures given antenna specifications. However, it is difficult to model the coupling of the radiation slots using the transmission line model and thus less accurate than the other two models. In this section, the procedure of patch antenna design using transmission-line model is presented first. Then the design parameters are further refined using HFSS simulation.

The procedures of designing a patch antenna given the resonant frequency f_r, the substrate height h, and the permittivity ϵ_r are as follows:

1. Compute the patch width W by

$$W = \frac{c}{2f_r}\sqrt{\frac{2}{\epsilon_r + 1}} \tag{3.30}$$

where c is the velocity of light in free space.

2. Determine the effective permittivity of the patch antenna using

$$\epsilon_{r,eff} = \frac{\epsilon_r + 1}{2} + \frac{\epsilon_r - 1}{2}\left(1 + 12\frac{h}{W}\right)^{-1/2} \tag{3.31}$$

3. Determine the extension of length ΔL using

$$\Delta L = 0.412h\frac{(\epsilon_{r,eff} + 0.3)\left(\frac{W}{h} + 0.264\right)}{(\epsilon_{r,eff} - 0.258)\left(\frac{W}{h} + 0.8\right)} \tag{3.32}$$

4. Determine the actual length of the patch using

$$L = \frac{1}{2f_r\sqrt{\epsilon_{r,eff}}\sqrt{\mu_0\epsilon_0}} - 2\Delta L \tag{3.33}$$

where $\mu_0 = 4\pi \times 10^{-7} N/A^2$ is the vacuum permeability, and $\epsilon_0 = 8.854 \times 10^{-12} F/m$ is the vacuum permittivity.

5. Determine the recess distance y_0 for impedance matching, i.e. solve for y_0 using

$$\frac{1}{2(G_1 + G_{12})}\cos^2\left(\frac{\pi}{L}y_0\right) = 50 \tag{3.34}$$

where

$$G_1 = \frac{W}{120\lambda_0}\left(1 - \frac{1}{24}(k_0 h)^2\right) \tag{3.35}$$

and

$$G_{12} = \frac{1}{120\pi^2} \int_0^{\pi} \left(\frac{\sin\left(\frac{k_0 W}{2} \cos\theta\right)}{\cos\theta} \right)^2 J_0(k_0 L \sin\theta) \sin^3\theta \, d\theta \tag{3.36}$$

where $J_0(z)$ is the Bessel function of the first kind of order zero.

With the preliminary dimension values of the patch antenna, we can build the HFSS model and scan the parameters to get the optimal values. The HFSS model of the patch antenna is shown in Figure 3.8(b).

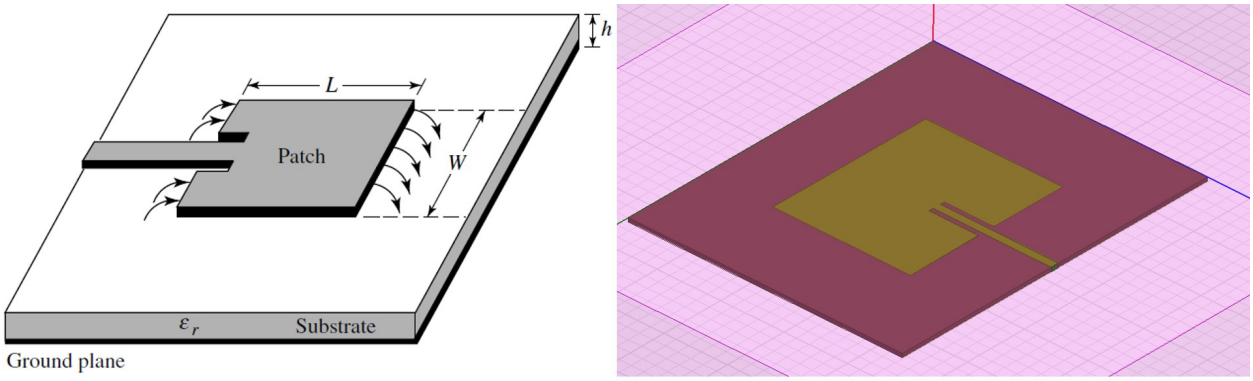

Figure 3.8: (a) Structure of a patch antenna. (b) HFSS patch antenna model. The model utilizes a transmission line feed, and a recessed insert feed to match the impedance.

Using a similar optimization procedures as the half-wavelength dipole antenna, the final parameters of the horizontally polarized L1 patch antenna are:

$$L = 54.02 \; mm \tag{3.37}$$

$$W = 67.33 \; mm \tag{3.38}$$

$$h = 1.52 \; mm \tag{3.39}$$

$$y_0 = 19.543 \; mm \tag{3.40}$$

The magnitude of reflection coefficient is given in Figure 3.9 . The radiation patterns in the E-plane ($\theta = 90°, 0° \leqslant \phi < 180°$) and in the H-plane ($\phi = 0°, 0° \leqslant \theta < 180°$) are given in Figure 3.10 and Figure 3.11, respectively.

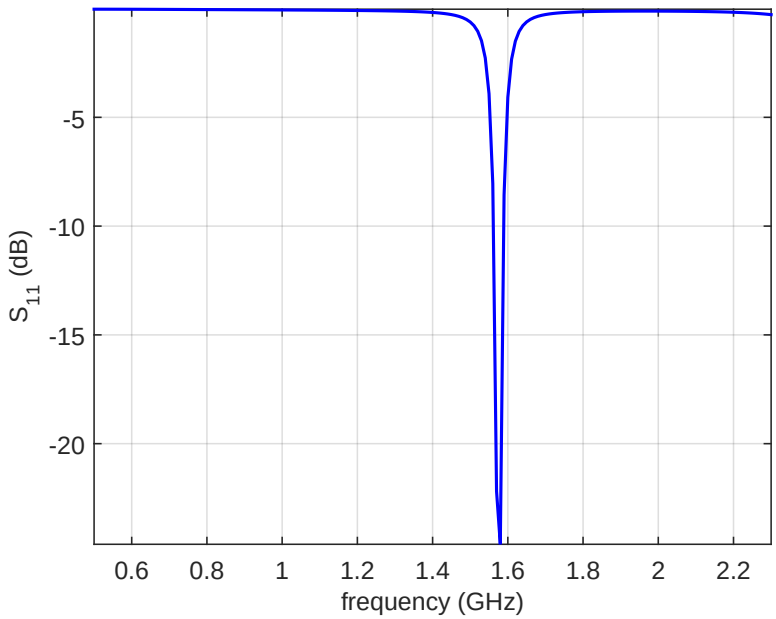

Figure 3.9: Reflection coefficient magnitude S_{11} of the patch antenna. The resonant frequency is L1 (1575.42 MHz).

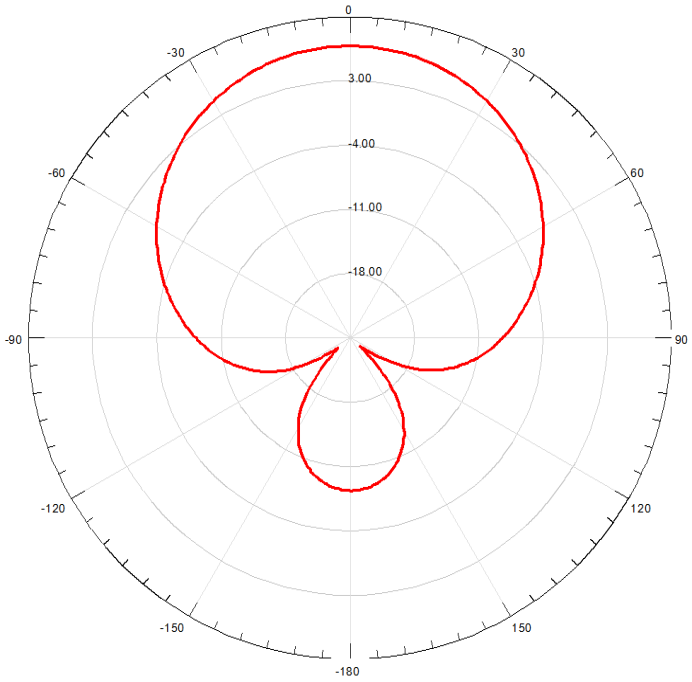

Figure 3.10: E-plane radiation pattern of the patch antenna. E-plane is the slice cut defined by $\theta = 90°, 0° \leqslant \phi < 180°$.

The designed patch antenna is fabricated by the First RF Corp. located in Boulder, Colorado, USA. The horizontally polarized patch antenna is more directive than the half-wavelength dipole antenna (in a horizontal-polarization configuration): it has a main lobe and a smaller side lobe. This directive difference indicates that the half-wavelength dipole antenna is more suitable for the open area while the patch antenna is preferred when there is an undesired multipath/reflection source (e.g. nearby structure). The dipole antenna is used in the snow experiments carried out in Table Mountain and Marshall Field (Chapters 4 and 5) and the vegetation experiment (Chapter 7). The patch antenna is used for the mountain-top snow experiment conducted at the Storm Peak Laboratory (Chapter 6). The comparison of the two antenna types is also presented in Chapter 6.

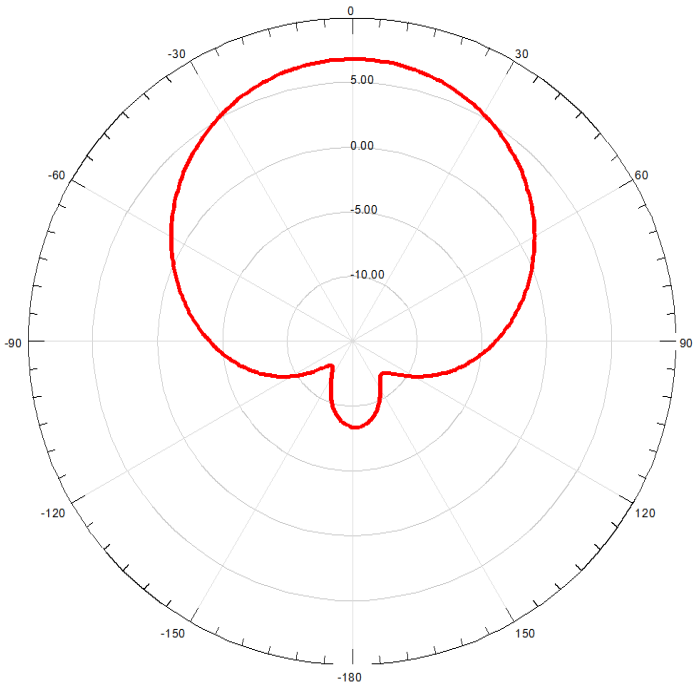

Figure 3.11: H-plane radiation pattern of the patch antenna. H-plane is the slice cut defined by $\phi = 0°, 0° \leqslant \theta < 180°$.

Chapter 4

Snow Experiment 1: Table Mountain Experiment

The snowpack is an important component in the investigation of global climate and hydrology as well as its functionality for fresh water reservoirs (Shi and Dozier, 2000a,b). The measurement of the amount of water stored in the snowpack and its melt rate are essential for the management of the water supply and flood control systems. The snowpack provides fresh water for more than one-sixth of the world's population and contribute significantly to the cause of floods (Li and Simonovic, 2002; Barnett et al., 2005; Armstrong and Brun, 2008). The measurement of snow depth and SWE is an important application of GPS-IR. The GPS-IR technique provides a relatively large footprint ($\sim$1000 m^2) and high temporal sampling rate (GPS satellite repeatability is $\sim$1 day), and thus can be used as an independent snow data measurement to complement the traditional regional snow data sets (Boniface et al., 2015). In addition, the GPS-IR snow measurements can also be used for validation of the measurements from air- or space-borne remote sensing instruments.

As demonstrated in Chapter 2, the horizontal polarization is suitable for snow depth sensing because of the large reflection coefficient magnitude and relatively constant phase. In Chapter 3, a dipole antenna that works with either vertical polarization or horizontal polarization is designed and built. An experiment campaign was conducted on the Table Mountain plateau, Boulder, Colorado, USA during February 2012. The purpose of the experiment was to verify the feasibility and superiority of the proposed dipole antenna in geometry-driven or altimetric applications, more specifically, in snow depth sensing. In this chapter, the experimental setup and data are presented. The SNR data from the dipole antenna show the potential of obtaining a more precise estimation

of the reflector height and thus the snow depth.

4.1 Experimental Setup

It is demonstrated that the L2C signal, a new civilian signal on GPS L2 frequency (1227.6 MHz), achieves more accurate snow depth retrievals for geodetic GPS data (Larson and Nievinski, 2013). The new L2C signal is only available on the modernized GPS satellites, i.e. the Block IIR-M, Block IIF and future Block III. In this experiment, the L2C signal instead of the legacy L1 C/A signal, is used for snow depth sensing. A MATLAB-based Software Define Receiver (SDR), which can provide the maximum flexibility, is developed for data processing.

4.1.1 L2C Signal

Since 2005, a new civil signal on GPS L2 frequency designated as L2C has been available for civilian users. The L2C code is composed of two kinds of PRN codes: the CM (Civil Moderate) code and the CL (Civil Long) code. The CM and CL codes are combined together in a time-multiplexing method, as shown in Figure 4.1. The CM code consists of 10,230 chips and the chip rate is 511.5 Kcps, resulting in a code period of 20 ms. The CL code is much longer with a code length of 767,250 chips. The chip rate of the CL code is also 511.5 Kcps and the code period is 1.5 s. The combined code is referred to as CS code, which has a equivalent chip rate of 1.023 Mcps. The civil navigation (CNAV) messages is only modulated on the CM code and the raw bit rate is 25 bps. However, the CNAV bits are encoded with rate-1/2 Forward Error Correction (FEC) resulting in a symbol rate of 50 sps. The data-free CL code offers the option of extending integration time to achieve better performance in weak SNR environments. Overall, the L2C code has the following advantages for remote sensing compared to the L1 C/A code:

(1) L2C has better code cross correlation (40 dB compared to L1 C/A's 24 dB) and continuous wave interference rejection.

(2) L2C has a pilot (data-free) channel for extended integration time. This is helpful to signal

tracking when the SNR is at deep nulls for GPS-IR applications.

(3) Improved navigation data structure offers a 5 dB improvement compared to L1 C/A.

At the time of experiment, L2C signal was only available on 9 GPS satellites, i.e. PRN 1, 5, 7, 12, 15, 17, 25, 29, 31. Therefore, the available ground tracks of the L2C signal were less than L1 C/A signal. As a result, the orientation of the GPS antenna needs to be carefully considered to make sure the target ground track is in the optimal sensing area.

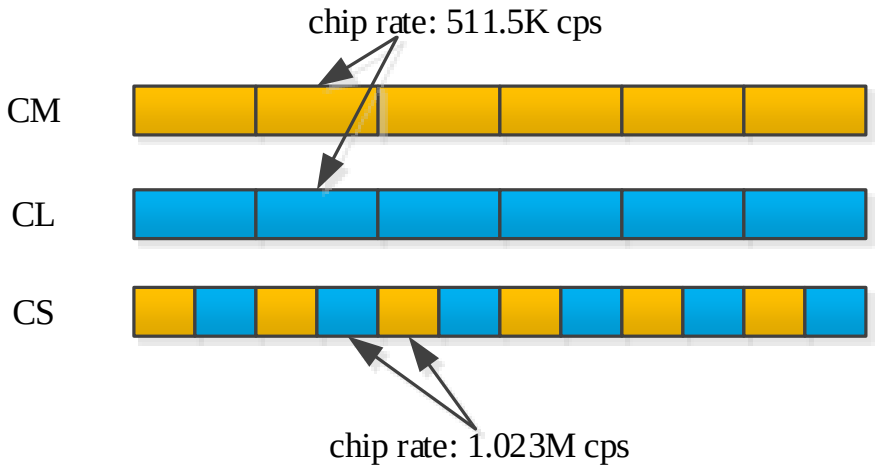

Figure 4.1: Both CM and CL have a chip rate of 511.5 Kcps. CM and CL codes are time-multiplexed combined to CS code: for each CS chip, the first half is CM chip and the second half is CL chip. The chip rate of CS code is 1.023 Mcps. The CNAV bits/symbols are only modulated on the CM code and CL serves as a pilot channel for extending integration time.

4.1.2 Front-end: Universal Software Radio Peripheral

The front-end down-converts the antenna received radio frequency (RF) samples to a much lower intermediate frequency (IF) and saves the IF samples to a hard drive for post-processing. In this experiment, a universal software radio peripheral (USRP) N210 platform (see Figure 4.2) from the Ettus Research Inc. is used as the front-end. The USRP has the following characteristics that make it a powerful RF/IF data collection tool.

(1) It has wide frequency range from 0.8 to 2.35 GHz, covering all GPS civil frequencies.

(2) It provides a sampling rate up to 50 Mbps and a RF bandwidth up to 25 MHz.

(3) It provides a 14-bit ADC/DAC that enables high dynamic range and low quantization noise level.

(4) The USRP has 1-GB Ethernet interface that provides enough bandwidth to transfer data.

In this experiment, the center frequency was set to be 1227.5 MHz (IF = 100 KHz) and the sampling rate was 2 Mbps. The sampling rate only covers the energy in the main lobe of the spectrum, which is primarily to reduce the storage and post-processing load.

Figure 4.2: The USRP N210 from Ettus Inc. is used as the front-end to convert RF down to IF and save the IF samples to a hard drive.

4.1.3 L2C Software Defined Receiver

A SDR was developed to process the raw IF data collected by the USRP. It was an extension of the open source L1 MATLAB receiver documented in Borre et al. (2007). In a typical SDR, the Delay Lock Loop (DLL) and Phase Lock Loop (PLL) are used to track the code phase and carrier frequency/phase of the incoming signal. However, the dipole antenna has no suppression to the reflected signal so the composite SNR could be very low when the direct and reflected signals are out of phase. In this case, the traditional tracking loop may lose lock. An open-loop (OL) tracking is an alternative to the traditional tracking loop that can provide additional sensitivity. The OL tracking does not use feedback loops, but rather performs repetitive acquisitions at a particular time interval. The OL tracking provides a more robust tracking approach and avoids the

need for tracking threshold and reacquisition algorithms. Another advantage of this USRP/SDR implementation is that the SNR data is available at a higher update rate than the geodetic GPS receivers (typically SNR update rate is 1 Hz), and the high-rate SNR can be averaged to obtain measurements with smaller noise.

4.1.4 Hardware Setup

An ongoing field experiment was running during February 2-4, 2012 to assess the performance of the dipole antenna for measuring the reflector height on the Table Mountain plateau of Boulder, Colorado (105°13′57.73″W, 40°7′48.46″N). A snowfall event occurred during the experiment provided the opportunity to assess its potential as a snow depth sensor. The block diagram and the instrument of the experimental setup are shown in Figure 4.3 and 4.4, respectively. The L2 dipole antenna is tipped and east-oriented, aiming to acquire the horizontally polarized components of the L2C signal of PRN 5 whose azimuth is about 180° (south).

Two data sets were collected in parallel during the experiment. The first data set contained the raw IF samples from the USRP front-end connected to the L2 dipole antenna. A Lenovo Thinkpad x220 laptop and a 1 TB hard drive were used to save the IF data. For comparison, a second data collection chain consisting of a Trimble geodetic antenna (Ashtech D/M Chokering) and a Trimble NetR9 receiver was utilized to collect a parallel data stream. The two antennas were not collocated but in relative close proximity with the geodetic antenna approximately 15 m to the SW, as shown in Figure 4.5.

4.2 Experimental Data and Results

The SNR data from the dipole antenna with bare ground is first presented, and then compared with those from the geodetic antenna. The potential of measuring snow depth using the dipole antenna SNR data is also evaluated by utilizing the snowfall event during the experimental period.

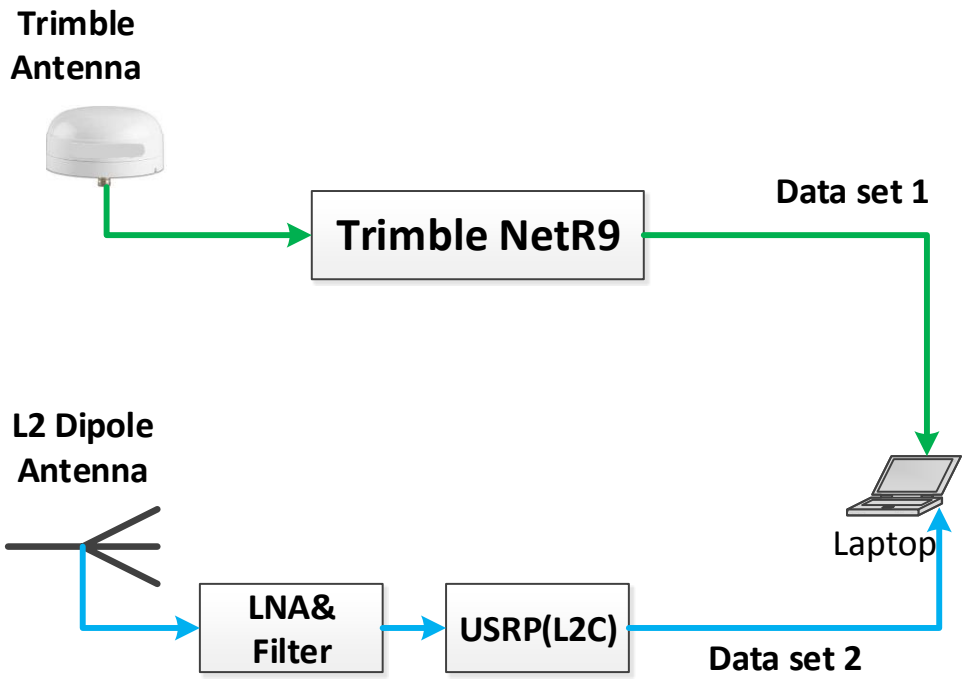

Figure 4.3: Block diagram of the data recording system for the Table Mountain experiment. One data set is from the geodetic GPS station. In parallel, the USRP collects the raw IF samples and saves them to a hard drive for post-processing.

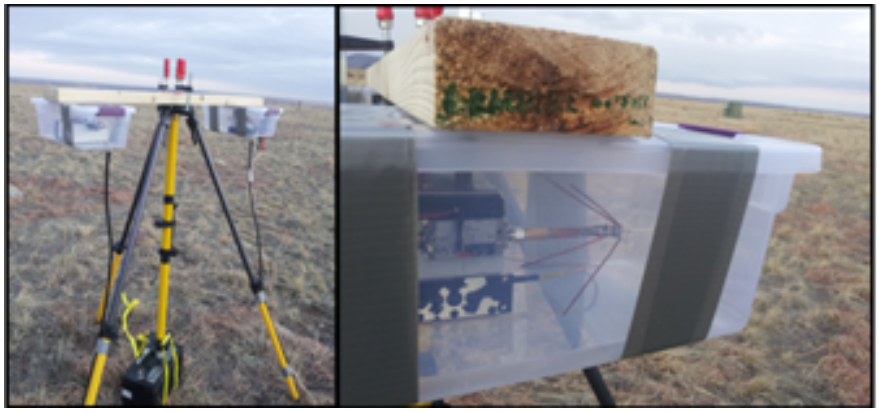

Figure 4.4: The dipole antenna was mounted on top of a tripod. The L2 dipole antenna, a low-noise amplifier (LNA) and a cavity filter were placed inside the plastic box. The dipole antenna was east-oriented, aiming to acquire the L2C signal of PRN 5.

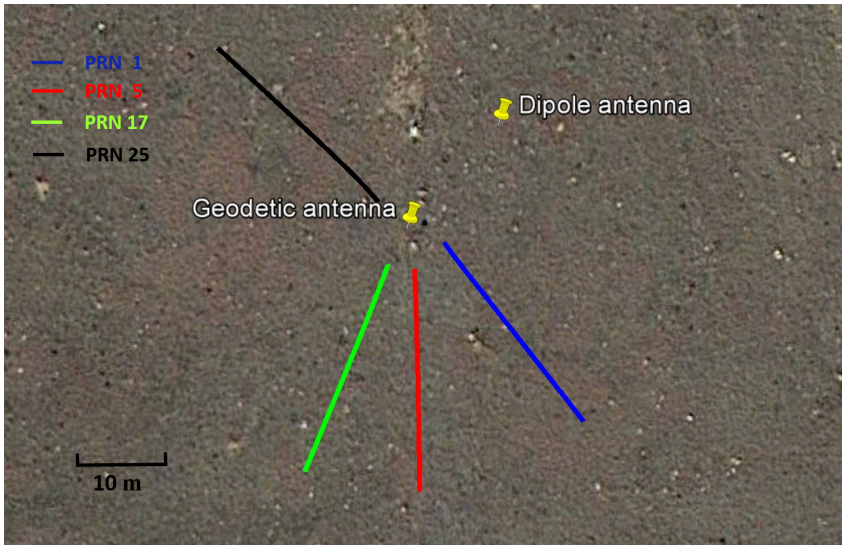

Figure 4.5: Specular ground tracks of PRN 1, 5, 17, 25. The geodetic antenna is approximately 15 m to the SW of the dipole antenna. The specular ground tracks extend from 3.5 to 23 m, corresponding to the elevation angle of 30 and 5 degrees. For a low-altitude antenna, the Earth curvature is ignored and the radial distance of the specular reflection point is approximated by $H_0/\tan e$, where H_0 is the geometric reflector height and e is the elevation angle.

4.2.1 SNR Data and LSP for Bare Ground

The geodetic L2C SNR data of PRN 1, 5, 17, 25 are presented in Figure 4.6. They are all ascending arcs and their specular ground tracks are shown in Figure 4.5. The ground tracks extend from 3.5 to 23 m in radius and the antenna height is approximately 2 m. From Figure 4.6, the interference patterns are more distinct at low elevation angles. In contrast, the oscillations diminish when elevation angles are greater than 25 degrees, implying that the reflective power is significantly attenuated. As illustrated in Chapter 2, the power of cross-polarized (LHCP) component increases as the elevation angle goes up, and the LHCP gain of the geodetic antenna is much smaller at high elevation angles. This characteristic constrains the elevation angle range that can be used for environmental parameters retrievals. Usually only the geodetic SNR data in the elevation angle range of 5 to 30 degrees are used in GPS-IR applications (Larson et al., 2009; Larson and Nievinski, 2013).

The dipole L2C SNR of PRN 5 is used to compare with the geodetic data. Unfortunately,

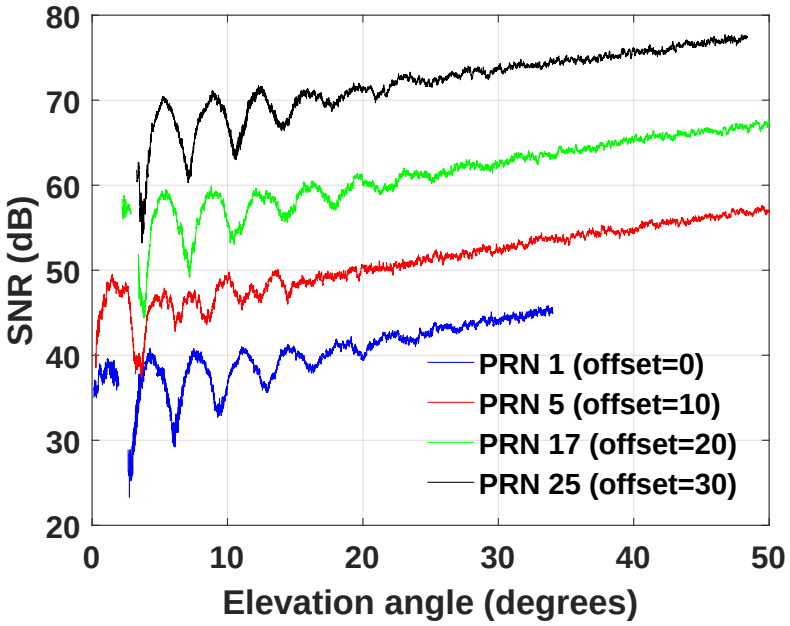

Figure 4.6: Geodetic SNR time series of PRN 1, 5, 17, 25. The interference patterns of geodetic SNR are distinct at low elevation angles, and then diminish gradually at high elevation angles. The geodetic SNR data shows a rising trend because the RHCP gain of the geodetic GPS antenna is optimized for the zenith direction.

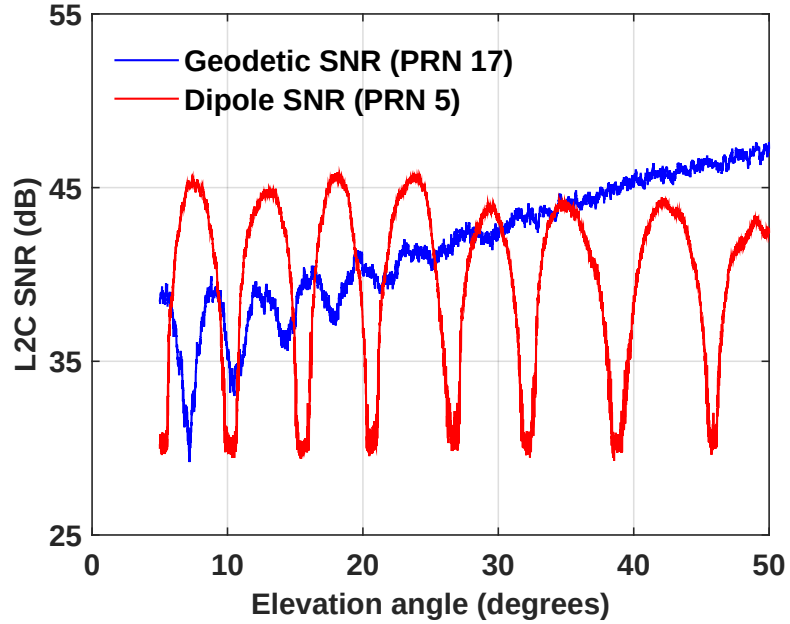

Figure 4.7: Geodetic SNR of PRN 17 vs. dipole SNR of PRN 5. The interference pattern of dipole SNR is much more distinct than the geodetic SNR data, especially at high elevation angles.

the geodetic SNR of PRN 5 has limited oscillations due to perturbations in the ground track, and thus the SNR of PRN 17 is used instead, as shown in Figure 4.7. The interference pattern of the dipole SNR is more distinct than the geodetic SNR data and more sinusoidal behaved, especially at high elevation angles.

The Lomb-Scargle Periodogram is used to translate the SNR from time domain to frequency domain. The elevation angle range is also from 5 to 30 degrees, for both SNR data sets. For the geodetic SNR data, a low-order polynomial model is used to fit and remove the rising trend, as suggested in Nievinski and Larson (2014a). For the geodetic SNR, no obvious rising or decreasing trend is observed, so the fit-and-remove processing is not required for the dipole SNR. The LSP of both data sets are presented in Figure 4.8. It is obvious that the peak of dipole SNR is sharper than geodetic SNR. The reason for the different heights is the different baseline heights/locations of each antenna. The height resolution of the LSP is 3 mm, which is much smaller than the surface roughness.

Intuitively, the dipole SNR yields a more precise reflector height estimation than the geodetic data. The 95% confidence interval (CI) using the bootstrapping resampling method (Mooney et al., 1993) is used to assess the precision of the reflector height estimation. The 95% CIs of the reflector height estimation for the geodetic and dipole SNR data are 4.9 and 9.8 mm, respectively. To comprehensively assess the performance of the geodetic data, the reflector height estimation and corresponding 95% CIs of 7 GPS satellites are listed in Table 4.1. We can see that the 95% CIs for the geodetic data are at least twice of that derived from the dipole SNR, indicating that the retrieved reflector height from dipole SNR is more precise than the geodetic SNR.

PRN	Reflector height (m)	95% CI (mm)
1	2.08	9.7
7	2.00	9.6
12	2.08	18.0
15	2.40	16.7
25	2.03	18.1
29	2.03	17.6
31	2.17	9.9

Table 4.1: Reflector height estimation and corresponding 95% CIs using the geodetic L2C SNR.

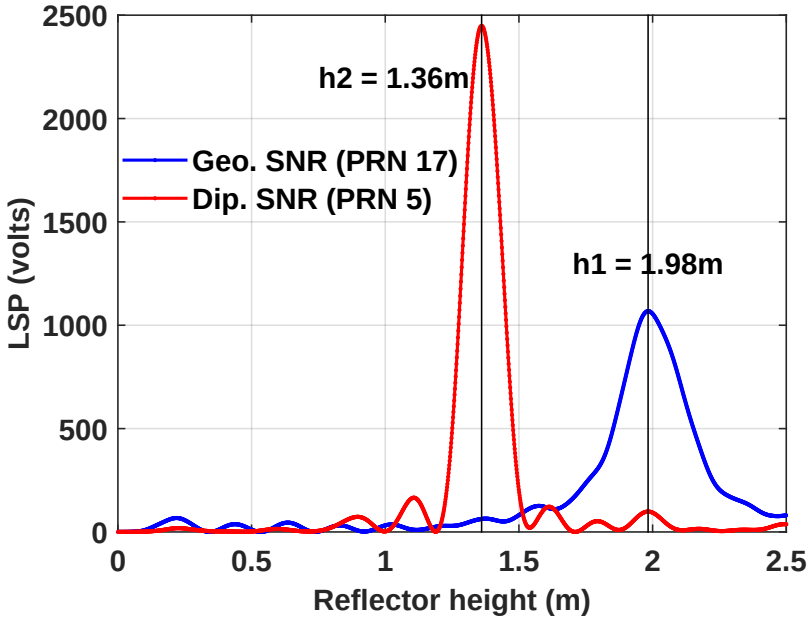

Figure 4.8: LSPs of dipole SNR and geodetic SNR. The main peak of dipole SNR is sharper than geodetic SNR, indicating a more precise reflector height estimation.

4.2.2 SNR and LSP for Snow

Taking advantage of the snowfall that occurred during the experiment, it is possible to retrieve snow depth with the dipole SNR data. The dipole SNR data of PRN 5 on the days Feb. 2 and 3, between which there was a snowfall, have been used for a comparison. The dipole SNR data of PRN 5 before and after the snowfall are presented in Figure 4.9, which clearly present an frequency change resulted from the snowfall. The LSPs for the two days' SNR data are presented in Figure 4.10, indicating a snow depth of 11.1 cm. Limited access to Table Mountain site immediately after the snowfall prevented manual verification of the snow depth. However, (1) the higher precision and low variability of the bare ground measurements from the dipole antenna and (2) the continued clear and distinct interference pattern in the SNR in the presence of snow verify the superiority of the dipole antenna design in a horizontally-polarized configuration.

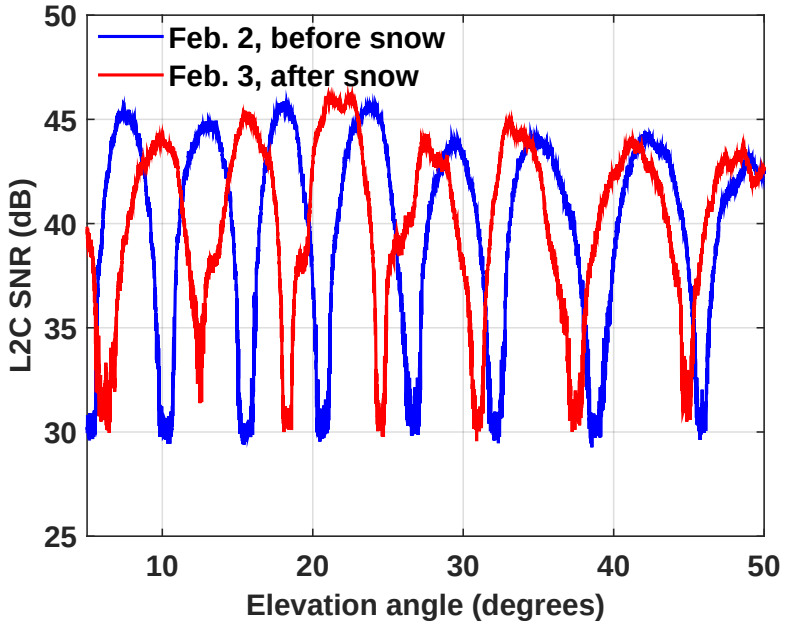

Figure 4.9: Dipole SNR data before and after a snowfall occurred during the experiment. Clear frequency change is observed, indicating a reflector height change.

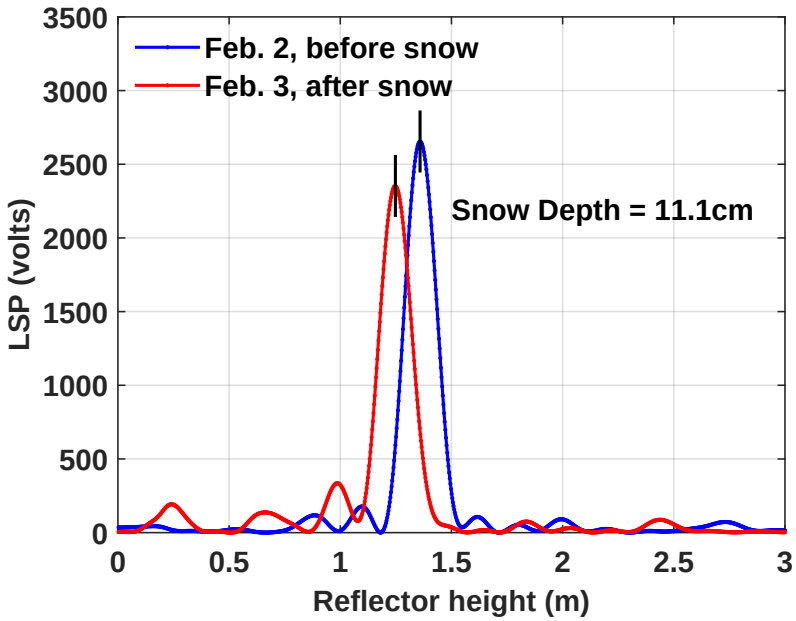

Figure 4.10: Dipole LSPs before and after a snowfall occurred during the experiment, indicating a snow depth of 11.1 cm.

4.3 Summary

In this chapter, we present an experiment carried out on Table Mountain plateau, Boulder, CO, aimed to evaluate the performance of the proposed dipole antenna in a horizontally-polarized configuration in reflector height retrieval for bare ground and snow. The experimental data clearly shows that the dipole SNR has a more distinct interference pattern than geodetic SNR, especially at high elevation angles. This characteristic yields a more precise reflector height estimation. Additionally, the extended elevation range shows the potential of collecting information from a larger footprint. The superiority of the dipole SNR data stems from two aspects: (1) The magnitude of horizontal reflection coefficient is the largest among the four considered polarizations, which means more reflection power is available for the receiving antenna; (2) The tipped dipole antenna has equal gain for both direct and ground reflected signals. A snowfall event occurred during the experiment was used to evaluate the potential of the proposed antenna in snow depth sensing, and the experimental result showed a clear frequency change (i.e. reflector height change) before and after the snowfall. Unfortunately, no *in situ* measurements were available to verify the accuracy of the snow depth retrievals. Also the experimental data was not substantial to make solid conclusion. To comprehensively evaluate the performance of the proposed design in snow depth sensing, a long-term experiment is desired.

Chapter 5

Snow Experiment 2: Marshall Field Experiment

The Table Mountain experiment preliminarily verifies the viability and superiority of the dipole antenna as applied to reflector heights retrievals. However, the limited data is not sufficient to make substantial conclusions. In order to comprehensively evaluate the performance of the proposed dipole antenna, we set up a snow sensor at the University Corporation for Atmospheric Research (UCAR) in Marshall, Colorado and carried out an experiment over the 2013-2014 water year. In this chapter, we first describe the experimental setup and then the experimental results.

5.1 Experimental Setup

5.1.1 Frequency and Receiver Selection

In the Table Mountain experiment, the L2C signal was used for snow depth measurement because of its better cross correlation property. However, presently only a subset of the GPS constellation broadcast the L2C signal. Although eventually L2C signal will be available for all the GPS satellites once the GPS modernization program is finished, for now the legacy L1 C/A signal provides better time availability and spatial coverage than the L2C signal.

Another drawback of using L2C signal is that the USRP/SDR implementation is costly and computationally expensive. The hardware cost (USRP, laptop, high-volume hard drive) is more expensive than a COST GPS L1 receiver. The huge amount of IF data streamed in is ~ 650 GB/day, so the data processing is slow under current computation resources and hinder the purpose of a long-time experiment. A COTS high-end GNSS receiver that is capable of handling the L2C signal

can get rid of the storage and computation problem, but it is also expensive (several thousand dollars).

Considering the limitation of L2C signal, it is beneficial to investigate whether the legacy L1 C/A signal can provide similar performance as the L2C signal using a low-cost COTS L1 GPS receiver. If the viability of L1 C/A signal is verified, then the spatial coverage and time availability are enlarged and the cost of installing a GPS-IR instrument is greatly decreased, which can facilitate the possible future GPS-IR network establishment.

5.1.2 Hardware Setup

A snow monitor utilizing the proposed dipole antenna and a low-cost COTS GPS L1 receiver was installed in the experiment field of UCAR, Marshall, Colorado, USA (105°12.96′W, 39°56.98′N). Because the horizontal polarization is utilized, we designate this system the Horizontal Polarization Snow Monitor (HPSM).

Figure 5.1 shows the HPSM setup and the optimal sensing area. A low-cost GlobalTop Gmm-u2P GPS evaluation board with a customized firmware to provide SNR resolved to 0.1 dB served as the GPS L1 receiver. The dipole antenna and the receiver were placed inside a PVC housing, which was water-proof and transparent to the EM wave at L1 frequency. The PVC housing was mounted on top of an aluminum post that was approximately 2.7 m above the ground, as shown in Figure 5.1(a). A Panasonic Toughbook was used to record the SNR data. The antenna orientation and sensing area are illustrated in Figure 5.1(b).

There is also an EarthScope PBO geodetic station to southeast of the HPSM, and they are about 25 m apart (Figure 5.1(b)). This geodetic GPS station includes a Trimble NetR9 receiver and a Trimble L1/L2 Dorne Margolin choke ring antenna that is about 2 m above the ground. The snow depth measurements from the geodetic receiver is publicly available from EarthScope PBO (2016). The UCAR site also has three ultrasonic SR50 snow sensors that are about 100 m south of the HPSM. In order to assist the evaluation of the snow depth measurements, we installed a camera and a labeled measurement post in the east direction (R01 and R16). An example image captured

by the camera is given in Figure 5.1(c). The snow sensor system was initiated from October 2013 and operated through May 2014. Occasional hardware failures resulted in some data loss during the experiment period.

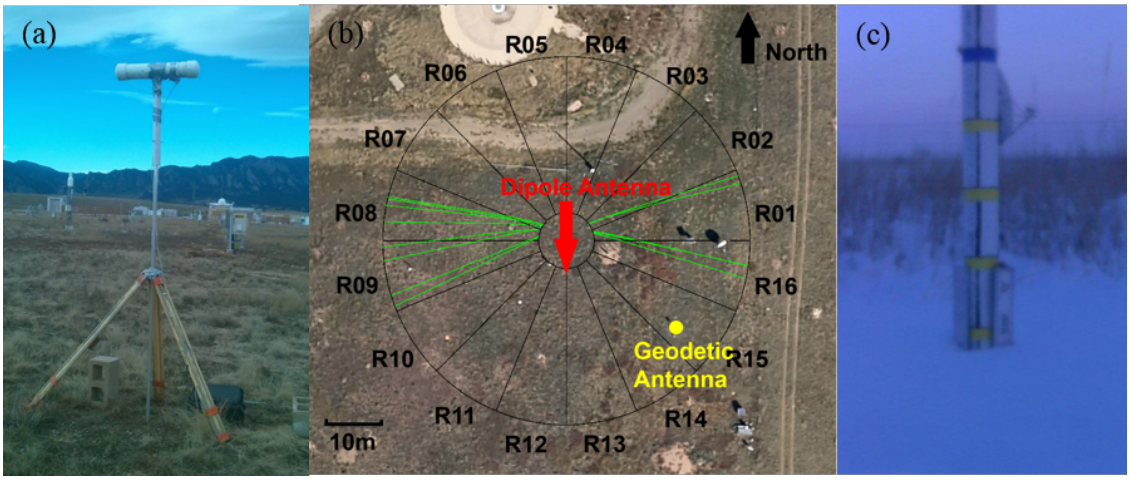

Figure 5.1: HPSM setup and sensing regions in the Marshall Field of UCAR. (a): the dipole antenna and a low-cost COTS GPS L1 receiver are inside the white PVC housing. A laptop inside the black box is used to record SNR data. (b): the dipole antenna is south oriented so the east and west regions are the optimal sensing area. The whole region is divided into 16 sectors and the 13 ground tracks located in sectors R01, R16, R08, and R09 are used to retrieve snow depth. The radii of the outer and inner rings are 30.9 and 4.7 m, respectively, corresponding to elevation angles of 5 and 30 degrees. (c): image captured by the camera. The blue label on the post is 50 cm and the interval between yellow labels is 10 cm.

5.2 Experimental Results

Before measuring snow depth, the antenna height with respect to bare soil needs to be computed using the LSP and serves as the calibration height. For each ground track, the antenna height measurements on several dry days are averaged to serve as the *j-th* calibration height H_j^{cal} (j = 1,2,...,13). For the *i-th* day (i = 1,2,3,...) and the *j-th* ground track (j= 1,2,...,13), an antenna height $H_{i,j}$ is obtained using LSP and the height difference $snow_{i,j} = H^{cal} - H_{i,j}$ is regarded as the measured snow depth for the *j-th* ground track on the *i-th* day. Then all the snow measurements

within one day are averaged to get the *i-th* day's snow depth:

$$snow_i = \frac{1}{M}\sum_{j=1}^{M} snow_{i,j} \tag{5.1}$$

where M is the number of usable ground tracks.

Considering the long duration of the experiment, it is important to verify the bare ground reflector height is stable. More specifically, the bare ground reflector height is not changing with soil moisture. In Section 2.2, the phase of the horizontal reflection coefficient is not changing with soil moisture. As a result, the reflector height estimation error caused by the phase change of the reflection coefficient is negligible. The standard deviations of bare soil reflector heights for different PRNs range from 0.5 to 0.9 cm across the entire snow-free period, which validates the simulation results. For a geodetic GPS antenna, the bare ground reflector height varies with the soil moisture change (Zavorotny et al., 2010; Larson et al., 2010; Larson and Nievinski, 2013). The Fresnel reflection coefficients of both the RHC and the LHC polarizations have a constant phase, so the variations in the effective reflector height should be attributed to the different phase responses of the geodetic antenna to RHC and LHC polarizations ($\sim$90° difference). To verify this inference, we simulate the interference phase changes because of the surface reflection and the antenna utilizing a geodetic GPS antenna's gain pattern (both RHCP and LHCP) as the input. As shown in Figure 5.2, the interference phase changes as elevation angle increases, which results in a bias in the effective reflector height. Moreover, the change rate is affected by the soil moisture level, which means that the height bias is not constant but changing with soil moisture level. If the LHCP gain is manually set to zero, then the interference phase is almost constant, meaning that the bias of effective reflector height is zero. The simulation results also indicate that the antenna working on a single dominant polarization (except vertical polarization) is more suitable for geometry-driven applications than the geodetic GPS antenna.

Some examples of the raw SNR and the corresponding LSPs before and after a snowfall are shown in Figure 5.3. The raw SNR of the three ground tracks in sector R16 on Day of Year (DoY) 306, 2013 and DoY 033, 2014 (Figure 5.3 a-c) show clear interference patterns. There was no snow

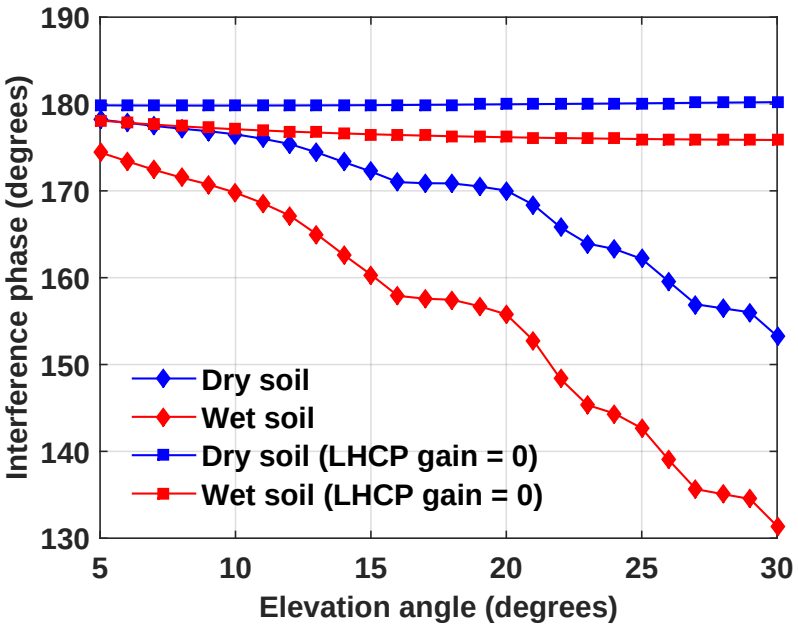

Figure 5.2: Interference phase introduced by surface reflection and antenna. For the original gain pattern of the geodetic antenna, the interference phase is changing and change rate is dependent on the soil moisture level. This characteristic gives rise to a reflector height bias. If the LHCP gain of the geodetic antenna is manually set to zero, then the phase change is almost zero. The simulation results verify that the bias in the effective reflector height is due to the considerable LHCP gain at low elevation angles.

or any other precipitation on DoY 306, 2013 but approximately 13 cm snow on DoY 033, 2014. We can clearly see a frequency change between the two days' SNR data. The interference pattern of the bare ground case is more distinct than that of the snow case, which indicates a stronger reflection power from bare soil than snow. This observation matches the simulation results in Chapter 2. In Figure 5.3 d-f, the LSPs of the three ground tracks for the two days' SNR are shown, indicating a reflector height change (i.e. snow depth) of approximately 13 cm.

The snow measurements from all four types of sensors together with the air temperature are shown in Figure 5.4. In the top panel, the uncertainties of the HPSM measurements are based on the standard deviations of snow depth retrievals. The experiment period was from November 1, 2013 through May 20, 2014. In this period, there were eleven snowfall events, both heavy and light, and each snowfall is numbered and labeled with a narrow grey bar at the beginning. There

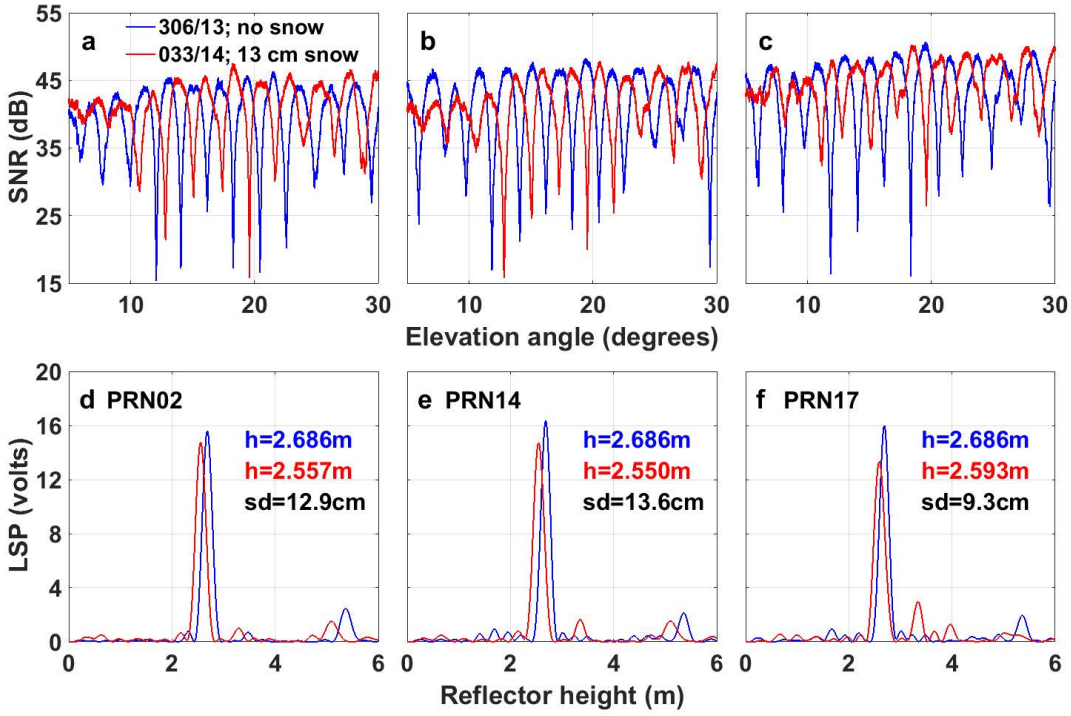

Figure 5.3: Raw SNR data and corresponding LSPs of PRN 02, 14, 17 on DoY 306, 2013 and DoY 33, 2014. Panels a-c: SNR data of the three ground tracks in sector R16. They are all rising arcs, and the azimuth angles are 71.8-95.8, 72.3-99.2, and 73.3-101.0 degrees, respectively. Panels d-f: corresponding LSPs computed for the SNR data.

was no heavy snowfall and the maximum snow depth was about 15 cm (snowfall 2 and 5). Also there were some very light snowfalls which resulted in less than 5 cm snow depth (snowfall events 3, 4, 7, 8, 9, 10).

It is worth noting that we did not implement any error checking for the HPSM snow depth measurements and nonsensical snow depths were retrieved occasionally. For example, for snowfall events 1, 3, and 4, HPSM tends to underestimate the true snow depth and even yields negative snow depth values. In contrast, for snowfall event 2, the HPSM tends to overestimate the actual snow depth as the SR50 and camera data indicate that the snow depth is decreasing while the HPSM measurements show the opposite trend. Because of the small uncertainties, it is reasonable to assume that the measurement anomalies are systematic errors instead of measurement noise. For now, we put aside the measurement anomalies and will discuss that in Section 5.3.

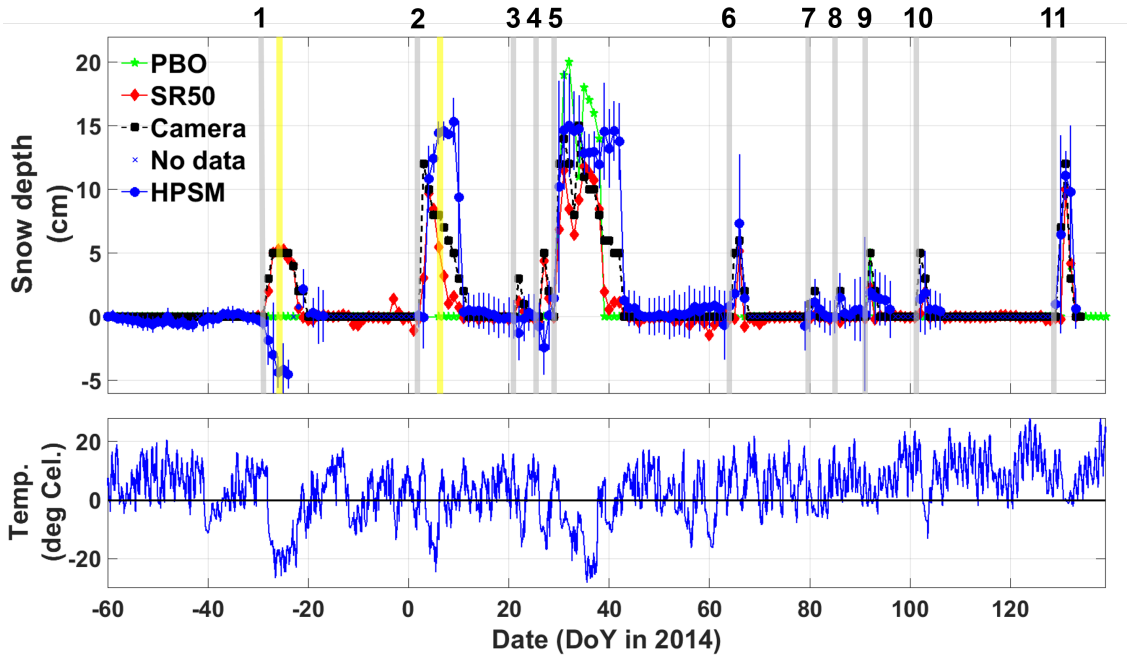

Figure 5.4: Snow depth measurements and air temperature data during the experiment period. The top panel is the snow depth measurements from the HPSM, the PBO geodetic GPS station, SR50 ultrasonic sensors, and the camera. There are 11 snowfalls during the experiment period. The beginning of each snowfall is labeled by grey bar and each snowfall is numbered. The snow conditions on the two days labeled by the yellow bars will be discussed in the next section. The error bars are based on the standard deviation of the individual measurements. The bottom panel is the air temperature. The time unit is DoY in 2014, so the days in 2013 have a negative index (e.g. DoY 0, 2014 = DoY 365, 2013).

The measurements from the camera and the SR50 sensors match up well although they are not collocated. This indicates that the spatial variations of the snow depth at Marshall Field are small and thus the measurements from the camera and SR50 sensors can serve as the ground truth data. Regardless of the measurement anomalies, we can see that the HPSM is able to detect every snowfall event, thereby indicating that the HPSM is very sensitive to even a small snow depth change. In contrast, the PBO geodetic snow sensor shows the least sensitivity by only detecting three of the snowfall events. Lacking the detailed specifics of the data processing algorithm, it is possible to speculate that the lack of snowfall detection may be a result of the lower reflection power and thus the deteriorated SNR fails to pass the quality check mechanism and cannot yield a reasonable snow depth measurement. It is also possible that the data processing algorithm, which

incorporates all possible PBO sites, outputs a zero if the derived snow depth is below a particular threshold (e.g. 5 cm).

5.3 Model Reconsideration

Although the HPSM measurement anomalies are small, these systematic errors need to be explained. In this section, the dual-interface model introduced in Chapter 2 is used to account for the anomalies. The effectiveness of the dual-interface model is validated by comparing the simulation results with the HPSM measurements for two snowfall events with significant measurement anomalies. The scatter plot of the HPSM measurements matches the simulated distribution curve. Finally, a simulated estimation error curve is demonstrated using the dual-interface model given various snow conditions, i.e. snow depths and permittivities.

5.3.1 Dual-interface Model for Snow Depth Sensing

In order to verify that the anomalies are not due to measurement noise, we show the SNR data and corresponding LSPs on DoY 340, 2013 (labeled by the left yellow bar in Figure 5.4) of sector R16 in Figure 5.5. On this day, the ground truth snow depth is about 5 cm, while the HPSM reports about -5 cm snow measurements. In Figure 5.5 d-f, the corresponding LSPs show a negative snow depth from -2.2 to -4.4 cm. In addition, the measurements in other sectors also show negative snow depth from -2.9 to -5.5 cm, which indicates that the anomalies cannot be explained by measurement noise, particularly given the clarity of the interference pattern.

Although the permittivity of snow is usually regarded as high enough so that the surface of snow acts as a single reflector, the measurement anomalies observed here indicate that single-interface reflection model might not be accurate enough to characterize reflections from the snow surface. In order to explain the measurement anomalies, we apply the dual-interface model that was originally proposed to characterize reflections from vegetation canopy to snow surface reflections. The primary difference is that the dual-interface model accounts for the effect of the underlying medium (soil), which is ignored in the single-interface model. From Figure 2.5, the phase of

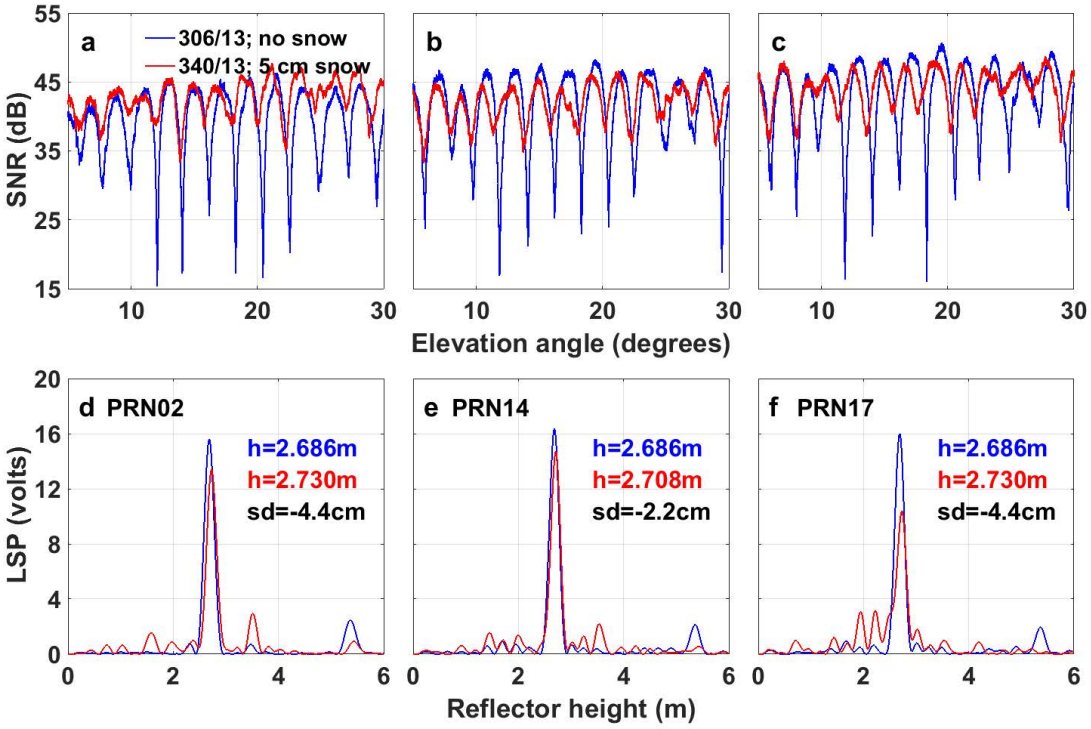

Figure 5.5: Raw SNR data and corresponding LSPs of PRN 02, 14, 17 on DoY 306 and 340, 2013. Panels a-c: SNR data of the three ground tracks in sector R16. They are all rising arcs, and the azimuth angles are 71.8-95.8, 72.3-99.2, and 73.3-101.0 degrees, respectively. Panels d-f: corresponding LSPs computed for the SNR data.

horizontal reflection coefficient is not constant because of the layering effect and the phase change would give rise to an error to the reflector height estimation, indicated by Eq. (2.10).

Some studies also employed layered model in snow sensing applications. Rodriguez-Alvarez et al. (2012a) proposed to use a vertically polarized antenna to measure snow depth. Instead of estimating the frequency of the interference pattern, they utilized the number and positions of the multiple notches of the SNR, which arise from the layering effect, to retrieve the snow depth. However, there was more than one solution corresponding to the observed notches, and ancillary snow depth data were needed to resolve the uncertainty. Jacobson (2010b, 2015) utilized a horizon-looking geodetic Trimble antenna and a layered model, i.e. snow + lake ice, to retrieve lake ice thickness using a least-square method. However, the least-square method required a priori knowledge of the environment, such as snow thickness on top of lake ice. Additionally, it could

converge to difference solutions depending on the accuracy of the a priori knowledge. Cardellach et al. (2012) employed the cross-correlation waveform, rather than the SNR, from a horizon-looking geodetic antenna as the observable. Then a spectral analysis was performed, for different time lags with respect to the direct signal, to detect the sub-structure of dry snow in Antarctica area. The technique utilized the code modulation of the GPS C/A signal on L1 frequency and it was applicable to detect layers far apart but was not suitable for closely separated layers.

Utilizing Eq. (2.17)-(2.21), we can simulate the composite reflection coefficient for horizontal polarization and then compute the LSP from the simulated data. Because the measurement anomalies were not expected, we did not make a field survey to measure the permittivities of snow and soil. However, we can use previous experiments carried out at the same location (Marshall Field, UCAR) to obtain an approximation. Zavorotny et al. (2010) use the *in situ* volumetric soil moisture (VSM) to infer a relatively stable surface soil permittivity of 4.5+0.5j at the Marshall Field, provided that the VSM is not changed significantly by precipitation. When the temperature is below 0 $^{\circ}C$, the complex permittivity of soil, both real and imaginary components, can have a reduction as the temperature decreases due to the freezing of water (Hallikainen et al., 1985; Mironov et al., 2010). For the relatively dry soil in Marshall, the impact of temperature change is not as significant as densely wet soil. For the dual-interface model used in this study, a soil permittivity value from 4.0+0j to 4.5+0.5j is a reasonable approximation. For the snow in the experiment location, a permittivity value from 1.4 to 1.8 is a reasonable approximation – the imaginary part of snow permittivity is usually small enough to be neglected (Tiuri et al., 1984). In the simulation, the permittivities of the snow and soil medium are set to be 1.5+0.001j and 4.3+0.3j, respectively.

Figure 5.6 shows the horizontal reflection coefficients with a 5-cm snow layer under both single-interface and dual-interface models and the corresponding LSPs. In Figure 5.6(a), we can see that the amplitude is smaller than that of the single-interface model, which would cause the fringes of the SNR interference pattern to be less distinct. More notably, the phase is no longer constant but increases as the elevation angle increases. This changing phase would introduce a reflector height bias as illustrated by Eq. (2.10). The LSP using the dual-interface model assuming

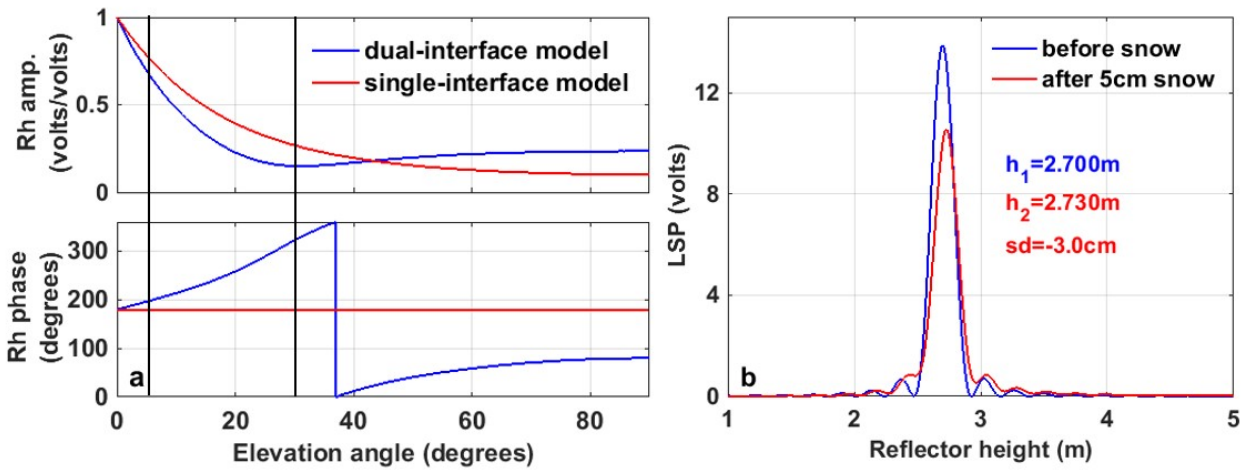

Figure 5.6: Reflection coefficients and LSPs using the dual-interface model with a 5-cm snow layer. Panel a: horizontal reflection coefficients for the dual-interface model and the single-interface model. Panel b: LSPs corresponding to the bare soil and 5-cm snow are simulated using the dual-interface model. The simulated snow depth estimation is -3.0 cm while the actual snow depth is 5 cm. The elevation angle range used to calculate LSP is from 5 to 30 degrees (between the dark bars).

a 5-cm snow layer is given in Figure 5.6(b). The antenna height above the bare soil ground is 2.7 m and its LSP shows a strong frequency component at h = 2.7 m. Adding a 5-cm snow layer, the LSP shows a frequency component at h = 2.73 m, resulting in a -3.0 cm snow depth while the actual geometric antenna height is 2.65 m. The simulated LSPs match those of the ground tracks in R16 as shown in Figure 5.5.

5.3.2 Model Verification and Error Curve

Another anomaly in the HPSM snow measurements is the 2nd snowfall event. The HPSM obviously overestimates the snow depth compared to the ground truth data. Again we will look at the LSPs of the actual data and see whether they match the simulation results. In Figure 5.7, SNR data and LSPs of the three ground tracks in R16 on DoY 6, 2014 (labeled by the right yellow bar in Figure 5.4) are shown. The HPSM snow depth measurement is about 12.5 cm and the ground truth is about 7 cm.

In the simulation, the antenna height with respect to bare soil surface is 2.7 m and then

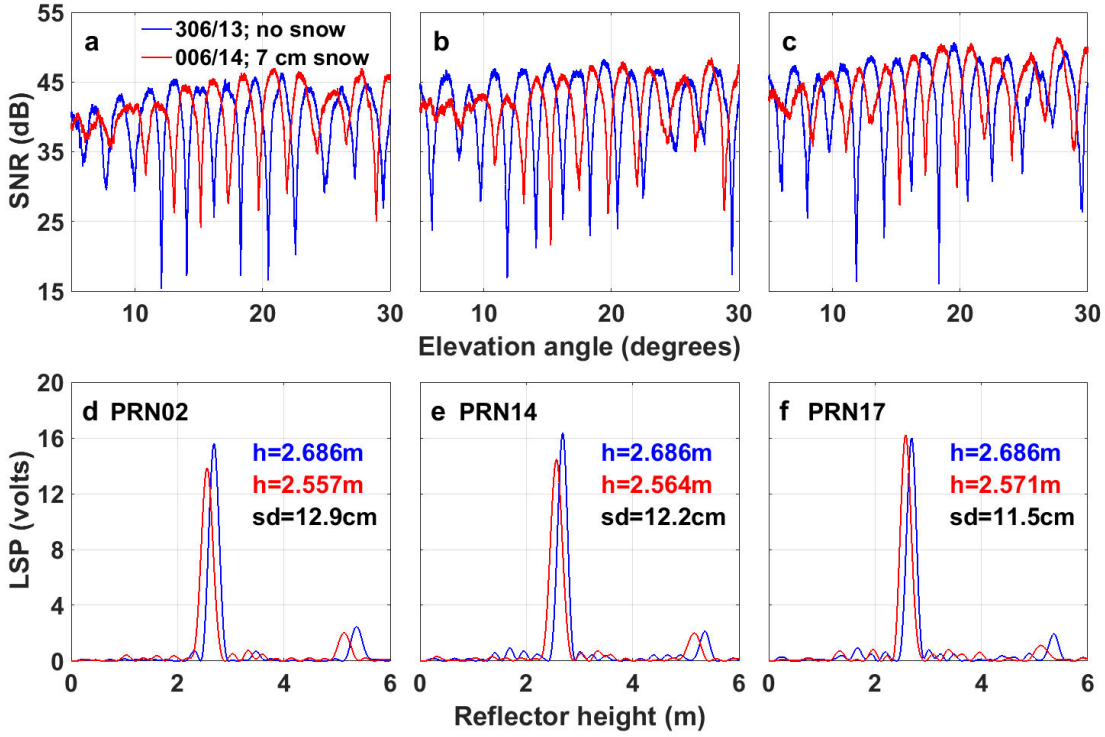

Figure 5.7: Raw SNR data and corresponding LSPs of PRN 02, 14, 17 on DoY 306, 2013 and DoY 6, 2014. Panels a-c: SNR data of the three ground tracks in sector R16. Panels d-f: corresponding LSPs computed for the SNR data.

a 7-cm snow layer is added. The same permittivities of snow and soil are used as those in the previous simulation. The simulated composite reflection coefficients and the LSPs are shown in Figure 5.8. Instead of increasing with elevation angle, the phase of the reflection coefficient shows a decreasing trend with the elevation angle in the selected elevation angle range (5 to 30 degrees). This decreasing trend introduces a negative bias to the antenna height estimation and thus makes the snow depth overestimated. From Figure 5.8(b), we can see that the simulated LSPs match those of the observed data in Figure 5.7 and the estimated snow depths are close.

With the ground truth data, we can see whether or not the HPSM snow depth measurements match the simulated distribution. In Figure 5.9, we superimpose the scatter plot of snow measurements on the error curve of $\epsilon_r = 1.5$. The x-axis of the scatter plot is the ground truth data, and the y-axis is the HPSM snow depth measurements. The elevation angle cutoff range is from 5 to 30 degrees. We can see that the distribution of the HPSM snow depth measurements

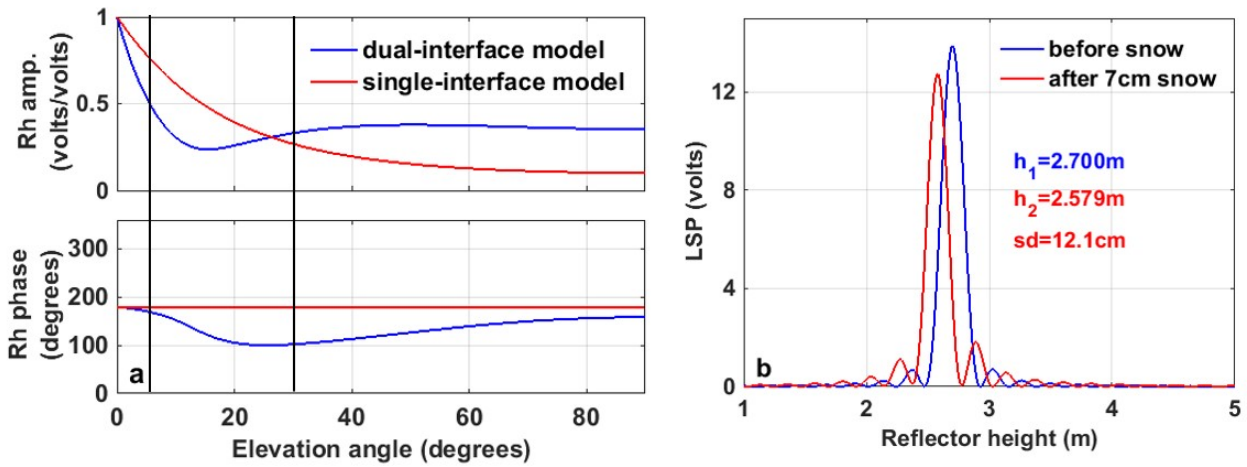

Figure 5.8: Reflection coefficients and LSPs using the dual-interface model for a 7-cm snow layer. Panel a: horizontal reflection coefficients for the dual-interface model and the single-interface model for a 7-cm snow layer. Panel b: LSPs corresponding to the bare soil and 7-cm snow are simulated using the dual-interface model. The simulated snow depth estimation is 12.1 cm while the actual snow depth is 7 cm. The elevation angle range used to calculate LSP is from 5 to 30 degrees (between the dark bars).

follows the simulated results. From Figure 5.6 and 5.8, we can see that the changing rate of the reflection coefficient phase is not constant across the entire elevation angle range, indicating that the snow depth retrievals could be different if other elevation angle cutoffs are used. In order to further validate the dual-interface model, we re-calculate the snow depth measurements from the SNR data using a higher elevation angle range from 15 to 50 degrees. The scatter plot together with the simulated error curve are shown in Figure 5.10, which also indicates good agreement between the HPSM measurements and simulation results.

It is clearly seen that the soil layer can cause a bias, either positive or negative, to the reflector height estimation. The estimation error is related to the depth of the snow layer as well as its permittivity. In order to understand the effect of the snow layer's depth and permittivity on the estimation errors, we simulate the estimation errors over a range of snow depth and the permittivity values. The error curve is shown in Figure 5.11. We can see that the estimated snow depth varies around the true snow depth and the error is decreasing with the increment of snow depth. Also the estimation error decreases with increasing permittivity of snow layer. This is reasonable because

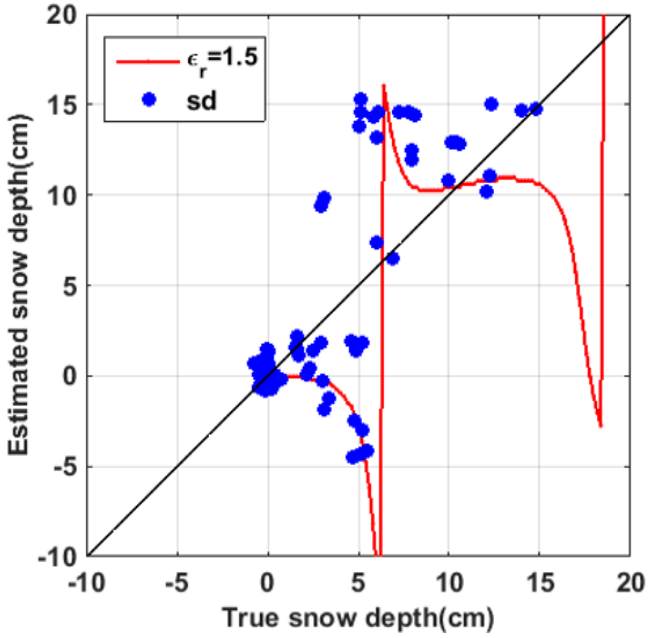

Figure 5.9: Simulated and observed snow depth measurements distribution. The blue dots are the scatter plots of retrieved snow depth vs. ground truth. The red curve is the estimated snow depth corresponding to $\epsilon_r = 1.5$. The elevation angle range is from 5 to 30 degrees.

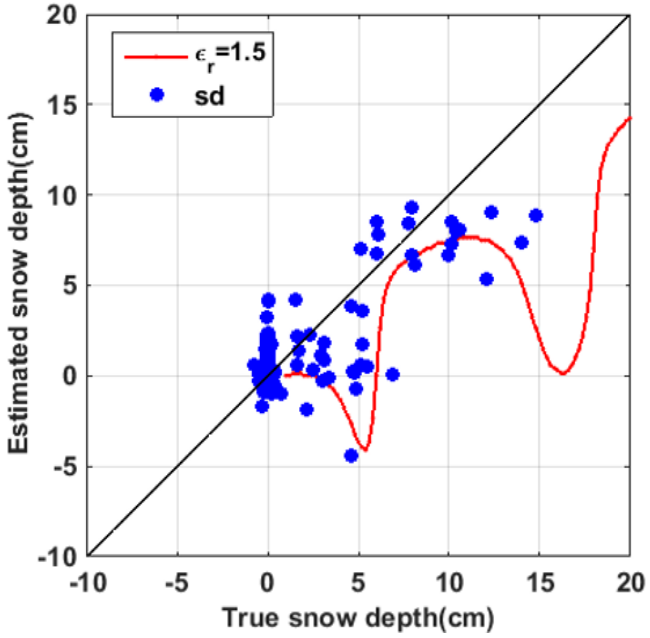

Figure 5.10: Simulated and observed snow depth measurements distribution. The blue dots are the scatter plots of retrieved snow depth vs. ground truth. The red curve is the estimated snow depth corresponding to $\epsilon_r = 1.5$. The elevation angle range is form 15 to 50 degrees.

a greater snow permittivity would allocate more energy to the first interface reflection and less to the bottom interface reflection. As a result, the bottom interface reflected EM wave would have less influence on the top interface bounced EM wave, which is closer to the single-interface model.

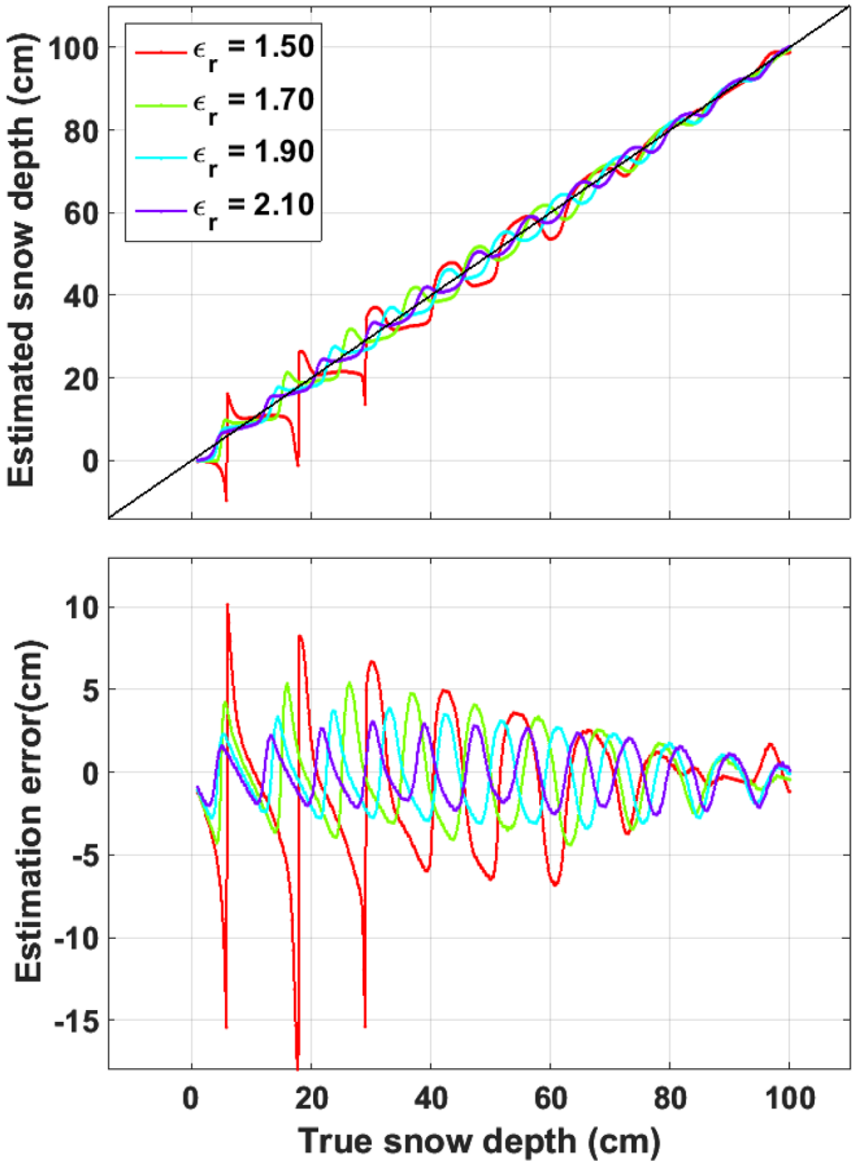

Figure 5.11: Snow depth estimation and estimation errors for various snow conditions, i.e. snow depth and permittivity. The top panel is the estimated snow depth vs. true snow depth for various snow permittivity values. The elevation angle range used for reflector height retrieval is from 5 to 30 degrees. The bottom panel is estimation error.

5.4 Summary

This chapter documents an experiment conducted at Marshall, CO, USA during the 2013-2014 water year, aimed to comprehensively assess the performance a dipole antenna and a COTS GPS L1 receiver for snow depth sensing. The developed instrument, designated as HPSM, shows higher sensitivity to light snowfalls which should be attributed to the horizontal polarization and improved gain pattern of the antenna developed. In order to explain the observed measurement anomalies, we utilize the dual-interface model that accounts for the effect of the underlying medium and simulate the horizontal reflection coefficients. The phase of the horizontal reflection coefficient is changing as elevation angle increases, which gives rise to an estimation bias of the reflector height. In order to validate the proposed model, we simulate the LSPs for two snowfall events that encounter obvious measurement anomalies. The simulation results match the observed LSPs. The scatter plots of the HPSM measurements, for two different elevation angle ranges, match well with the simulated distributions, and thereby further validate the dual-interface model. With the dual-interface model, we simulate the estimation error curve for various snow depths and permittivities, and find that the estimation error decreases if the snow layer thickness and permittivity increase.

Chapter 6

Snow Experiment 3: SPL Experiment

The two experiments presented in Chapters 4 and 5 validate the superiority and effectiveness of the proposed horizontally-polarized (H-pol) dipole antenna as applied to snow depth sensing in plain areas. Most GPS-IR snow experiments were conducted in topographically flat sites (Larson et al., 2009; Rodriguez-Alvarez et al., 2012a; Jacobson, 2014; McCreight et al., 2014; Chen et al., 2014, 2016). However, Gutmann et al. (2012) evaluated the accuracy of snow depth measurements using the geodetic SNR at the Niwot Ridge saddle, Colorado, USA – an area that includes topographic variations and considerable snow roughness. They concluded that GPS-IR can measure snow depth in an alpine environment with an accuracy of 9 to 13 cm. The experimental data showed that the results of the western GPS tracks, where the terrain was not as planar as it was in other directions, did not match the manual *in situ* and Lidar measurements of snow depth. Gutmann et al. suggested that the large-scale undulations and the small-scale roughness of the snow surface might be the reason for the considerable measurement errors. Jacobson (2014) incorporated the tilt angle of the surface into the model and employed a nonlinear least-square fit algorithm to estimate snow depth and SWE. However, the model also assumed that the surface was planar, although not horizontal, and the nonlinear least-square fit required a priori information about the environment (e.g. snow depth, snow density). In addition, the duration of the experiment was only a single day, which was not sufficiently long to make substantial conclusions about the effectiveness of the proposed algorithm and configuration. Given that the alpine area stores most of the snowpack, it is significantly important to further investigate the feasibility of snow sensing using GPS-IR technique

in such area.

This chapter presents an experiment conducted at the mountain-top Storm Peak Laboratory (SPL) in Steamboat Springs, Colorado, USA. This experiment aims to investigate the accuracy of measuring snow depth using the GPS-IR technique in an alpine environment. Two aspects of the site make this investigation challenging: (1) the surface tilt angle is relatively large (5-6 degrees) and varies when there is snow. (2) The region is very windy, which creates significant snow drifting and surface roughness. Additional challenges are associated with site infrastructure. The antenna is attached to the porch railing of the SPL, and thus the SPL itself is another source of reflections, resulting in a distortion to the ground reflected signals. The proposed H-pol patch antenna in Chapter 3 is utilized to suppress the reflections from the SPL structure. In this chapter, we first describe the adaptions made to the forward model of GPS-IR, which takes the tilt angle of the snow surface into account. Then we present the effect on snow depth estimation and the estimation algorithm of the tilt angle. In addition, the algorithm of using the estimated tilt angle to calibrate the retrieved snow depth is presented. The experimental setup and data processing method then follow. The experimental results show that there are considerable retrieval errors of snow depth introduced by the variant surface tilt angles. The calibrated snow depth retrievals show significant improvements in both accuracy and precision of the snow depth measurements.

6.1 Theoretical Analysis

6.1.1 Adapted forward model of GPS-IR

The SNR, incorporating the direct and the horizontal surface reflected signals, is formulated as (see Figure 6.1(a)):

$$SNR = \frac{P_d + P_r + 2\sqrt{P_d P_r}\cos\left(2\pi f_m \sin e + \phi\right)}{P_n} \tag{6.1}$$

As indicated in Figure 6.1(b), if the reflecting surface is not horizontal but tilted, Eq. (6.1) is adapted to

$$SNR = \frac{P_d + P_r + 2\sqrt{P_d P_r}\cos\left(2\pi f_m \sin(e + \alpha) + \phi\right)}{P_n} \tag{6.2}$$

where α is the tilt angle of the reflecting surface. The elevation angle e is calculated with respect to an imaginary horizon and the grazing angle γ amounts to the sum of the elevation angle and the surface tilt angle, i.e., $\gamma = e+\alpha$. Here α is positive for ascending terrain and negative for descending terrain. The LSP-derived antenna height H_1 is the perpendicular distance from the antenna to the reflecting surface, and is related to the vertical antenna height H_0 by $H_1 = H_0 \cos\alpha$. The difference between H_1 and H_0 is minor, provided that the tilt angle is relatively small ($\cos 8^\circ = 0.99$). However, the surface tilt angle α has a significant impact on the phase pattern of the observed SNR. When α is small, SNR is approximated by

$$SNR \approx \left(P_d + P_r + 2\sqrt{P_d P_r}\cos\left(2\pi f_m \sin e + 2\pi\alpha f_m \cos e + \pi\right)\right)/P_n \tag{6.3}$$

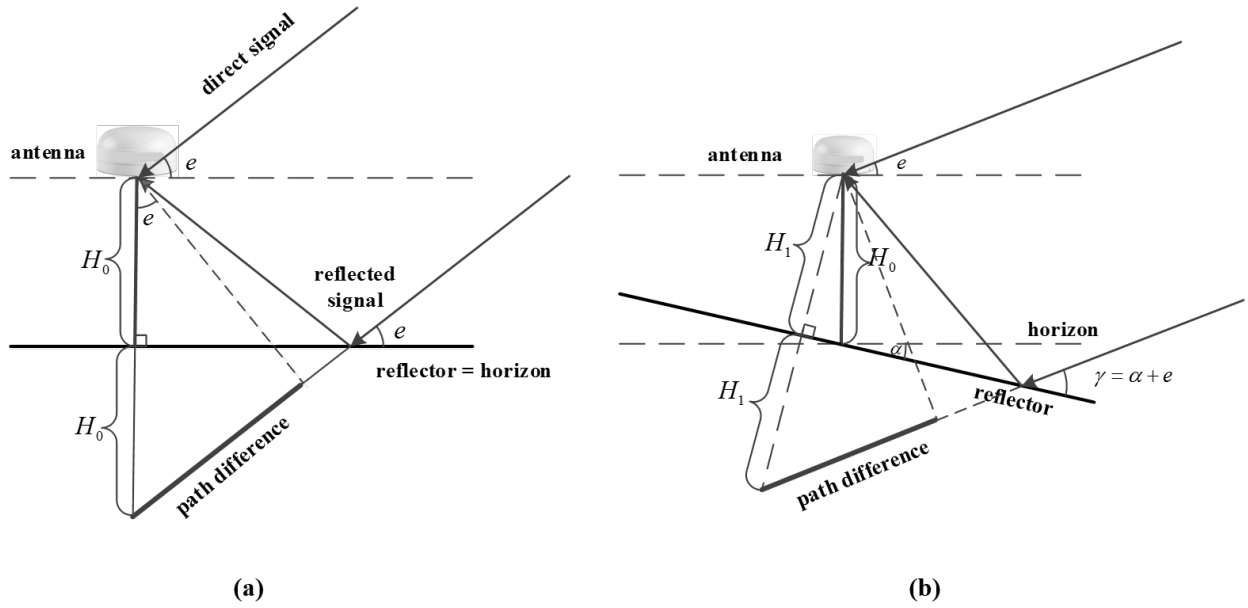

Figure 6.1: (a) Geometry of GPS-IR for horizontal reflector. The grazing angle of the incident wave amounts to the elevation angle calculated from GPS almanac or ephemeris. (b) Geometry of GPS-IR for tilted reflector. The grazing angle $\gamma = \alpha + e$. The LSP-derived antenna height is no longer the vertical antenna height, but the perpendicular distance from the antenna to the reflecting surface.

From Eq. (6.3), we can see that the tilt angle α brings in a phase offset $\beta = 2\pi\alpha f_m \cos e \approx 2\pi\alpha f_m$. The phase offset increases as the tilt angle α or the perpendicular antenna height H_1 increases. The effect of tilt angle α on the phase pattern of SNR is illustrated in Figure 6.2. We

can see that the SNR phase pattern is obviously changed, while the frequency change is minor or even negligible. The sensitivity of phase change to tilt angle indicates that the relationship can be used to estimate the surface tilt angle. However, two different tilt angles might yield the same phase shift because of the periodicity of the sinusoidal function, resulting in an ambiguity problem in the estimation of the surface tilt angle. An approximation of the ambiguity repeatability is

$$\delta\alpha = \frac{\lambda}{2H_1}\frac{180}{\pi}\ deg \tag{6.4}$$

provided that the elevation angle is not large. The repeatability of a 2-m high antenna is 2.7 degrees, which matches the simulation result in Figure 6.2.

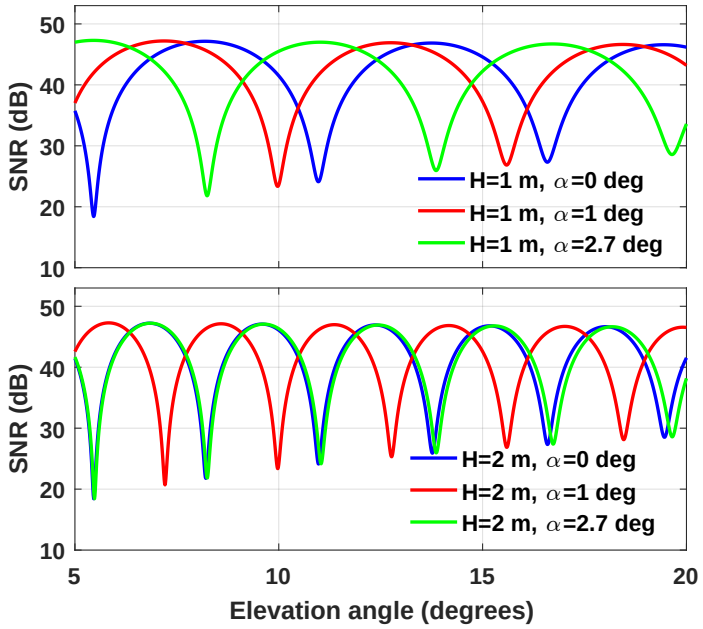

Figure 6.2: The effect of surface tilt angle on the phase pattern of SNR. The tilt angle has an impact on the phase of the SNR interference pattern. A positive tilt angle moves the SNR left and a negative tilt angle moves the SNR right.

6.1.2 Effect of tilted terrain on snow depth retrievals

Tilted terrain affects the accuracy of GPS-IR snow depth retrievals. Larson and Nievinski (2013) simulated the retrieval errors of the LSP-derived snow depth with a 2-m antenna and a variety of snow depth levels and surface tilt angles. The tilt angles of the ground and snow surfaces

were assumed to be identical, i.e., the snow surface and underlying ground surface were parallel. Here, we re-simulate the effect of tilted surface on snow depth retrievals assuming that the antenna height is 5 m and the elevation angle range is 5 to 20 degrees, both of which are close to the actual conditions of the experimental setting. The obtained snow depth retrieval errors are illustrated in Figure 6.3. The simulation results show that for a 5-m antenna, the snow depth retrieval errors range from a few cm to 1 dm when the terrain tilt angles are relatively small (smaller than 6 degrees). Compared with the results in Larson and Nievinski (2013), the retrieval errors are enlarged because of the greater antenna height (5 m vs. 2 m). The retrieval errors arise from two aspects: (1) the LSP-derived antenna height is the perpendicular distance from the antenna to the reflecting surface, not the vertical distance; (2) the input of LSP should be $\sin(e+\alpha)$, but the actual input is $\sin e$ if the tilt angle α is unknown. This results in a small distortion to the intervals between samples. The errors introduced by these two factors are minor, especially at low elevation angles.

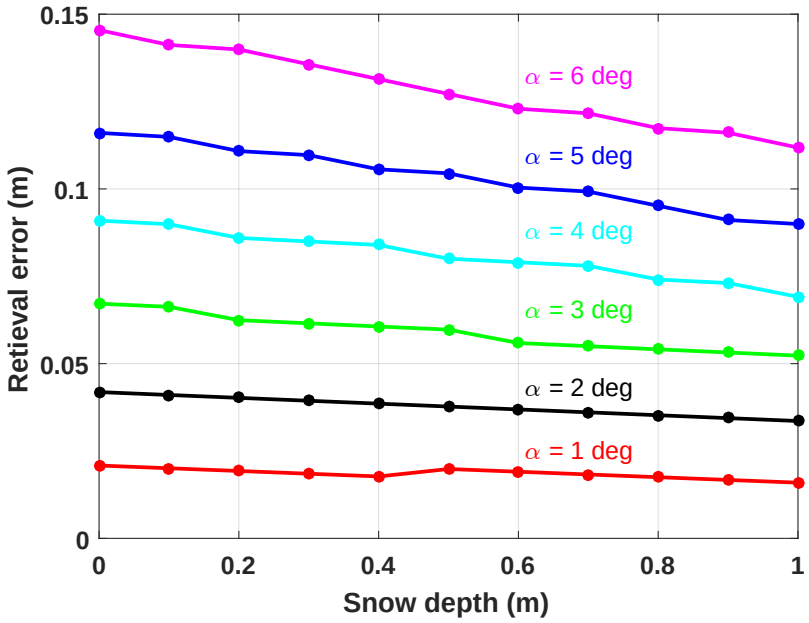

Figure 6.3: Effect of terrain tilt angles on snow depth retrievals. The antenna height is 5 m above the ground, which is close to the experimental setting introduced in Section 6.2. The snow and ground surfaces are parallel. Only positive tilt angles are simulated here, corresponding to the mountain-top terrain of the experiment.

For the actual terrain conditions, the snow surface and ground surface might not be parallel.

Here, we vary the tilt angle of the snow surface while keeping the ground tilt angle at 5 degrees. The snow surface tilt angle varies from -2 to 2 degrees relative to the ground surface. The obtained errors in snow depth retrievals are presented in Figure 6.4. We can see that a variant tilt angle of snow surface can greatly enlarge the retrieval error of the snow depth. The retrieval error increases from several cm to several dm, or even more than 1 m. For example, for 1-m snow, the retrieved snow depth might be close to 0 if the snow surface has a relative tilt angle of -2 degrees. Figure 6.5 explains the reason for the considerable errors: for the parallel case, the change of H_{eff} indicates the actual snow depth; however, if the snow surface has a non-zero relative angle with respect to the ground surface, the change of H_{eff} is not the actual snow depth. Again, the H_{eff} is the perpendicular distance from the antenna to the reflecting surface. The error can be approximated by $x \cdot \tan(\delta\alpha)$, where x is the horizontal distance from the specular reflection point to the antenna. The experimental results presented in Section 6.3 validate the retrieval errors introduced by the variant tilt angles of the snow surface.

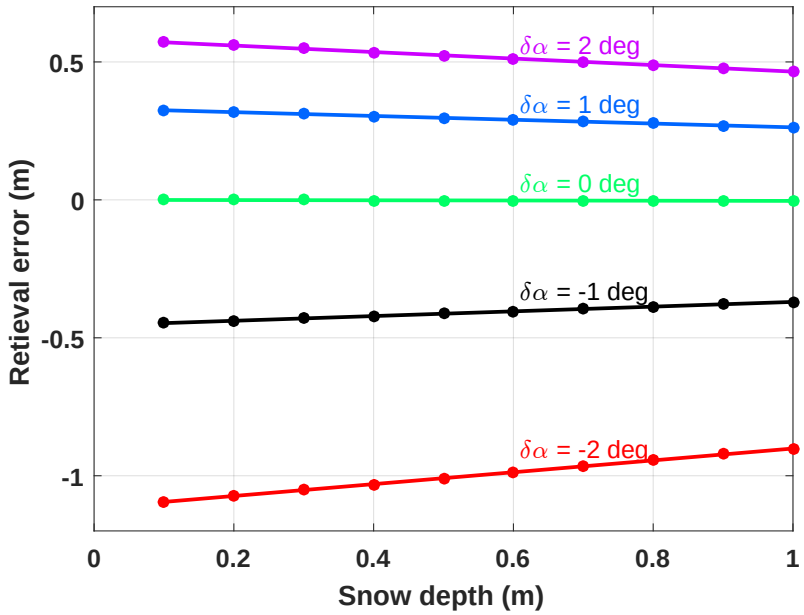

Figure 6.4: Effect of variant tilt angle of snow surface on snow depth retrievals. The tilt angle of the ground surface is fixed to be 5 degrees. $\delta\alpha$ is the relative snow surface tilt angle with respect to the ground surface and varies from -2 to 2 degrees.

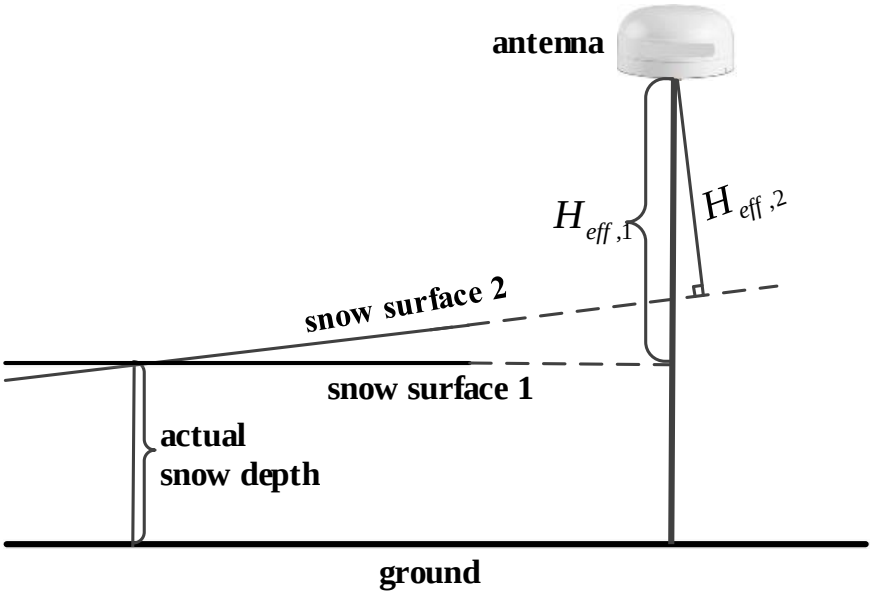

Figure 6.5: The snow surface with a non-zero relative tilt angle with respect to the ground surface can significantly change the effective antenna height, and introduces a considerable retrieval error of snow depth.

6.1.3 Tilt angle estimation algorithm and effective antenna height calibration

The variant surface tilt angle can introduce considerable errors to GPS-IR snow depth measurements, so it is reasonable to estimate the surface tilt angle and use this information to calibrate the LSP-derived snow depth measurements. It is demonstrated that the tilt angle has an impact on the phase pattern of the observed SNR. Here, we propose an algorithm to estimate the surface tilt angle α. The procedures are as follows:

- Obtain the LSP of the SNR time series, and get the most distinct frequency component f_m.
- Use least-square fit to obtain the estimate of the interference phase $\phi = 2\pi\alpha f_m \cos e + \pi$ with the estimated f_m as input.Then the tilt angle α can be obtained by

$$\alpha = \frac{\phi + (2k+1)\pi}{2\pi f_m \cos e}, k = 0, \pm 1, \pm 2, ... \tag{6.5}$$

- Determine the appropriate k value and the corresponding tilt angle α, i.e., resolve the tilt angle ambiguity.

The ambiguity of the tilt angle has to be resolved if we want to utilize this tilt angle to calibrate the effective antenna height. The resolving algorithm is presented in Section 6.3.

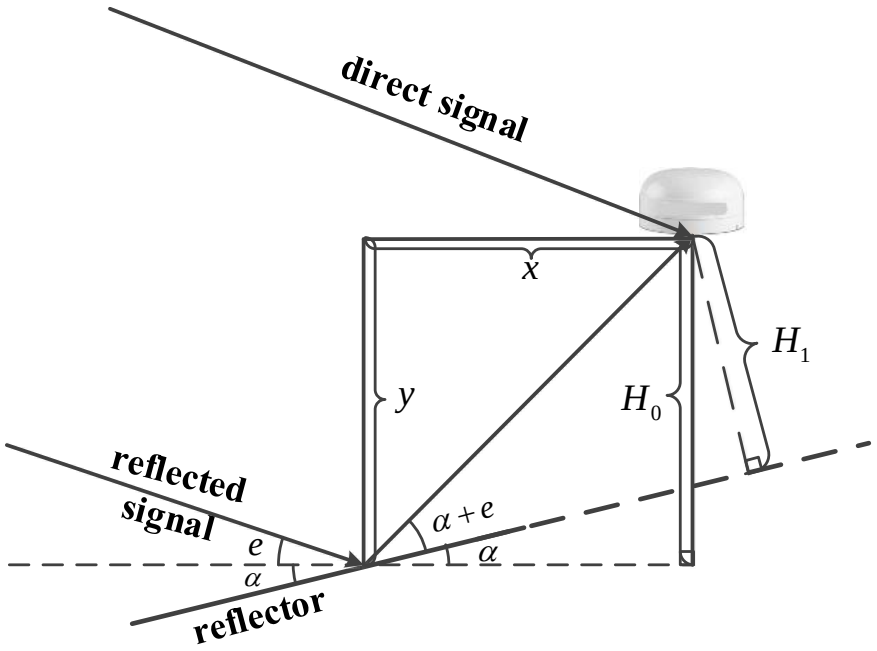

Figure 6.6: The variations of surface tilt angle can affect the effective antenna height H_1. For a particular reflecting point, the effective antenna height is H_1. To obtain H_0, the tilt angle estimation is required. This can be derived from the phase pattern of the observed SNR.

For a particular reflection point, the tilt angle has a significant effect on the effective perpendicular antenna height H_1 while the metric of interest is the vertical antenna height H_0 , as shown in Figure 6.6. The large-scale undulations (several meters to tens of meters) of the snow surface can vary the local tilt angle and thus the perpendicular antenna height H_1. However, from H_1 we can derive the horizontal and vertical distances from the specular reflection point to the antenna:

$$y = H_1 \frac{\sin(e+2\alpha)}{\sin(e+\alpha)} = H_0 \tag{6.6}$$

$$x = H_1 \frac{\cos(e+2\alpha)}{\sin(e+\alpha)} \tag{6.7}$$

If the tilt angle α can be estimated, then the vertical antenna height H_0 at a horizontal distance x can be obtained from the LSP-derived perpendicular antenna height H_1 .

6.2 Experimental Setup and Data Processing Algorithm

6.2.1 Experimental Setup

As shown in Figure 6.7(a), the H-pol patch antenna was mounted to the porch railing of the SPL roof, which was ∼5 m above the ground, in order to make use of the existing power supply and remote connectivity. We installed three measurement posts with 10-cm scale marks to the southwest of the antenna in order to provide *in situ* snow depth measurements. A HD-relay live camera was used to take snapshots of the field to record the *in situ* snow depth data. The positions of the measurement posts are indicated in Figure 6.7(b). The experiment instruments were installed on February 10, 2015 when the snow was ∼1 m deep, and was operational until July when the snow completely melted. The SPL structure affects the redistribution of snow by wind, leading to much deeper snow close to the laboratory than in farther away areas (see Figure 6.7(a)). For example, snow depth at the closest post to the SPL structure was over 2 m on April 1, but closer to 1m at the other posts. A manual depth survey, which was conducted on June 1, at 37 points throughout the sensing footprint showed that the snow depth values near the first post formed a considerable rising gradient due to drifting. For this reason, the measurement of the post that was closest to the structure was excluded and only the measurements from two further posts were used to generate the *in situ* snow depth data.

The digital elevation maps (DEM) around the antenna installation from U.S. Geological Survey (USGS) is given in Figure 6.8. The spatial resolution of DEM is ∼10 m. The derived surface tilt angle is approximately 5 to 6 degrees in the southwest direction, which is the optimal sensing area. The first Fresnel zone (FFZ), which is the sensing footprint of GPS-IR, is illustrated in Figure 6.9. The FFZ is an elongated ellipse with a relatively constant semi-minor. The semi-major of the FFZ in the radial direction depends on the antenna height and elevation angle. Figure 6.9 shows the FFZ with a 5-m antenna for elevation angles from 5 to 20 degrees. The tilt angle of the ground is incorporated when generating the FFZ.

The SPL structure also serves as a reflector of the GPS signals as well as the ground surface.

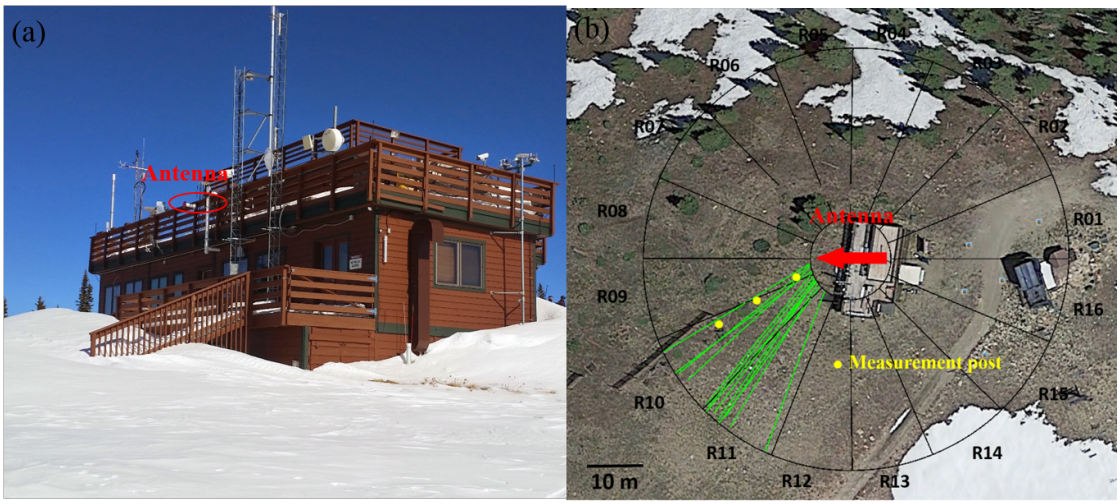

Figure 6.7: (a) Photograph of the Storm Peak Laboratory on the day of instrument installation. The antenna is mounted to the porch trailing of the SPL roof. (b) Ground tracks (specular reflection points) in the optimal sensing area and the positions of the three measurement posts. R10 and R11 are selected because they are located in the high gain area of the patch antenna.

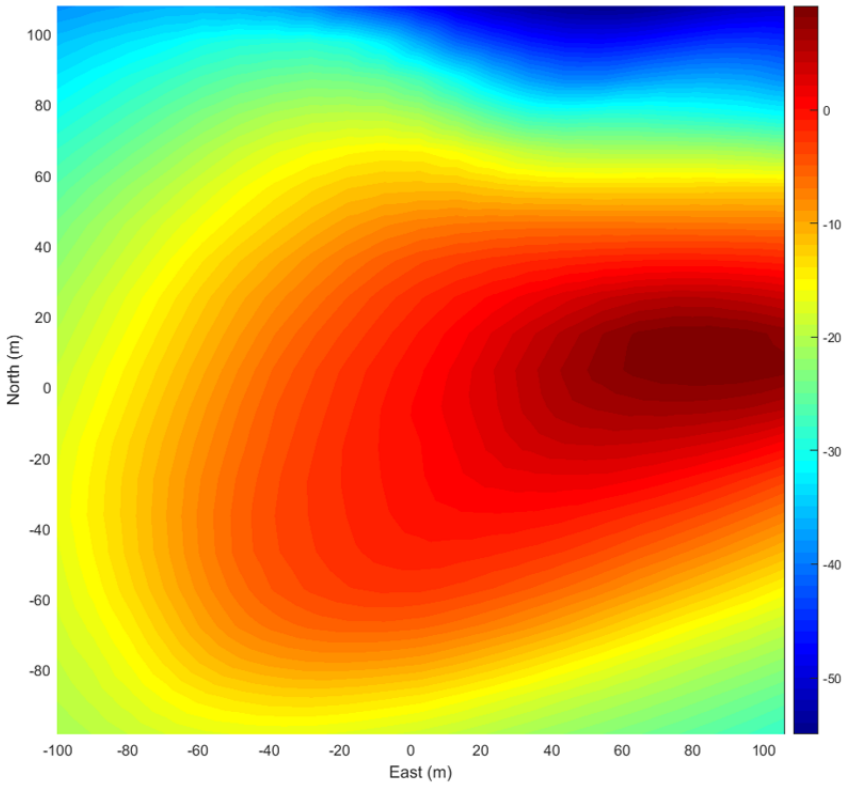

Figure 6.8: Digital elevation map around the antenna installation. The antenna is located at the origin.

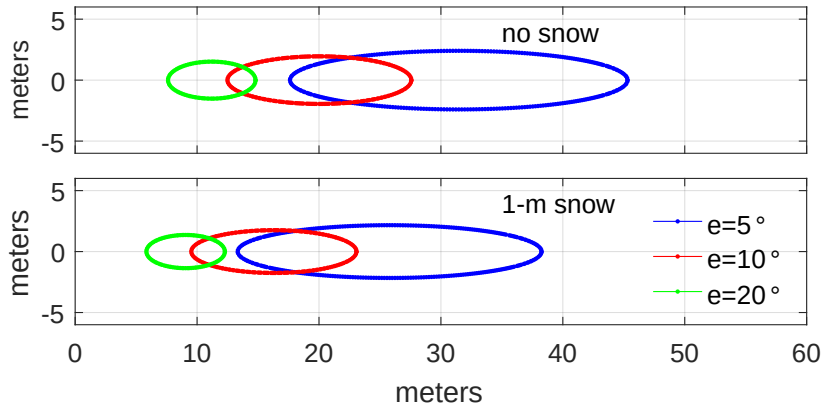

Figure 6.9: First Fresnel zones for elevation angles from 5 to 20 degrees. The antenna height is 5 m above bare ground. The top panel assumes no snow and the bottom panel assumes 1-m snow.

In this situation, the dipole antenna is not suitable for this environment because its gain pattern has no suppression to the backward multipath or reflections. To utilize the dipole antenna, we have to mount the dipole antenna sufficiently far from the SPL to eliminate the multipath from the structure. This installation option greatly increases the difficulties of antenna mounting, power supply, and connectivity maintenance. In this situation, an H-pol patch antenna is used instead. Figure 6.10 illustrates the gain patterns of the dipole antenna and the proposed patch antenna. The dipole antenna shows a uniform gain with elevation angles, and thus has a considerable reception to the structure reflected signal as well as the ground reflected signal. In contrast, the horizon-looking patch antenna also has a nearly uniform gain at its main lobe that is beneficial to receive the ground reflected signal, while the small back lobe suppresses the reflections off the structure. In fact, the dipole antenna was first deployed to test whether or not it could provide high-quality SNR data, and it was then changed to the patch antenna because of the low-quality SNR. Two SNR arcs of PRN 22 in R10, from the dipole antenna and the patch antenna respectively, are presented in Figure 6.11 Although the two SNR arcs were not collected on the same day, they are good representatives of the entire dipole and patch SNR data sets, respectively. The dipole SNR is completely blurred and shows no clear interference pattern all over the observed elevation angle range, while the patch SNR shows a relatively distinct interference pattern at low elevation angles. The gain pattern difference

between the two antenna types should be attributed to the better backward multipath rejection of the patch antenna. It also demonstrates that the patch antenna is a better option than the dipole antenna for measuring snow depth in complex multipath environment.

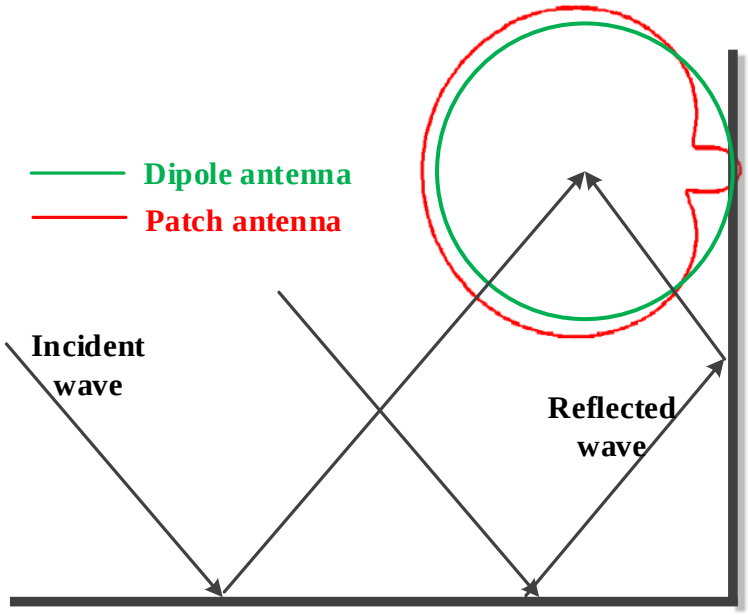

Figure 6.10: Sketch of gain patterns of the dipole antenna and the H-pol patch antenna. The patch antenna has a small back lobe and thus is desired to mitigate the reflections from the structure.

6.2.2 Data Processing Algorithm

We demonstrated that a variant snow surface tilt angle can give rise to considerable errors in the snow depth measurement. In Section 6.1.3, we propose an algorithm to estimate the surface tilt angle. The estimated surface tilt angle is then used to calibrate the LSP-derived effective antenna height. Here, we summarize the data processing procedure as follows:

- For each SNR time series in the optimal sensing area, select an appropriate elevation angle range where the SNR shows distinct interference pattern. More specifically, the power level differences of the maxima and minima in the selected elevation angle range should be greater than 15 dB. Sometimes a manual adjustment of the elevation angle range is needed, especially when the automatic selected elevation angle range contains many

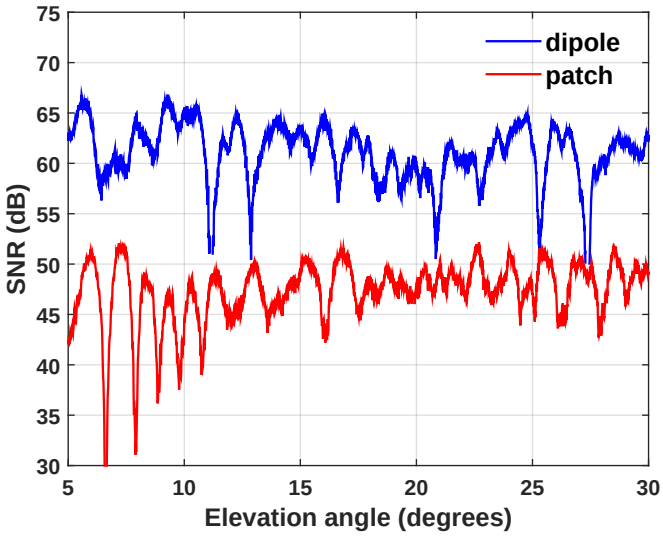

Figure 6.11: Dipole SNR and patch SNR of PRN 22 in R10. The two SNR arcs were collected on DoY 122, 2014 and DoY 122, 2015, respectively. Although these two SNR arcs are corresponding to difference snow conditions, they are good representatives of dipole SNR and patch SNR data sets, respectively.

frequency components.

- Estimate tilt angle for the selected SNR segment using the procedures presented in Section 6.1.3. Again, the estimation of the tilt angle has an ambiguity problem, i.e. more than one tilt angle can result in the observed phase shift.

- For each tilt angle candidate, use Eqs. (6.6) and (6.7) to compute the vertical and horizontal distances from the reflecting point to the antenna. This results in an estimated tilted surface segment corresponding to the selected elevation angle range.

- The spatial correlation of adjacent ground tracks are used to resolve the ambiguity. The basic idea is that the vertical antenna heights at the same horizontal distance derived from the adjacent ground tracks should be close. Then a non-ambiguous vertical antenna height can be given by

$$H = \arg \sum_{i=1}^{N} \min_{j} |H - H_{i,j}| \tag{6.8}$$

where N is the number of ground tracks, $H_{i,j}$ is the calibrated vertical antenna height of

the i-th ground track and the j-th tilt angle. In the Section 6.3.2, we will show how the ambiguity resolution algorithm works.

6.3 Experimental Results

6.3.1 Snow depth measurements without tilt angle calibration

As mentioned previously, the instrument was installed and operated from February to July when the snow completely melted. As a result, the bare soil antenna height was not available to calculate the actual snow depth until the end of the experiment. In Figure 6.12, two representatives of the raw SNR time series and the corresponding LSPs on DoY 171 (bare soil) and 080 (∼1 m snow) are presented. For the bare soil case, the SNR time series show a clear interference pattern and the LSP has a unique distinct peak at 5.1 m. However, for the 1-m snow case, the interference pattern of the SNR time series is blurred and it is difficult to identify a primary peak in the LSP. Although there are two relatively distinct peaks, the derived snow depth from either peak is more than 2 m, which is far from the *in situ* snow depth measurements. It is worth noting that the SNR interference patterns on the snow days are also distinct, at least for some elevation angle range.

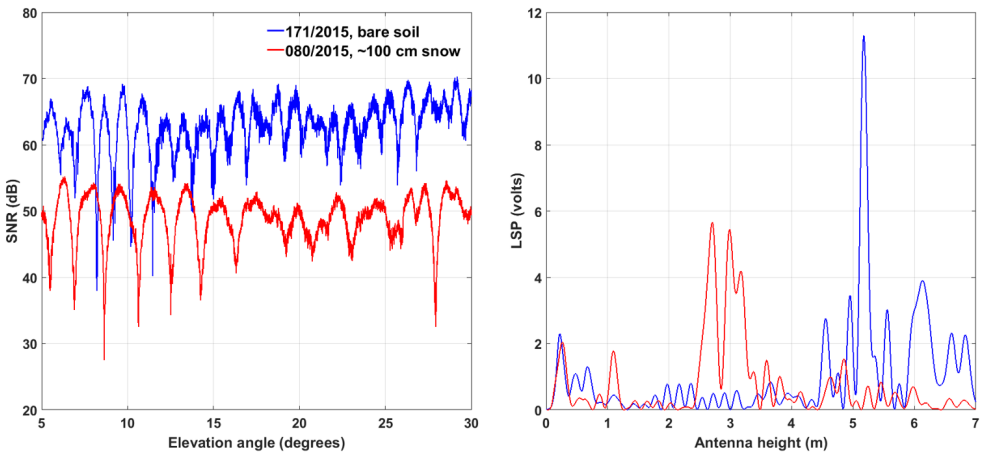

Figure 6.12: SNR time series and corresponding LSPs of PRN 07 in R10 for DoY 171 and 080, 2015. There is no snow on DoY 171 and 1 m snow on DoY 080. The SNR shows a clear interference pattern for bare soil, but is blurred when snow exists.

In Figure 6.13, the LSP-derived snow depth measurements, together with the *in situ* mea-

surements, are presented. We can clearly see that in general the LSP-derived GPS snow depth measurements do not match the *in situ* measurements. At the beginning of the experiment, the GPS snow depth measurements swing around zero and have large error bars, while the actual snow depth is ∼0.8 m. After DoY 60, the GPS snow depth measurements follow the trend of the *in situ* measurements although with a relatively constant bias. At the melting stage (after DoY 145), GPS snow depth measurements reflect the melting process and match the *in situ* measurements, although still with a constant bias. These considerable measurement errors cannot be explained by a constant tilt angle of the terrain, because the retrieval error introduced by a constant surface tilt angle is on the level of several cm, as illustrated in Figure 6.3. Instead, a variant surface tilt angle can result in retrieval errors on meter level, which is likely the reason for the observed retrieval errors.

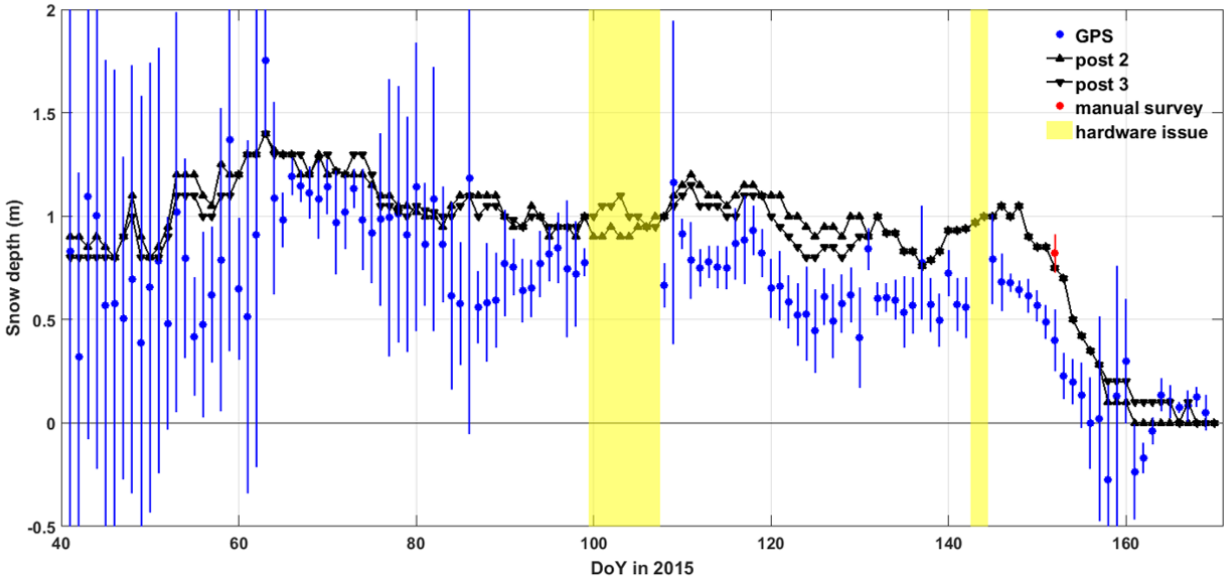

Figure 6.13: Time series of the LSP-derived snow depth and *in situ* measurements. The error bars are based on the standard deviation of the measurements. During the days 100-107 and 143-144, the GPS data is missing because of hardware issues.

6.3.2 Snow depth measurements calibrated with tilt angle

In this section, we try to estimate the surface tilt angle and then use the estimated tilt angle to calibrate the LSP-derived snow depth. The tilt angle of the sow surface, which is superimposed on the bare ground, is assumed to be in the range of ± 2 degrees relative to the ground surface, which is 3 to 7 degrees for this experimental site. Prior to estimating snow depth, the bare ground tilt angle needs to be resolved first. As shown in Figure 6.14(a), the bare ground SNR data of PRN 01 on DoY 170 shows a clear interference pattern between 5 and 13 degrees and this data segment is selected for further data processing. With the LSP-derived frequency f_m, a least-square fit algorithm is used to estimate the phase of the interference pattern. Then a series of tilt angles are estimated from the interference phase. In Figure 6.14(b), the effects of the tilt angle on the phase pattern of the observed SNR are illustrated: the reconstructed SNR time series with horizontal surface have a phase mismatch with the observed SNR segment, while an appropriate tilt angle is able to eliminate the mismatch. As mentioned previously, there might be more than one tilt angle that can generate the observed interference pattern and thus the ambiguity problem has to be resolved.

We use the algorithm proposed in Section 6.2 to resolve the tilt angle ambiguity of the bare ground terrain. As indicated in Figure 6.15, each ground track in R11 has a solution in the ellipse area. The estimated tilt angles of the four tracks range from 5.2 to 5.6 degrees, which fall into the range derived from the DEM. In this study, we use the terrain slopes encompassed by the ellipse as the actual ground terrain. Using similar processing procedure, the estimated snow surface segments for each of the four ground tracks on DoY 080 are shown in Figure 6.16. Again, each ground track has a solution in the ellipse area. By comparing Figures 6.15 and 6.16, it is easy to obtain a snow depth of $\sim$1 m. To facilitate resolving the ambiguity, a snow depth search range can be determined first. The search range of the *n-th* day is based on the resolved snow depth of the previous day $snow_{n-1}$: $[snow_{n-1} - 0.2, snow_{n-1} + 0.7]$, assuming that the snow depth cannot increase more than 0.7 m or decrease more than 0.2 m within two consecutive days because of snowfall or melting,

respectively. The empirical search range might vary from site to site.

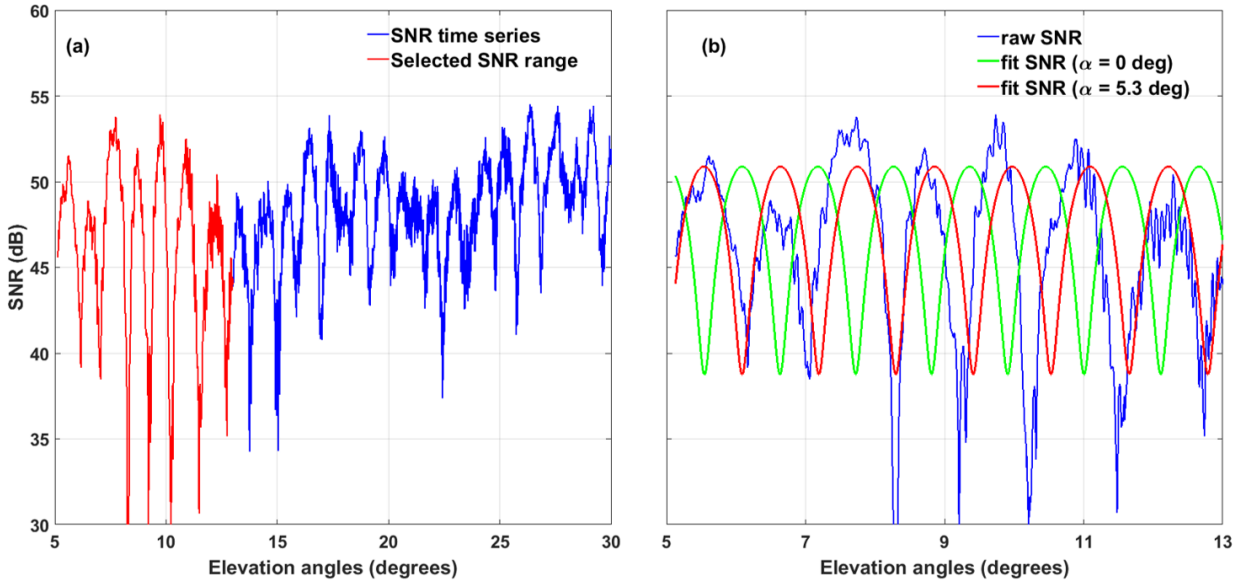

Figure 6.14: (a) SNR time series of PRN 01 on DoY 170. The elevation angle range of 5 to 13 degrees is selected for further data processing because of its distinct interference pattern. (b) Use the selected elevation angle range for data processing. The LSP-derived frequency is used to do the least-square fit. The green curve is the reconstructed SNR using 0 tilt angle while the red curve is constructed using the estimated tilt angle (5.3 degrees).

The calibrated snow depth measurements, together with the post measurements and the manual survey measurement, are presented in the top panel of Figure 6.17. The error bars are based on the standard deviation of the individual measurements. The calibrated snow depth measurements match well with the *in situ* post measurements, yielding a RMSE of 14 cm. Compared with Figure 6.13, the calibrated snow depth measurements have much smaller error bars and improved accuracy. The large estimation biases for the first twenty days are eliminated. In addition, the calibrated measurements can keep tracking of the decreasing trend (e.g. DoY 65 to 83, 148 to 161) and the increasing trend (e.g. DoY 109 to 112) of the *in situ* snow depth measurements. We can also see that the proposed ambiguity resolving algorithm fails to yield a solution on some days, primarily because not enough snow depth candidates fall into the search range. In this situation, we use the post measurements to determine the search range of the next day. The bottom panel of Figure 6.17 shows the average of the resolved relative surface tilt angles with respect to the ground surface.

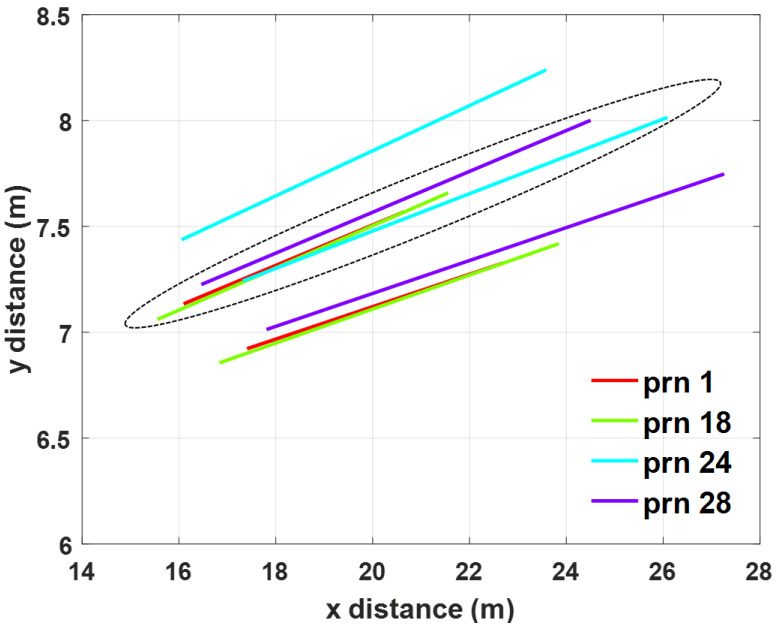

Figure 6.15: Resolved bare ground terrains from PRN 1, 18, 24, 28 in R11 on DoY 170. Different elevation angle ranges are selected for different PRNs, thus different terrain segments are obtained.

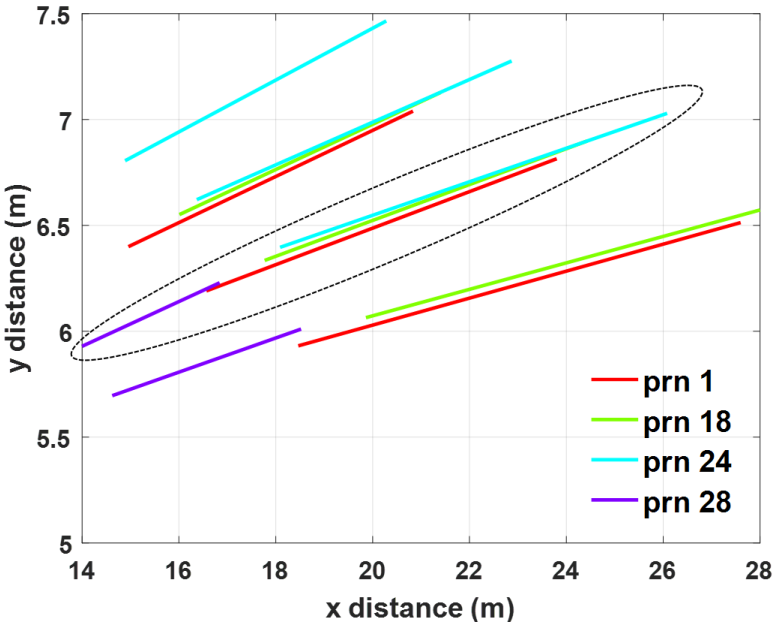

Figure 6.16: Resolved snow surface terrains from PRN 1, 18, 24, 28 in R11 on DoY 080. It is not difficult to obtain the snow depth is ∼1 m (e.g. by comparing the vertical distance at x = 20).

The manual survey on DoY 152 provides a rough estimation of snow surface tilt angle. The survey

was along the line of the three measurement posts, yielding a relative surface tilt angle of 0.7-1.4 degrees. Figure 6.6 shows that a positive relative tilt angle results in a positive error of snow depth retrieval. The ground track of PRN 07 in sector R10 is close to the footprint of the manual survey. The LSP-derived snow depth of PRN 07 is 1.6 m, which is much greater than *in situ* measurement (∼0.8 m) and thus agrees with the simulation result. The resolved relative surface tilt angle is 0.9 degrees, which falls into the range derived from the manual survey.

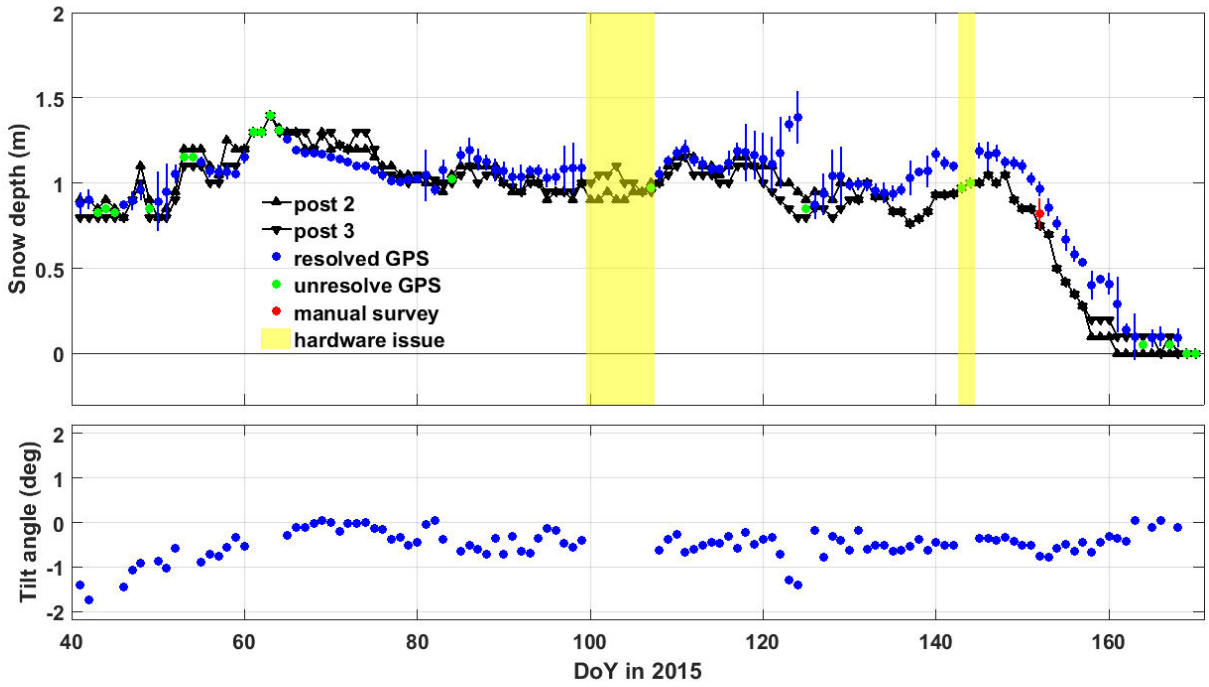

Figure 6.17: The top panel is the calibrated snow depth measurements and estimated surface tilt angle. Compared with LSP-derived snow depth, the calibrated measurements improves the measurement accuracy and precision significantly. Occasionally the proposed algorithm fails to resolve the ambiguity. The bottom panel is the estimated relative tilt angle of the snow surface.

6.4 Summary

In this chapter, we conducted a five-month experiment at the mountain-top SPL aiming to investigate the accuracy of snow depth measurement using the GPS-IR technique in an alpine environment. To suppress the reflections from the SPL structure, we utilized an H-pol patch antenna mounted to porch railing of the SPL roof. The experimental results show that the LSP-derived

snow depth measurements have considerable errors, which are likely due to the variant tilt angles of the snow surface. We add the tilt angle of the reflecting surface into the GPS-IR forward model and propose an algorithm to estimate the tilt angle from the interference phase information. The estimated tilt angle is used to calculate the vertical antenna height. Because of the periodicity of the SNR interference pattern, more than one tilt angle can result in the observed SNR interference pattern and thus add the difficulty of estimating tilt angle. In general, the calibrated GPS snow depth measurements and the *in situ* measurements match up well with a RMSE of 14 cm. The experiment results show the potential and effectiveness of the proposed algorithm in an alpine environment. However, the limitations of the algorithm in resolving vertical snow depth is also observed occasionally. In the future, more experiment campaigns are needed to make a conclusion of the feasibility of snow depth measurements via GPS-IR in alpine areas.

Chapter 7

Vegetation State and Soil Moisture Sensing

Soil moisture and vegetation water content (VWC) are two key parameters for the studies of hydrological and carbon cycles. Information of both variables is required by hydrology, climatology, and agriculture for understanding the hydrological interaction between land surfaces and the atmosphere, prediction of potential flood hazards and drought, crops yield estimation, and understanding the carbon cycle processes (Jackson and Schmugge, 1991; Atlas et al., 1993; Western et al., 2004; Sitch et al., 2008). A variety of microwave remote sensing techniques, both active and passive, have been developed for estimating soil moisture and VWC in global or local scale (Brakke et al., 1981; Njoku and Entekhabi, 1996; De Roo et al., 2001; Njoku et al., 2002).

The permittivity or dielectric constant of water at L-band is at least one order of magnitude greater than that of dry soil or vegetation. Therefore, the amount of water stored in soil or vegetation can be detected by measuring the dielectric properties of corresponding medium. The passive microwave remote sensing technique, i.e. radiometer, measures the brightness temperature of the surface medium (vegetation or soil) to retrieve the emissivity. Then the soil moisture or vegetation optical depth (VOD) can be retrieved from the brightness temperature measurements. The radiometric measurements are influenced by the diurnal temperature fluctuations of the vegetation canopy or soil surface. The active microwave remote sensing technique, i.e. radar, measures the scattering coefficient or backscatter cross section from which the vegetation biomass (and VWC) and soil moisture can be derived. Njoku and Oneill (1982) demonstrated that the P-band (0.775 GHz) and the L-band (1.4 GHz) signals are optimal for remotely sensing soil moisture in the top

0-4 and 0-2 cm layer, respectively. The L-band radar also shows sensitivity across a VWC range of 0-5 kg/m^2 (Kim et al., 2012). A number of space missions (e.g. SMOS, AMSR-E, SMAP) have been launched to provide global-scale soil moisture and VWC measurements (Entekhabi et al., 2008; Brown et al., 2011; Jackson et al., 2012).

As a L-band bistatic radar technique, GNSS-R has also been applied to soil moisture and vegetation state sensing. For the conventional GNSS-R approach (dual-antenna configuration, air- or space-borne), Masters and Katzberg carried out the first GNSS-R soil moisture remote sensing experiment (SMEX02) (Masters et al., 2004; Katzberg et al., 2006). The SNR of the cross-polarized (LHCP) signal was used as the observable and the experimental results showed good agreement with *in situ* measurements. For the GPS-IR approach (ground-based single antenna configuration), Larson et al. demonstrated the geodetic SNR data can be used to retrieve the near-surface soil moisture (Larson et al., 2008a,b, 2010). Rodriguez-Alvarez et al. (2009) utilized a V-pol patch antenna to exclusively receive the V-pol components of both the direct and the reflected signals. The notch position resulting from the Brewster's angle is primarily determined by the permittivity of the soil medium and thus can be used to retrieve bare soil moisture. Small and Larson found that the normalized root-mean-square (RMS) of the MP_1 time series, an observable quantizing the multipath error in the pseudorange measurement, showed good agreement with *in situ* VWC data (Small et al., 2010, 2014; Larson and Small, 2014). Chew et al. (2015) and Wan et al. (2015) demonstrated that the amplitude of the geodetic SNR interference pattern was linearly correlated with *in situ* VWC data within a range of 0-1.0 kg/m^2. If VWC was greater than 1.0 kg/m^2, the SNR amplitude saturated and the linear relationship broke down. The footprint of the GPS-IR remote sensing is typically much smaller than the spatial resolution of space based remote sensing technique, and thus can be used to validate the remote sensing data. It is worth noting that one common difficulty of the microwave remote sensing techniques, both active and passive, is that the existence of the vegetation canopy affects the emissivity and scattering coefficients of the underlying soil (Jackson and Schmugge, 1991). Also the variations of soil moisture have an influence to the retrieval of vegetation biophysical parameters.

This chapter describes an experiment that investigates three observables in vegetation growth sensing using the GPS-IR technique: SNR amplitude, SNR notches, and MP_1rms. The three observables, corresponding antennas, and reference papers are listed in Table 7.1. To validate the GPS-IR metrics, *in situ* soil moisture and VWC measurements are surveyed periodically. The experiment is focused on vegetation state sensing, but it also provides the opportunity to assess the potential of measuring bare soil moisture using the H-pol SNR amplitude.

index	Observable	Antenna	Reference
1	SNR amplitude	Horizontal L1	Wan et al. (2015), Chew et al. (2015)
2	SNR notches	Vertical L1	Rodriguez-Alvarez et al. (2009)
3	MP_1rms	Horizontal L1 & L2	Small et al. (2010, 2014), Larson and Small (2014)

Table 7.1: Three observables (SNR amplitude, SNR notches, MP_1rms) were investigated in the vegetation state sensing experiment. Three antennas (H-pol L1, H-pol L2, and V-pol L1) were employed to provide the desired observables.

7.1 Experimental Setup

An experimental campaign was conducted from May to August, 2014 at an alfalfa farm in Boulder, Colorado, USA. This experiment is to evaluate the three observables listed in Table 7.1 in the measurement of vegetation biophysical parameters.

The assembled vegetation sensor is shown in Figure 7.1(a). A 100-Watt solar panel was employed to provide power to the whole system. A mobile cellular radio was used to provide remote connectivity. This vegetation sensor employed three GPS antennas: a vertically polarized L1, a horizontally polarized L1, and a horizontally polarized L2. Two low-cost MediaTek GPS L1 receivers were used to collect the SNR data from the H-pol and V-pol L1 antennas, respectively. A high-end geodetic-quality Novatel receiver was used to provide the dual-frequency observable MP_1rms. A web camera was installed to monitor the vegetation growth. A Raspberry Pi, an inexpensive embedded computer that can further cut the hardware cost from hundreds of dollars to dozens of dollars, was used to control the system and record the SNR data. The location of the vegetation sensor (40°01′52.15″N, 105°10′11.75″W) in Google Maps is shown in Figure 7.1(b).

The experiment period was from May 1st, before the alfalfa sprouted, to August 13th, after the alfalfa was harvested and moved out of field. The antennas were east-oriented, and thus the south region, which had most ground tracks, was the optimal sensing area. The V-pol L1 antenna had no preference as to azimuth. Due to the distribution of the GPS satellites, there were few complete ground tracks to the north.

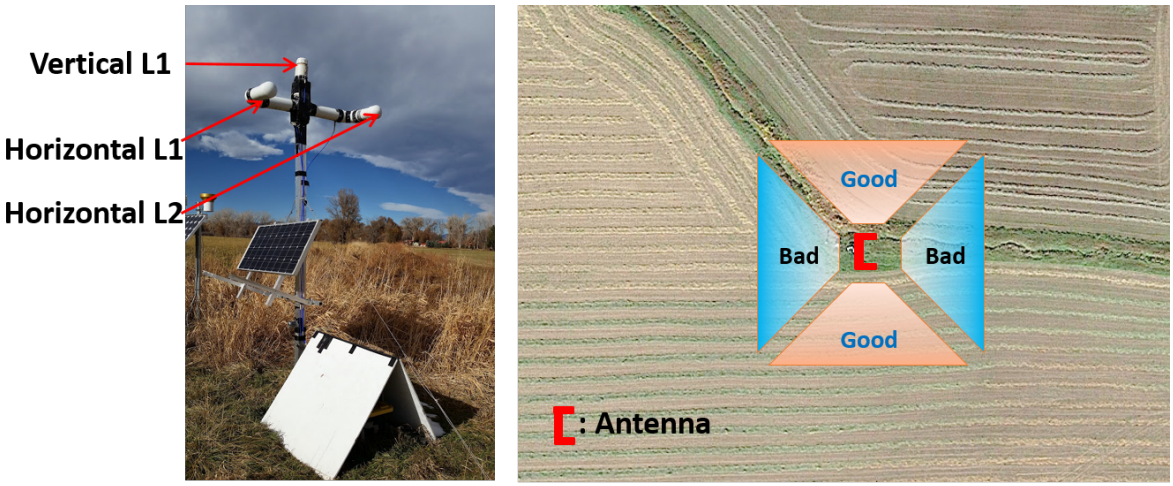

Figure 7.1: (a) Photograph of the assembled vegetation sensor. Three GPS antennas (H-pol L1 and L2, V-pol L1) are utilized. The GPS receivers, Raspberry Pi, and other devices are inside the black box under the white shield. The horizontal antennas are approximately 3 m above the ground. (b) The horizontal antennas are east-oriented, so the optimal sensing region is the south area. The V-pol L1 antenna is omnidirectional and thus has no preference as to azimuth.

In situ measurements are needed to validate the GPS metric. During the experimental period, *in situ* vegetation state data were sampled on a nearly weekly basis. In total, 11 field surveys were completed. The *in situ* vegetation measurements include vegetation height and vegetation water content. For each vegetation sampling survey, seven 30-cm by 30-cm quadrats were selected randomly in the sensing region and their locations were recorded. Their distances from the antenna ranged from 7 to 34 m. The vegetation within each quadrat was clipped, weighed immediately to get the wet weight, dried in an oven at 50 °C for 48 h, and weighed again to get the dry weight. The difference of the wet and dry weights represents the vegetation water mass, which is then

normalized by the sampled area to obtain the vegetation water content. The data from the seven sampled quadrats were averaged to get one day's *in situ* VWC measurement. Also at each quadrat, the vegetation height was measured and then averaged in the same way. Soil moisture data were sampled by Campbell Scientific 616 soil moisture probes at a rate of one sample per 30 min. The probes were distributed as follows: five probes were buried in soil at 2.5 cm, five were buried at 7.5 cm, and two were buried at 20 cm. Because the penetration depth of L-band EM wave is ∼5 cm, we only utilized the 2.5 cm probe data here, which provides an average of the top 5 cm of the soil column. The 2.5 cm depth soil moisture data within one day were averaged to get a single day's soil moisture data representative of the top 5 cm of the soil column, as in Larson et al. (2008b).

7.2 Raw Experimental Data

Three observables are evaluated in the experiment for vegetation state sensing. In this section, we examine the experimental data of each observable, concluding that the H-pol SNR amplitude A_h is the optimal observable for vegetation state sensing.

7.2.1 Observable 1: MP_1rms

Usually most high-end geodetic GPS receivers provide two ranging observables for each frequency: the code phase measurement P_i (i.e. pseudorange) and carrier phase measurement ζ_i. Here i represents the GPS L_i frequency ($i = 1, 2, 5$). The name "pseudorange" comes from the fact that several error terms are included in P_i as well as the actual geometric range:

$$P_i = \rho + c\delta_t + I/f_i^2 + T + M_i + \epsilon_i \tag{7.1}$$

where ρ is the geometric range between the GPS satellite and receiver, δt is receiver's clock error relative to the GPS time. The error term I/f_i^2 is the ionospheric delay, where $I = 40.3TEC$ and TEC (total electron content) is the number of electrons in a 1-m^2 cross section extending from the satellite to the receiver. T is tropospheric delay caused by the dry gases (mainly N_2 and O_2) and the water vapor in the atmosphere. Unlike ionospheric delay, tropospheric delay T is non-dispersive

and is the same for all GPS frequencies. M_i is the error term caused by multipath, and ϵ_i is the measurement noise term.

The L1 pseudorange multipath error M_1 is calculated by

$$M_1 = \frac{\alpha D \cdot \phi_{r,1}}{1 + \alpha D \cdot \phi_{r,1}} \tag{7.2}$$

where α is the ratio of the reflected signal amplitude to the direct signal amplitude, $D = 2H_0 \sin e$ is the excess path of the reflected signal relative to the direct signal, $\phi_{r,1}$ is the interference path and is calculated by

$$\phi_{r,1} = \frac{4\pi H_0}{\lambda_1} \sin e \tag{7.3}$$

The pseudorange multipath error M_1 results from the distorted correlation waveform because of multipath or reflected signal (Kaplan and Hegarty, 2005).

The carrier phase measurement ζ_i is formulated as:

$$\lambda_i \zeta_i = \rho + c\delta_t - I/f_i^2 + T + m_i + N_i\lambda_i + \epsilon_{\phi,i} \tag{7.4}$$

where N_i is an unknown integer number, referred to as the carrier phase ambiguity, m_i is the carrier phase multipath error, which is much smaller than the pseudorange multipath error (just several cm), $\epsilon_{\phi,i}$ is the carrier phase measurement error, usually just a few mm. It is noticeable that the ionospheric delay term for carrier phase measurement has the same magnitude as that in the pseudorange but with a negative sign.

A dual-frequency observable referred to as the MP_1 is formulated by

$$MP_1 = P_1 - \frac{f_1^2 + f_2^2}{f_2^2 - f_2^2}\zeta_1\lambda_1 + \frac{2f_2^2}{f_1^2 - f_2^2}\zeta_2\lambda_2 = M_1 + C + \epsilon_1. \tag{7.5}$$

where C is an unknown constant bias provided that the carrier phase ambiguities N_1 and N_2 do not change, i.e., no cycle slips during the observation period. Therefore, MP_1 is usually used to describe the pseudorange multipath error M_1.

When the GPS satellite is rising or setting, the interference phase $\phi_{r,1}$ varies rapidly, depending on the reflector height and the elevation angle. The excess path D also varies as the elevation

angle changes, but in a much slower rate than $\phi_{r,1}$. The ratio α can be approximated by the root-mean-square (rms) of the MP_1 time series, which is primarily determined by the vegetation growth state. One sample of the MP_1 time series (PRN 13 on May 1, 2014), together with a field photograph, are shown in Figure 7.2. The azimuth angle of PRN 13 during the observation time is ~175 degrees, locating in the optimal sensing area of the horizontal antenna. We can see that the MP_1 time series have multiple abrupt variations when the SNR is at the deep troughs, indicating that the receiver's tracking loop fails to keep tracking of the carrier phase of the incoming signal at the SNR troughs. When the signal power recovers to a particular threshold, the tracking loop re-acquires the signal but the integer cycles or carrier phase ambiguity changes, resulting in the abrupt changes in the MP_1 time series. It is worth noting that the geodetic MP_1 are not reported to have similar problems, because the geodetic GPS antenna has good mutipath suppression and thus the geodetic SNR would not degrade enough to fail the carrier tracking loop. However, for the customized dipole antennas, MP_1rms is not an applicable observable for vegetation state sensing.

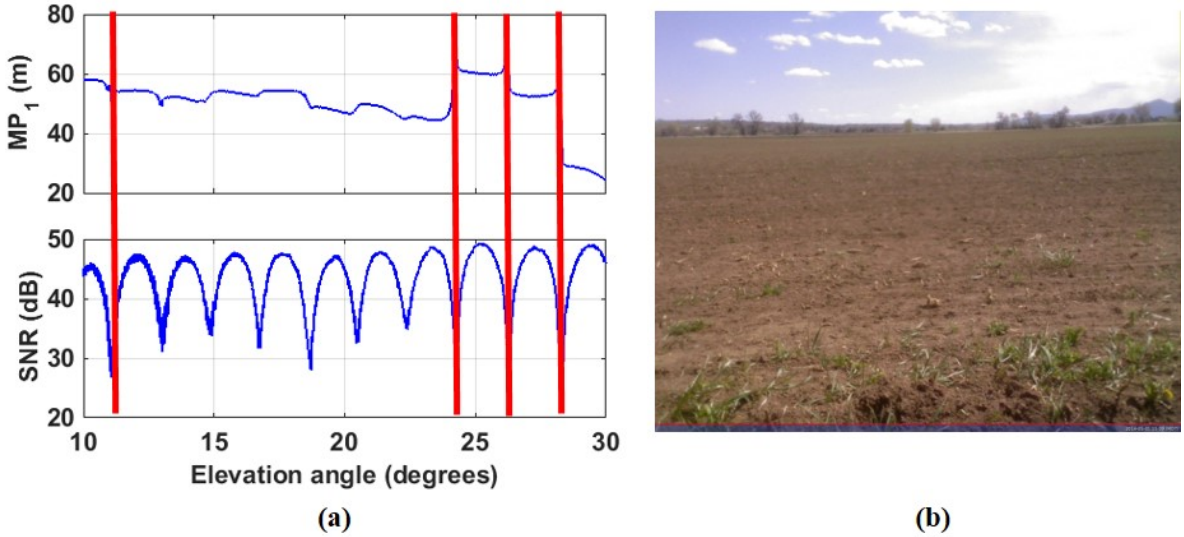

Figure 7.2: (a) MP_1 time series of PRN 13 on May 1, 2014 and the H-pol SNR. The abrupt changes in MP_1 time series are noted with red lines. (a) Photograph of the field conditions. The soil was plowed and the alfalfa had not sprouted yet.

7.2.2 Observable 2 and 3: V-pol and H-pol SNR

Different features of the V-pol and the H-pol SNR can be used to measure the vegetation biophysical parameters: the amplitude of the H-pol SNR is an indicator of the reflection power attenuation and the notches of the V-pol SNR contain the information about the vegetation height. For simplicity, the vegetation canopy can be regarded as an attenuation layer that is proportional to VWC (Ulaby and Wilson, 1985; Ulaby and Elrayes, 1987). The dual-interface model presented in Section 2.2.2 provides a more precise approach to characterise the amplitude and phase of the reflected electromagnetic wave from the vegetation canopy. Three representative H-pol and V-pol SNR time series of PRN 13 that correspond to the beginning (DoY 121), middle (DoY 171), and end (DoY 202) phases of the vegetation growth cycle are presented in Figure 7.3. In addition, photographs of the corresponding days are included to show the field conditions.

Before the alfalfa sprouted (DoY 121), both the H-pol and the V-pol SNR show a distinct interference pattern. The interference pattern of the H-pol SNR has deeper nulls than the V-pol SNR, indicating that more reflection power is absorbed by the horizontal antenna. This matches the simulation results in Chapter 2 – $|R_h|$ is greater than $|R_v|$ for bare soil case. The interference pattern of the V-pol SNR has a notch in amplitude when the elevation angle is around 22 degrees. This should be attributed to the Brewster's angle of the V-pol reflection. The V-pol interference pattern does not completely diminish at the Brewster's angle, because of the non-uniformity of the soil layer as well as the surface roughness. Using the *in situ* soil moisture data and the soil permittivity-moisture model described in Hallikainen et al. (1985), we can compute that the theoretical Brewster's angle is 24 degrees, which is close to what is observed in V-pol SNR data. There are also some mismatches between experimental data and simulated results in Chapter 2. For example, the simulated V-pol SNR at low elevation angles (below 13 degrees) shows irrelevance to vegetation growth (see Figure 2.3), while the experimental V-pol SNR data shows a uniformly decreasing trend even at low elevation angles. This discrepancy indicates the limitation of the layered model - the inhomogeneities of the vegetation layer and the inside volume scattering are

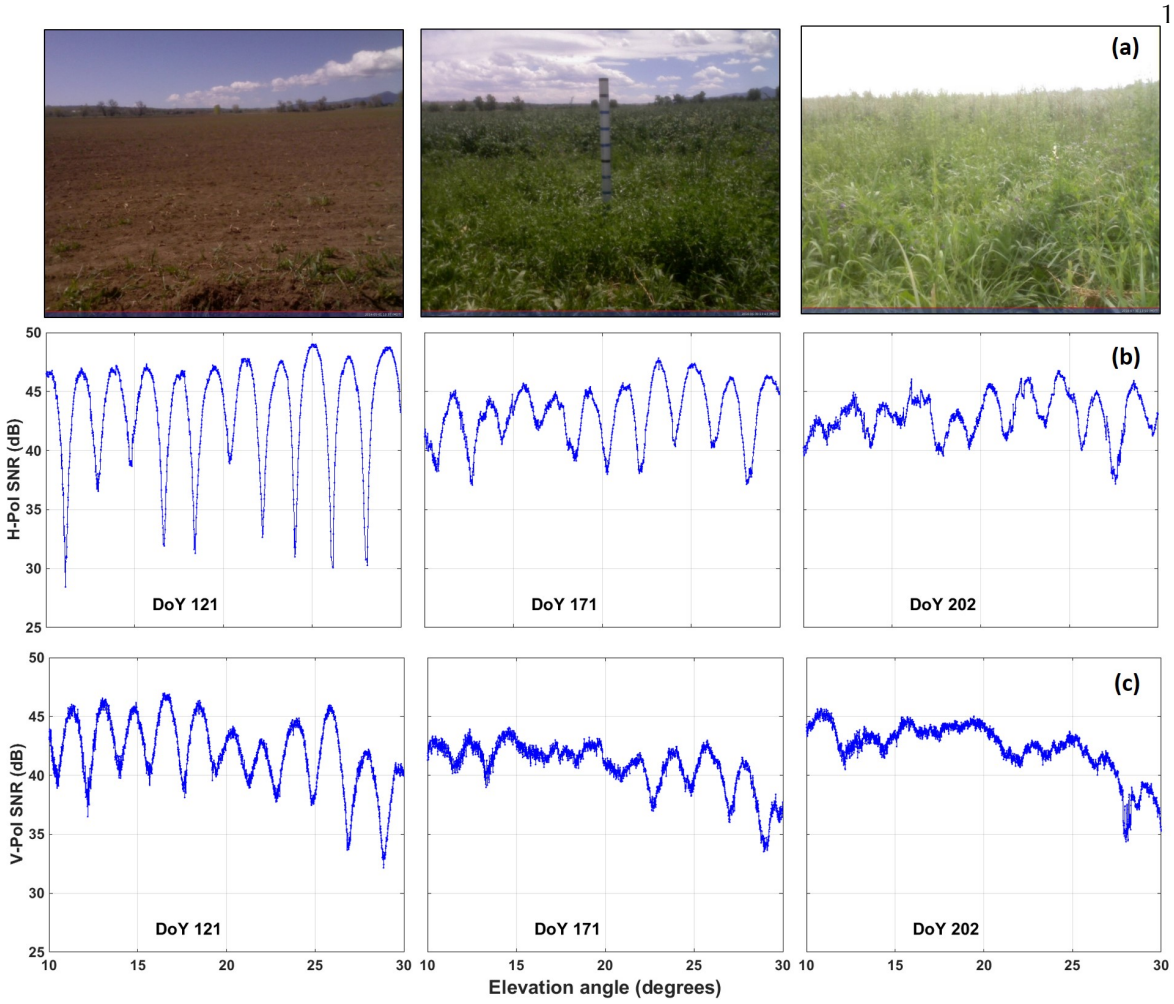

Figure 7.3: (a) Photographs of field conditions, (b) V-pol SNR, and (c) H-pol SNR of PRN 13 in Region 13 on DoY 121, 171, and 202, 2014.

not accounted for. Also for this reason, we use a relatively large cutoff elevation angle (10 degrees) because we see an obvious drop in SNR amplitude when elevation angles are below 10 degrees.

As the vegetation grows, we can see a drop in the H-pol SNR amplitude, which also matches the simulation results in Chapter 2. For the V-pol SNR, the interference patterns are blurred as the vegetation grows. It is difficult to identify any notch in the V-pol SNR data from DoY 171 and 202. In contrast, notches were observed in Rodriguez-Alvarez et al. (2009, 2011a,b) throughout the experimental cycle. The results presented here and those from Rodriguez-Alvarez et al. (2009, 2011a,b) are not expected to be the same: different antennas (patch vs. dipole) were used in the two experiments, and different types of vegetation (wheat, barley, maize vs. alfalfa) were studied.

Therefore, for this particular experimental setup, only the H-pol SNR is applicable while the other two observables have limitations in measuring vegetation biophysical parameters.

7.3 H-pol GPS Metric A_{norm} and *in situ* Measurements

The MediaTek receiver generates a customized NMEA message that includes the desired SNR information. The customized NMEA message can provide SNR resolved to 0.1 dB. Since a portion of the COTS GPS receivers only provide quantized SNR resolved to 1 dB, we manually quantized the received SNR to 1 dB and found that the error of A_{norm} introduced by the quantization effect is minor (less than 2%). The elevation angle mask used in the data processing is from 10 to 30 degrees, resulting in the ground tracks extending from 5 to 20 m. There are approximately 70 GPS arcs, both rising and setting, satisfying the elevation angle mask each day. The ground tracks are not evenly distributed in azimuth – most are in the southerly direction. The full azimuth direction is evenly divided into 16 sectors and the ground tracks in the two southern-most sectors R12 and R13 are used to compute one day's SNR amplitude metric (see Figure 7.4). For each ground track's SNR data, LSP is used to obtain the oscillation frequency of the interference pattern. As is shown in Figure 7.3, the SNR data does not exhibit a rising trend as the geodetic SNR and thereby no detrending processing is required. Then the amplitude is estimated using the least-quare fit method, with the estimated oscillation frequency as the input. A quality check procedure, using the ratio of post-fit error to the amplitude as a goodness-of-fit indicator, is carried out to exclude the erroneous tracks. Finally, the estimated amplitudes that pass the quality check are averaged to be a single value and then normalized by bare soil SNR amplitude, serving as the derived GPS metric A_{norm} for that particular day.

The time series of vegetation height (*in situ* and camera), *in situ* VWC, normalized SNR amplitude A_{norm}, effective reflector height H_{eff}, and soil moisture from the observation period are shown in Figure 7.5. The vegetation was cut on DoY 217 (labeled by the yellow bar), then removed from the field on DoY 225 (labeled by the green bar). The raw SNR amplitude time series are normalized by the average of amplitude measurements from DoY 120 to 123. During these four

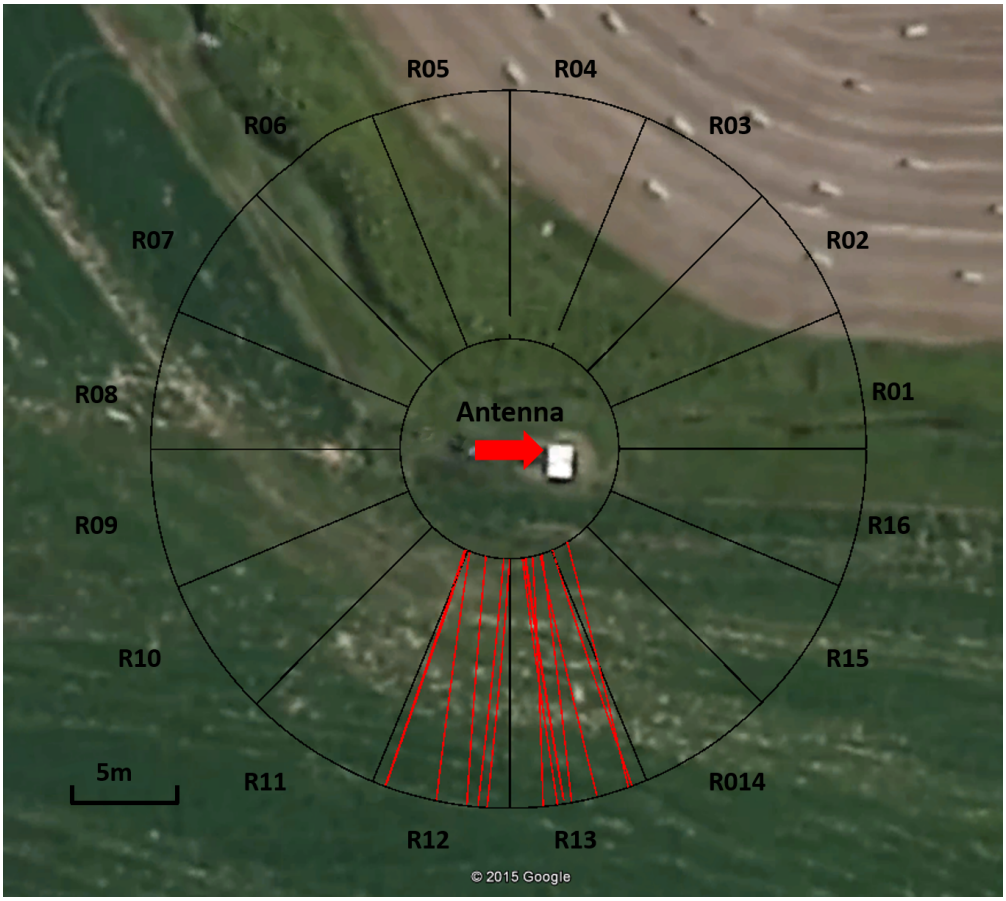

Figure 7.4: The whole sensing region is evenly divided into 16 sectors. The two sectors in the south direction (R12 and R13) are the optimal sensing area because the antenna is east oriented. In the two sectors, there are about 12 ground tracks usable.

days, the vegetation had not yet sprouted. In addition, there were no precipitation events so the soil moisture was relatively constant. In the following interval, precipitation would increase the soil moisture and thus the reflection power. As a result, the normalized SNR amplitude is greater than 1 on some days.

The normalized SNR amplitude A_{norm} clearly decreases as the vegetation grows (see Figure 7.5, panels 1, 2, and 3), from the value of 1.0 at the start of the observation period to close to zero prior to the alfalfa cutting. During this interval, vegetation height increases from 0 to 90 cm and VWC increases from 0 to 6 kg/m^2. The high amplitude values between DoY 130 and 150 show the effects of increasing soil moisture, prior to the sprouting of the alfalfa. Once the alfalfa

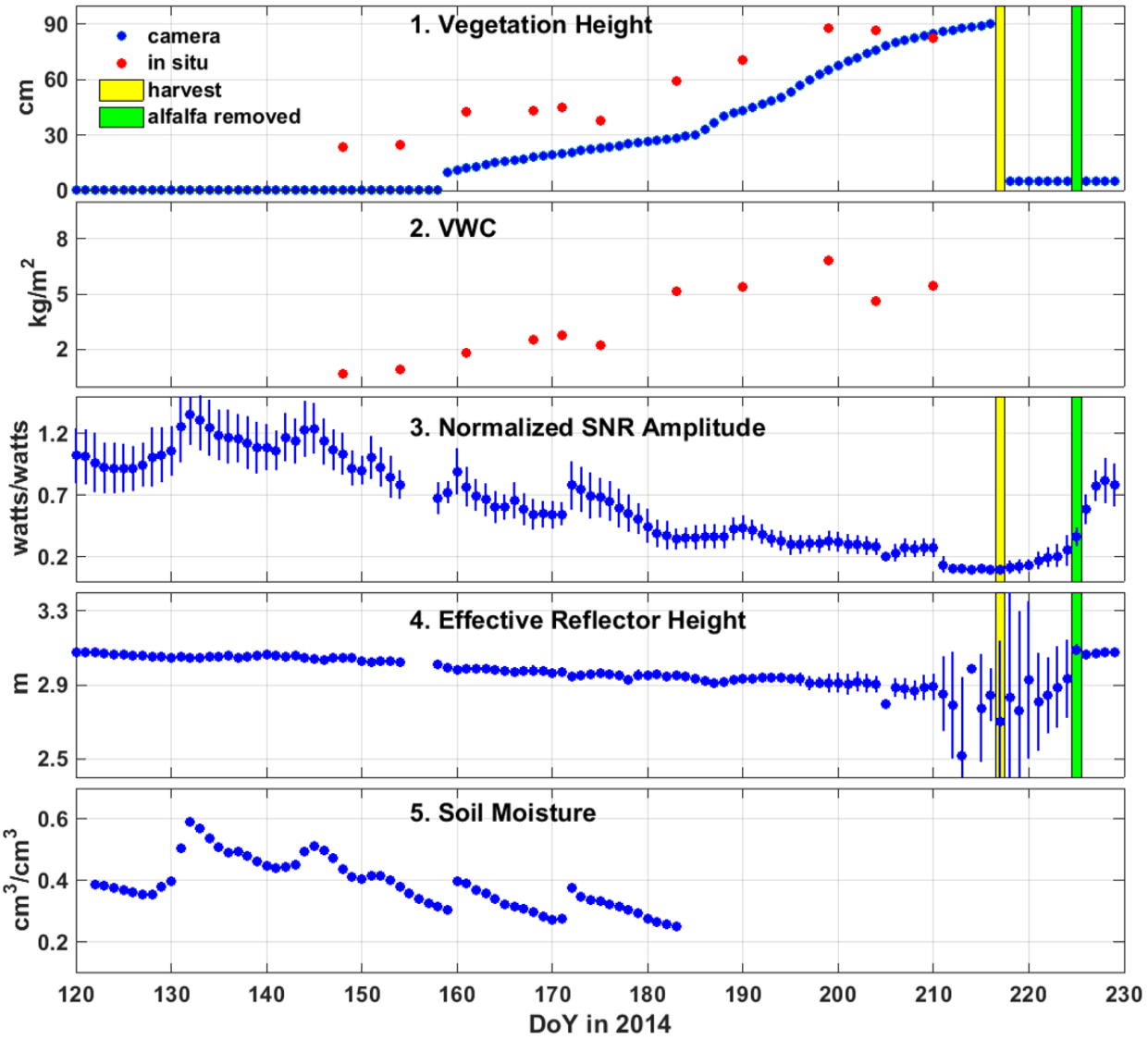

Figure 7.5: Time series of (panel 1) vegetation height, (panel 2) VWC, (panel 3) normalized SNR amplitude A_{norm}, (panel 4) effective reflector height H_{eff}, and (panel 5) soil moisture from DoY 120 to 230. The error bars of panel 3 and 4 are based on the standard deviation of the measurements. Please note that the standard deviation of H_{eff} is only a few cm at the beginning of the vegetation growth (thus the error bar is invisible), and then increases as vegetation grows. The vegetation is cut on DoY 217, as is noted by the yellow bar. The cut vegetation was left in the field to dry, and then removed on DoY 225 (labeled by the green bar). The soil moisture data is not available after DoY 183 because of hardware issues.

sprouts, there is a nearly monotonic decrease in A_{norm} as vegetation height and VWC increase. This decrease occurs over a range of VWC of 0-6 kg/m^2. Importantly, A_{norm} does not increase after the vegetation is cut on DoY 217, which indicates that A_{norm} is not sensitive to vegetation

height or vegetation density. In contrast, A_{norm} does increase dramatically (almost to 1.0) once the cut vegetation is removed from the field on DoY 225. This shows that A_{norm} is affected directly by the variations in VWC. The apparent relationship between A_{norm} and vegetation height is the outcome of a linear correlation between vegetation height and VWC during the growth period. Panels 3 and 5 show that the general decline in A_{norm} is temporarily affected by abrupt increases in soil moisture due to precipitation or irrigation. These sharp increases in soil moisture increase the permittivity of soil and the H-pol reflection coefficient, as shown in Figure 2.3.

It is demonstrated that the effective reflector height H_{eff} derived from geodetic SNR is not a reliable indicator of vegetation change (Chew et al., 2015). From panel 4 of Figure 7.5, H_{eff} linearly decreases from ∼3.1 m (bare soil) at the beginning to ∼2.8 m prior to harvest (∼1 m vegetation). The decrease of H_{eff} is much smaller than the increase of vegetation height (0.3 m vs. 1 m), indicating that the soil surface is still the primary reflector even with high vegetation. Moreover, H_{eff} becomes unreliable when the vegetation height reaches a particular threshold prior to the harvest: the average H_{eff} behaves randomly and the standard deviation greatly increases. The reason for the randomized H_{eff} and the increased errors is likely the high-vegetation LSP has two peaks and the maximum peak alternates, as demonstrated in Chew et al. (2015).

7.4 Correlation Analysis between GPS Metric and *in situ* Measurements

As mentioned previously, the layered model (vegetation + soil) does not account for the inhomogeneities and the volume scattering of the vegetation canopy, so it is desired to assure that the model is valid in describing the response of SNR amplitude to vegetation growth. In Figure 7.6, we reconstruct SNR using *in situ* soil moisture and vegetation measurements. Although the simulated SNR does not match the measured SNR in every detail, it does predict the amplitude attenuation because of vegetation growth. Therefore, the layered model is valid in describing the SNR amplitude attenuation because of vegetation growth (i.e. VWC increases).

A regression analysis is conducted between the GPS metric A_{norm} and vegetation biophysical parameters (VWC and vegetation height). Figure 7.7 shows that a clear negative correlation exists

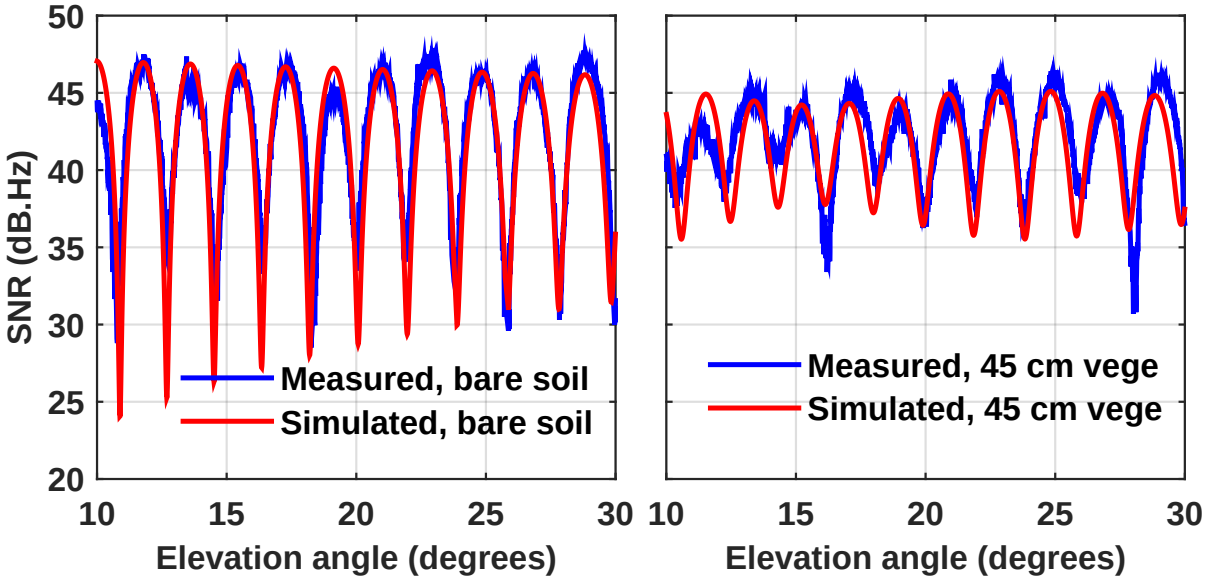

Figure 7.6: Simulated and measured SNR time series corresponding to different vegetation heights. The permittivities of vegetation canopy and soil are derived from *in situ* VWC and soil moisture measurements. The simulated SNR match well with measured SNR in terms of amplitude attenuation.

between A_{norm} and the *in situ* measurements of VWC. The uncertainties shown are based on the standard deviation of the A_{norm} observations and *in situ* measurements. The R^2 is 0.86, indicating a good agreement between the two variables. The maximum *in situ* VWC exceeds 6 kg/m^2, which is much greater than the maximum VWC detectable using geodetic GPS data (1.0 kg/m^2). Figure 7.8 shows the correlation between A_{norm} and the *in situ* vegetation height is similarly high (R^2 = 0.86). Generally we can say the normalized SNR amplitude A_{norm} shows a good linear relationship with the *in situ* measurements of the vegetation biophysical parameters (VWC and vegetation height).

The simulation results in Chew et al. (2015) show that A_{norm} derived from geodetic SNR is linearly decreasing as VWC increases provided that VWC is below 1.0 kg/m^2, and then saturate. Because the GPS antenna and vegetation type in this experiment are totally different from the configuration in Chew et al. (2015), we re-simulate the responses of A_{norm} with vegetation growth, as shown in Figure 7.9. The magnitude of the simulated decreasing slope is close to but smaller than

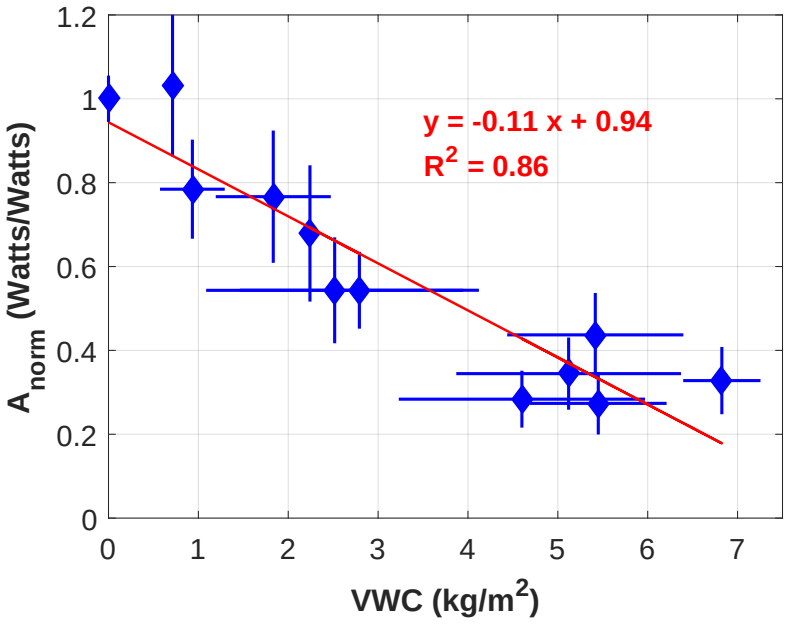

Figure 7.7: The correlation between A_{norm} and VWC. Both the A_{norm} and *in situ* VWC uncertainties are based on the observation standard deviation. The first dot corresponds to the bare soil case. The regression yields $A_{norm} = -0.11 * VWC + 0.94$ with a R^2=0.86. The 95% confidence level of slope coefficient is -0.11 ± 0.03.

that fitted by the actual data. This discrepancy should also be attributed to the unincorporated inhomogeneities and volume scattering of the vegetation canopy, which would bring in extra signal power loss.

Figure 7.5 (3) and (5) clearly indicates that A_{norm} is affected by the change of soil moisture as well as the vegetation growth. Basically the soil moisture and vegetation are affecting A_{norm} in opposite trends: increasing soil moisture can enlarge the complex permittivity of soil and thus makes reflection power stronger; vegetation growth (increasing VWC) attenuates the reflection power more by either assimilating or scattering the reflected radio waves. Here we make use of the multiple precipitation events and the *in situ* surface soil moisture data to evaluate the soil moisture effect on A_{norm}. First, we use the soil permittivity-moisture model (Wang and Schmugge, 1980; Hallikainen et al., 1985) to simulate the responses of A_{norm} and compare with the measured A_{norm}. If the effectiveness of the model is validated, then it can be used to assess the effect of soil moisture

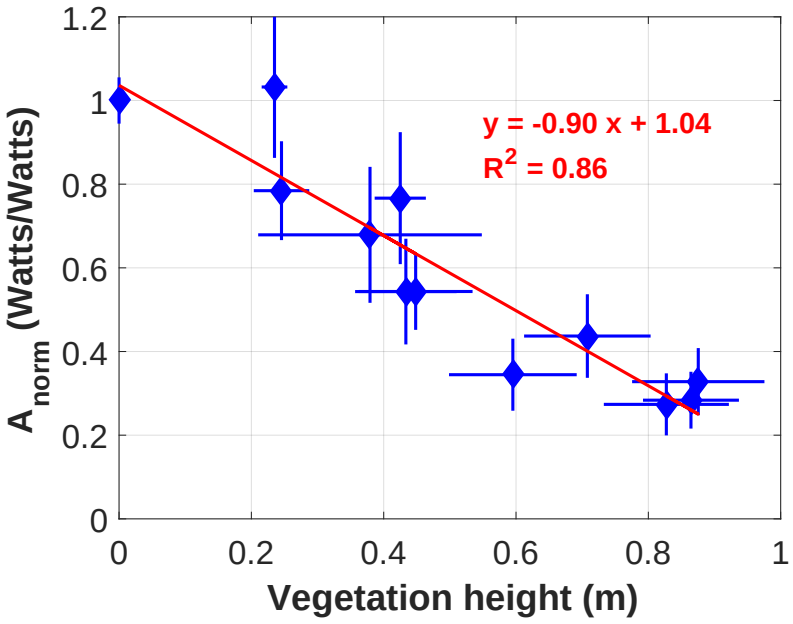

Figure 7.8: The correlation between A_{norm} and vegetation height (VH). Both the A_{norm} and *in situ* vegetation height uncertainties are based on the observation standard deviation. The first dot corresponds to the bare soil case. The regression yields $A_{norm} = -0.90 * VH + 1.04$ with a R^2=0.86. The 95% confidence level of slope coefficient is -0.9 ± 0.32.

variations on A_{norm}.

Before the alfalfa sprouts, the soil roughness is quite stable and the change of A_{norm} should be attributed to the change of the soil moisture. With the *in situ* soil moisture data, we can simulate the change of A_{norm}. The relationship of the simulated and actual A_{norm} changes (ΔA_{norm}) is shown in Figure 7.10 and the regression has a slope of 1.00 and R^2 of 0.66, which validates the effectiveness of the permittivity model for bare soil. Based on this calculation, the change of A_{norm} introduced by precipitation or irrigation is estimated to be no larger than 24% during the experiment period, using the maximum and minimum available soil moisture value as the inputs.

The *in situ* soil moisture data also provides the opportunity to investigate near-surface soil retrieval using A_{norm}, which is an indicator of the reflection power. In this experiment, the surface roughness is relatively stable and thus effect of surface roughness variations is not evaluated. As mentioned previously, the vegetation canopy can greatly change the reflection power and it is

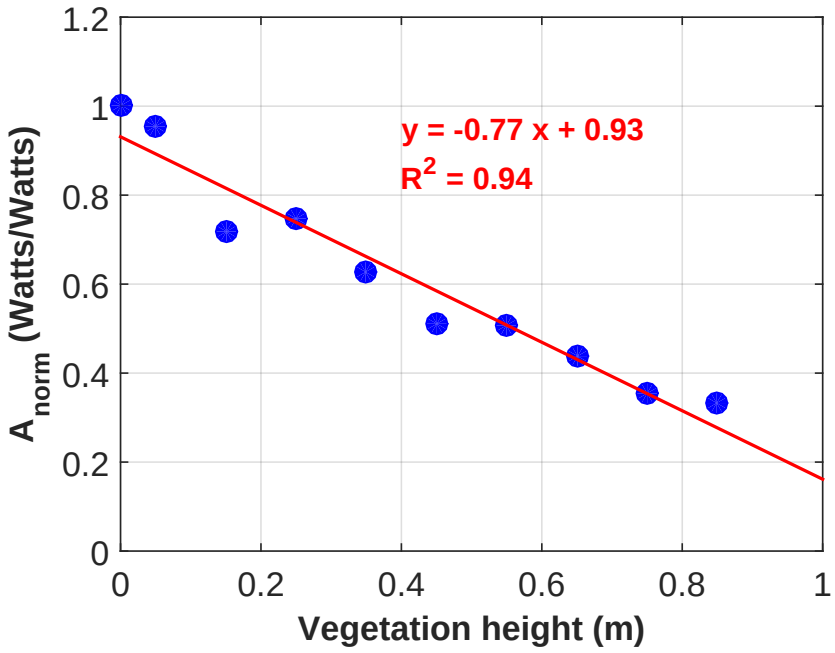

Figure 7.9: Simulated A_{norm} vs. vegetation height. The vegetation permittivity used in the simulation is 1.06+0.015j, which is derived from *in situ* vegetation measurements.

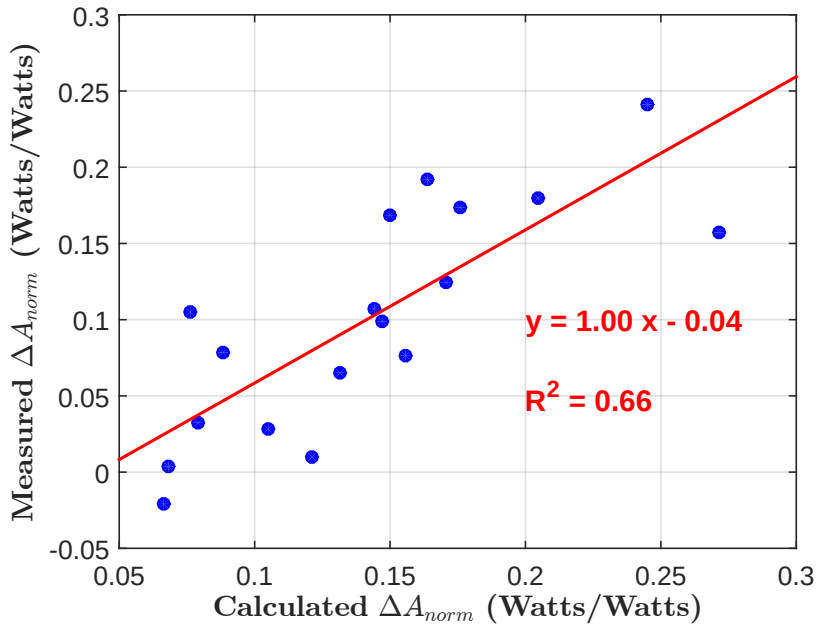

Figure 7.10: Measured A_{norm} change vs. calculated A_{norm} change from *in situ* soil moisture data before alfalfa sprouts. With soil moisture, soil permittivity can be calculated using the model in Wang and Schmugge (1980) and compute the A_{norm} change using the model in Chew et al. (2015).

difficult to isolate the two factors (soil moisture and vegetation) without ancillary data. Therefore, only the near-surface soil moisture retrievals for bare soil conditions are evaluated here and the isolation of the vegetation effect is beyond the scope of this dissertation. The relationship between the near-surface soil moisture and A_{norm} is shown in Figure 7.11. The R^2 is 0.84, also indicating A_{norm} has a strong linear relationship with near-surface soil moisture. The distribution of the retrieved soil moisture error is shown in Figure 7.12. Overall, the performance of utilizing H-pol A_{norm} for bare soil moisture retrieval is comparable with the results reported in Larson et al. (2010), Rodriguez-Alvarez et al. (2009), and Alonso-Arroyo et al. (2014b).

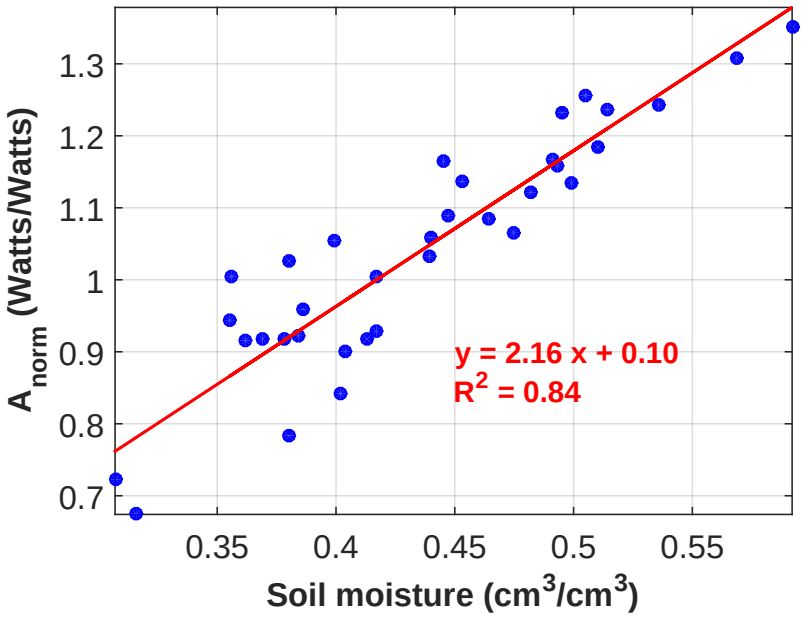

Figure 7.11: The correlation between A_{norm} and near-surface soil moisture. The regression yields $A_{norm} = 2.16{*}SM{+}0.10$ with a R^2=0.84. The 95% confidence level of slope coefficient is 2.16±0.43.

7.5 Summary

In this chapter, we present an experiment carried out at an alfalfa farm in Boulder, Colorado, USA from May to August, 2015 to evaluate three GPS-IR observables in vegetation state sensing. The MP_1rms from the horizontally-polarized antennas is not applicable because of the frequent cycle slips resulted from better reflection power reception of the H-pol dipole antenna. The SNR

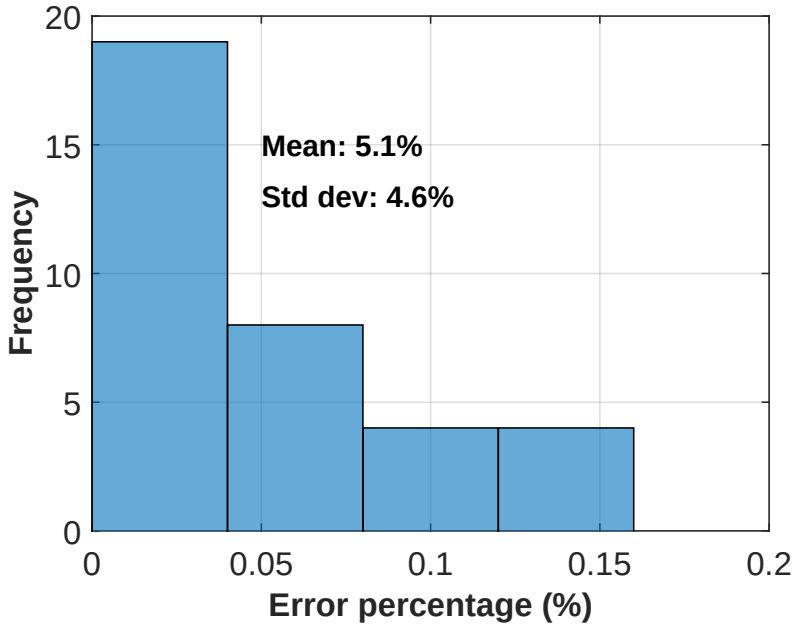

Figure 7.12: Distribution of retrieved soil moisture error $(SM_{retrieved} - SM_{in\ situ})/SM_{in\ situ}$.

notches from V-pol SNR are suitable for bare soil moisture retrieval, but are difficult to identify with existence of vegetation canopy. The normalized H-pol SNR amplitude shows a negative, linear relationship with the vegetation water content over a range of 0-6 kg/m^2. This measurement range is much greater than that detectable using standard geodetic systems or a V-pol dipole antenna. The extended measurement range is due to the increased reception capability of the dipole antenna used in the experiment. The effect of the soil moisture change is also observed and evaluated. The variations of soil moisture produce relatively smaller changes in normalized SNR amplitude. The normalized H-pol SNR amplitude also shows a linear relationship with near-surface soil moisture for bare soil conditions, indicating its potential as a soil moisture sensor.

Chapter 8

Conclusions

The studies presented in this dissertation contribute to the field of GNSS Reflectometry, with emphasis in the instrument optimization for applications of GPS Interferometric Reflectometry. GPS-IR was originally developed for the application of measuring near-surface soil moisture using data from the geodetic GPS networks. Later it was extended to other applications, including the measurements of snow depth/SWE, coastal sea/water level, and vegetation biophysical parameters. This dissertation first analyzes the signal characteristics of four available polarizations of the GPS signals, and then discusses how these characteristics are related to and can be used for several typical remote sensing applications of GPS-IR. Two types of antennas (a half-wavelength dipole antenna and a patch antenna) are proposed to utilize the linear polarizations, and their design procedures are detailed. A series of field experiments are conducted to evaluate the performance of the proposed antennas in measuring snow depth, vegetation biophysical parameters, and near-surface soil moisture. The main contributions of this dissertation are summarized below.

First, the reflection characteristics (i.e. the magnitude and phase of the Fresnel reflection coefficients) of four polarizations (horizontal, vertical, RHC, and LHC) of the GPS signals are simulated and discussed. Depending on the environmental conditions of the applications, two reflection models (single-interface model and dual-interface model) are utilized to simulate the reflection properties. For the first type of applications, such as water level and soil moisture measurements, the single-interface model is applicable because the large permittivity value of the bottom medium allows for a single reflector. For the second type of applications, such as measuring

vegetation biophysical parameters, the dual-interface model is used to account for the reflections from the underlying soil, as the vegetation canopy is not dense enough to overshadow the effect of the soil. The snow medium is more complex, where the snow is usually regarded as a single reflector. However, the results from the Marshall Field experiment described in this dissertation show that the effect of soil cannot be ignored, at least for shallow snow. For deep snow, the effect of soil diminishes and it is safe to use the single-interface model to simulate the reflection properties.

It is concluded that the horizontal polarization, which is suitable for the measurements of water level, snow depth, vegetation biophysical parameters, and near-surface soil moisture, has the most extensive applicability. The vertical polarization possesses an important characteristic that, at the Brewster's angle, the incident electromagnetic wave completely penetrates the bottom medium and is not reflected at all. This characteristic makes vertical polarization suitable for the measurement of near-surface soil moisture, which primarily determines the complex permittivity of the soil medium and thus the position of the Brewster's angle. However, the simulation results reveal the potential difficulty of detecting notches when using vertical polarization for the measurement of vegetation biophysical parameters (e.g. vegetation height). The reflection coefficient of RHCP is almost not affected by soil moisture and therefore, RHCP is not suitable for the measurement of soil moisture. The magnitude of the reflection coefficient of the LHCP has a rising trend, which is different from the other three polarizations. This characteristic makes LHCP unsuitable for the GPS-IR technique because in general, only SNR data at low elevation angles is used to obtain a large footprint.

Second, two antenna prototypes, the half-wavelength dipole antenna and the patch antenna, are designed and fabricated to utilize the linear polarizations (the horizontal polarization and the vertical polarization) specifically for the GPS-IR applications. The dipole antenna can be configured to work with either horizontal polarization or vertical polarization. One important feature of the dipole antenna in a horizontally-polarized configuration is that it has a constant gain for different elevation angles, which is desired for the calculation of the received reflection power as it excludes the effect of antenna's gain on SNR. The patch antenna also provides the flexibility of polarization

selection by carefully placing the feed point. A horizontally-polarized patch antenna is proposed to provide a new antenna option for GPS-IR applications. The design and optimization procedures using the HFSS simulation software are detailed for each of the antennas. These two antennas are used in different scenarios: the dipole antenna is more suitable for an open area and the patch antenna is more applicable when a particular direction is preferred.

Four field experiments were conducted to assess the feasibility of the design criteria and the proposed antennas. Three experiments are focused on snow depth measurement and the other is focused on the measurement of vegetation biophysical parameters and near-surface soil moisture. The first snow experiment was conducted on the Table Mountain plateau, CO in February 2012, aimed to evaluate the performance of the proposed dipole antenna in the measurements of bare ground reflector height and snow depth. The experiment also provides the opportunity to assess the data processing capability of a MATLAB-based L2C SDR. The SDR implements an open-loop tracking algorithm that allows for more robust and accurate SNR estimation than a typical COTS receiver, which uses a close-loop tracking structure. The SNR estimation by the closed-loop tracking algorithms implemented in the COTS GPS receivers has a higher probability of loss of lock when the reflected signal deteriorates the direct signal to a particular threshold. The SNR data collected with the dipole antenna is promising: the bare ground SNR shows a more distinct interference pattern in a wider elevation angle range and results in a more precise estimation of the reflector height. Obvious frequency changes are observed after the snowfall that occurred during the experiment. The results validate the signal characteristics and the utility of the horizontal polarization concluded in Chapter 2.

The second snow experiment was conducted in the Marshall Field of UCAR in CO during the 2013-2014 water year. Instead of using the L2C SDR, a low-cost COTS L1 receiver was employed to provide the SNR of L1 C/A signal. The utilization of the L1 C/A signal increases the number of usable GPS satellites, and thus more measurements can be obtained. When compared to the L2C SNR data from the customized SDR, no obvious deterioration is observed in the SNR data from the COTS L1 receiver. The experiment results suggest the possibility of building high-

performance GPS-IR instruments using inexpensive COTS instruments. Other data sets of snow depth measurements (visual and sonic) are utilized to compare with and validate the GPS-derived snow depth data. In general, the GPS snow measurements match well with the *in situ* measurements. Occasional measurement anomalies are observed that either overestimate or underestimate the actual snow depth. The dual-interface model is employed to account for the measurement anomalies, which indicates that the effect of underlying soil cannot be ignored for shallow snow. The distribution of the snow measurements matches well with the simulation results. With the dual-interface model, an error curve of the snow depth estimation is obtained, indicating that the layering effect is detectable only for shallow snow and diminishes for deep snow.

The alpine areas store the most snowpack, and thus it is desirable to investigate the feasibility of the GPS-IR technique in such areas. The third snow experiment was carried out at the mountaintop Storm Peak Laboratory, CO from February to July, 2015. Rather than using the dipole antenna, the horizontally-polarized patch antenna was utilized to suppress the undesired reflections from the SPL structure. The environment is challenging in the sense that the terrain is not horizontal, but has a relatively large tilt angle. In addition, the tilt angle of the snow surface is variant and can be changed by strong winds. We add the tilt angle of the reflecting surface into the GPS-IR forward model and propose an algorithm to estimate the tilt angle from the phase pattern of the observed SNR. The estimated tilt angle is used to calculate the vertical antenna height. Because of the periodicity of the SNR interference pattern, more than one tilt angle can result in the observed SNR interference pattern, and thus adds the difficulty of estimating the tilt angle. In general, the GPS snow depth measurements and the *in situ* measurements match up well with a RMSE of 14 cm. The experiment results show the potential and effectiveness of the proposed algorithm in complex multipath environment.

The last experiment was conducted at an alfalfa farm in Boulder, CO from May to August, 2014, with the goal to evaluate the performance of the proposed dipole antenna as applied to the measurements of vegetation biophysical parameters and near-surface soil moisture. Three GPS metrics (H-pol SNR amplitude, V-pol SNR notches, and MP_1rms) are assessed as applied to VWC

retrieval. The V-pol SNR notches are readily apparent during bare ground conditions, but diminish with growing vegetation. The MP_1 time series encounter frequent cycle slips as a result of the stronger receptivity of the reflected signals, and thus are not applicable for this particular setup. The H-pol SNR amplitude time series show a linearly relationship with *in situ* measurements of vegetation water content over a range of 0-6 kg/m^2, which is much greater than the range from the geodetic data (0-1 kg/m^2). It is concluded that the H-pol SNR is suitable for vegetation sensing in most environments, including agricultural settings. The H-pol SNR amplitude also shows a positive linear relationship with the near-surface soil moistures, indicating its potential as a soil moisture sensor.

In conclusion, the studies within this dissertation investigate key aspects related to instrument optimization of the GPS-IR technique, including signal characteristics and antenna design. A series of experiments have been conducted to verify the design and explore the performance improvements in corresponding applications. Experimental results verify the superior design of the proposed instruments.

Bibliography

A. Alonso-Arroyo, A. Camps, A. Aguasca, G. Forte, A. Monerris, C. Rudiger, J. P. Walker, H. Park, D. Pascual, and R. Onrubia. Improving the Accuracy of Soil Moisture Retrievals Using the Phase Difference of the Dual-Polarization GNSS-R Interference Patterns. IEEE Geoscience and Remote Sensing Letters, 11:2090–2094, 2014a.

A. Alonso-Arroyo, A. Camps, A. Aguasca, G. F. Forte, A. Monerris, C. Rudiger, J. P. Walker, H. Park, D. Pascual, and R. Onrubia. Dual-Polarization GNSS-R Interference Pattern Technique for Soil Moisture Mapping. IEEE Journal of Selected Topics in Applied Earth Observations and Remote Sensing, 7:1533–1544, 2014b.

A. Alonso-Arroyo, A. Camps, H. Park, D. Pascual, R. Onrubia, and F. Martin. Retrieval of Significant Wave Height and Mean Sea Surface Level Using the GNSS-R Interference Pattern Technique: Results From a Three-Month Field Campaign. IEEE Transactions on Geoscience and Remote Sensing, 53:3198–3209, 2015.

R. L. Armstrong and E. Brun. Snow and Climate: Physical Processes, Surface Energy Exchange and Modeling. Cambridge University Press, 2008.

R. Atlas, N. Wolfson, and J. Terry. The Effect of Sst and Soil-Moisture Anomalies on Gla Model Simulations of the 1988 United-States Summer Drought. Journal of Climate, 6:2034–2048, 1993.

C. A. Balanis. Antenna Theory: Analysis and Design. John Wiley & Sons, 2005.

C. A. Balanis. Advanced Engineering Electromagnetics. Wiley Online Library, 2012.

T. P. Barnett, J. C. Adam, and D. P. Lettenmaier. Potential impacts of a warming climate on water availability in snow-dominated regions. Nature, 438:303–309, 2005.

P. Beckmann and A. Spizzichino. The scattering of electromagnetic waves from rough surfaces. Artech House Inc., 1987.

K. Boniface, J. J. Braun, J. L. McCreight, and F. G. Nievinski. Comparison of Snow Data Assimilation System with GPS reflectometry snow depth in the Western United States. Hydrological Processes, 29:2425–2437, 2015.

M. Born and E. Wolf. Principles of optics: electromagnetic theory of propagation, interference and diffraction of light. Cambridge university press, 1999.

K. Borre, D. M Akos, N. Bertelsen, P. Rinder, and S. H. Jensen. A software-defined GPS and Galileo receiver: a single-frequency approach. Springer Science & Business Media, 2007.

T. W. Brakke, E. T. Kanemasu, J. L. Steiner, F. T. Ulaby, and E. Wilson. Microwave Radar Response to Canopy Moisture, Leaf-Area Index, and Dry-Weight of Wheat, Corn, and Sorghum. Remote Sensing of Environment, 11:207–220, 1981.

M. E. Brown, S. Moran, V. Escobar, D. Entekhabi, P. O'Neill, and E. Njoku. The Soil Moisture Active Passive (SMAP) Applications Activity. In International Geoscience and Remote Sensing Symposium (IGARSS), IEEE, pages 2306–2309, 2011.

E. J. Burke, R. C. Harlow, and T. Ferre. Measuring the dielectric permittivity of a plant canopy and its response to changes in plant water status: An application of Impulse Time Domain Transmission. Plant and Soil, 268:123–133, 2005.

E. Cardellach, F. Fabra, O. Nogues-Correig, S. Oliveras, S. Ribo, and A. Rius. GNSS-R ground-based and airborne campaigns for ocean, land, ice, and snow techniques: Application to the GOLD-RTR data sets. Radio Science, 46, 2011.

E. Cardellach, F. Fabra, A. Rius, S. Pettinato, and S. D'Addio. Characterization of dry-snow sub-structure using GNSS reflected signals. Remote Sensing of Environment, 124:122–134, 2012.

Q. Chen, D. Won, and D. M. Akos. Snow depth sensing using the GPS L2C signal with a dipole antenna. EURASIP Journal on Advances in Signal Processing, 2014:1–10, 2014.

Q. Chen, D. Won, and D. M. Akos. Snow depth estimation accuracy using a dual-interface GPS-IR model with experimental results. GPS Solutions, pages 1–13, 2016.

C. C. Chew, E. E. Small, K. M. Larson, and V. U. Zavorotny. Effects of Near-Surface Soil Moisture on GPS SNR Data: Development of a Retrieval Algorithm for Soil Moisture. IEEE Transactions on Geoscience and Remote Sensing, 52:537–543, 2014.

C. C. Chew, E. E. Small, K. M. Larson, and V. U. Zavorotny. Vegetation Sensing Using GPS-Interferometric Reflectometry: Theoretical Effects of Canopy Parameters on Signal-to-Noise Ratio Data. IEEE Transactions on Geoscience and Remote Sensing, 53:2755–2764, 2015.

R. D. De Roo, Y. Du, F. T. Ulaby, and M. C. Dobson. A semi-empirical backscattering model at L-band and C-band for a soybean canopy with soil moisture inversion. IEEE Transactions on Geoscience and Remote Sensing, 39:864–872, 2001.

M. C. Dobson, F. T. Ulaby, M. T. Hallikainen, and M. A. Elrayes. Microwave Dielectric Behavior of Wet Soil-part II: Dielectric Mixing Models. IEEE Transactions on Geoscience and Remote Sensing, 23:35–46, 1985.

EarthScope PBO. PBO H2O Data Portal. website, 2016. URL `http://xenon.colorado.edu/portal/`. checked: 04/11/2016.

A. Egido, M. Caparrini, G. Ruffini, S. Paloscia, E. Santi, L. Guerriero, N. Pierdicca, and N. Floury. Global Navigation Satellite Systems Reflectometry as a Remote Sensing Tool for Agriculture. Remote Sensing, 4:2356–2372, 2012.

A. Egido, S. Paloscia, E. Motte, L. Guerriero, N. Pierdicca, M. Caparrini, E. Santi, G. Fontanelli, and N. Floury. Airborne GNSS-R Polarimetric Measurements for Soil Moisture and Above-Ground Biomass Estimation. IEEE Journal of Selected Topics in Applied Earth Observations and Remote Sensing, 7:1522–1532, 2014.

M. A. Elrayes and F. T. Ulaby. Microwave Dielectric Spectrum of Vegetation-part I: Experimental-Observations. IEEE Transactions on Geoscience and Remote Sensing, 25:541–549, 1987.

D. Entekhabi, E. Njoku, P. O'Neill, M. Spencer, T. Jackson, J. Entin, E. Im, and K. Kellogg. The soil moisture active/passive mission (SMAP). In International Geoscience and Remote Sensing Symposium (IGARSS), IEEE, page 1, 2008.

I. M. Fuks and A. G. Voronovich. Wave diffraction by rough interfaces in an arbitrary plane-layered medium. Waves in Random Media, 10:253–272, 2000.

J. L. Garrison and S. J. Katzberg. Detection of ocean reflected GPS signals: theory and experiment. In Southeastcon '97. Engineering New Century., Proceedings. IEEE, pages 290–294, 1997.

J. L. Garrison, S. J. Katzberg, and M. I. Hill. Effect of sea roughness on bistatically scattered range coded signals from the Global Positioning System. Geophysical Research Letters, 25:2257–2260, 1998.

J. L. Garrison, A. Komjathy, V. U. Zavorotny, and S. J. Katzberg. Wind speed measurement using forward scattered GPS signals. IEEE Transactions on Geoscience and Remote Sensing, 40:50–65, 2002.

O. Germain, G. Ruffini, F. Soulat, M. Caparrini, B. Chapron, and P. Silvestrin. The Eddy Experiment: GNSS-R speculometry for directional sea-roughness retrieval from low altitude aircraft. Geophysical Research Letters, 31(21), 2004.

S. Gleason, S. Hodgart, Y. P. Sun, C. Gommenginger, S. Mackin, M. Adjrad, and M. Unwin. Detection and processing of bistatically reflected GPS signals from low earth orbit for the purpose of ocean remote sensing. IEEE Transactions on Geoscience and Remote Sensing, 43:1229–1241, 2005.

E. D. Gutmann, K. M. Larson, M. W. Williams, F. G. Nievinski, and V. Zavorotny. Snow measurement by GPS interferometric reflectometry: an evaluation at Niwot Ridge, Colorado. Hydrological Processes, 26:2951–2961, 2012.

CD Hall and RA Cordey. Multistatic scatterometry. In International Geoscience and Remote Sensing Symposium (IGARSS), IEEE, 'Remote Sensing: Moving Toward the 21st Century'., pages 561–562, 1988.

M. T. Hallikainen, F. T. Ulaby, M. C. Dobson, M. A. Elrayes, and L. K. Wu. Microwave Dielectric Behavior of Wet Soil-part I: Empirical-Models and Experimental-Observations. IEEE Transactions on Geoscience and Remote Sensing, 23:25–34, 1985.

T. J. Jackson and T. J. Schmugge. Vegetation Effects on the Microwave Emission of Soils. Remote Sensing of Environment, 36:203–212, 1991.

T. J. Jackson, R. Bindlish, M. H. Cosh, T. J. Zhao, P. J. Starks, D. D. Bosch, M. Seyfried, M. S. Moran, D. C. Goodrich, Y. H. Kerr, and D. Leroux. Validation of Soil Moisture and Ocean Salinity (SMOS) Soil Moisture Over Watershed Networks in the U.S. IEEE Transactions on Geoscience and Remote Sensing, 50:1530–1543, 2012.

M. D. Jacobson. Dielectric-covered ground reflectors in GPS multipath reception - Theory and measurement. IEEE Geoscience and Remote Sensing Letters, 5:396–399, 2008.

M. D. Jacobson. Inferring Snow Water Equivalent for a Snow-Covered Ground Reflector Using GPS Multipath Signals. Remote Sensing, 2:2426–2441, 2010a.

M. D. Jacobson. Snow-covered lake ice in GPS multipath reception - Theory and measurement. Advances in Space Research, 46:221–227, 2010b.

M. D. Jacobson. Estimating snow water equivalent for a slightly tilted snow-covered prairie grass field by GPS interferometric reflectometry. EURASIP Journal on Advances in Signal Processing, 2014.

M. D. Jacobson. A Case Study for Inferring Freshwater Lake Ice Thickness by GPS Interferometric Reflectometry. Journal of Geography and Geology, 7:10–19, 2015.

S. G. Jin and A. Komjathy. GNSS reflectometry and remote sensing: New objectives and results. Advances in Space Research, 46:111–117, 2010.

S. G. Jin and N. Najibi. Sensing snow height and surface temperature variations in Greenland from GPS reflected signals. Advances in Space Research, 53:1623–1633, 2014.

S. G. Jin, G. P. Feng, and S. Gleason. Remote sensing using GNSS signals: Current status and future directions. Advances in Space Research, 47:1645–1653, 2011.

E. Kaplan and C. Hegarty. Understanding GPS: principles and applications. Artech house, 2005.

S. J. Katzberg, O. Torres, M. S. Grant, and D. Masters. Utilizing calibrated GPS reflected signals to estimate soil reflectivity and dielectric constant: Results from SMEX02. Remote Sensing of Environment, 100:17–28, 2006.

A. Kavak, W. J. Vogel, and G. H. Xu. Using GPS to measure ground complex permittivity. Electronics Letters, 34:254–255, 1998.

Y. Kim, T. Jackson, R. Bindlish, H. Lee, and S. Hong. Radar Vegetation Index for Estimating the Vegetation Water Content of Rice and Soybean. IEEE Geoscience and Remote Sensing Letters, 9:564–568, 2012.

A. Komjathy, J. Maslanik, V. U. Zavorotny, P. Axelrad, and S. J. Katzberg. Sea ice remote sensing using surface reflected GPS signals. In International Geoscience and Remote Sensing Symposium (IGARSS), IEEE, pages 2855–2857, 2000a.

A. Komjathy, V. U. Zavorotny, P. Axelrad, G. H. Born, and J. L. Garrison. GPS signal scattering from sea surface: Wind speed retrieval using experimental data and theoretical model. Remote Sensing of Environment, 73:162–174, 2000b.

A. Komjathy, M. Armatys, D. Masters, P. Axelrad, V. Zavorotny, and S. Katzberg. Retrieval of ocean surface wind speed and wind direction using reflected GPS signals. Journal of Atmospheric and Oceanic Technology, 21:515–526, 2004.

K. M. Larson and F. G. Nievinski. GPS snow sensing: results from the EarthScope Plate Boundary Observatory. GPS Solutions, 17:41–52, 2013.

K. M. Larson and E. E. Small. Normalized Microwave Reflection Index: A Vegetation Measurement Derived From GPS Networks. IEEE Journal of Selected Topics in Applied Earth Observations and Remote Sensing, 7:1501–1511, 2014.

K. M. Larson, E. E. Small, E. Gutmann, A. Bilich, P. Axelrad, and J. Braun. Using GPS multipath to measure soil moisture fluctuations: initial results. GPS Solutions, 12:173–177, 2008a.

K. M. Larson, E. E. Small, E. D. Gutmann, A. L. Bilich, J. J. Braun, and V. U. Zavorotny. Use of GPS receivers as a soil moisture network for water cycle studies. Geophysical Research Letters, 35(24), 2008b.

K. M. Larson, E. D. Gutmann, V. U. Zavorotny, J. J. Braun, M. W. Williams, and F. G. Nievinski. Can we measure snow depth with GPS receivers? Geophysical Research Letters, 36(17), 2009.

K. M. Larson, J. J. Braun, E. E. Small, V. U. Zavorotny, E. D. Gutmann, and A. L. Bilich. GPS Multipath and Its Relation to Near-Surface Soil Moisture Content. IEEE Journal of Selected Topics in Applied Earth Observations and Remote Sensing, 3:91–99, 2010.

K. M. Larson, R. D. Ray, F. G. Nievinski, and J. T. Freymueller. The Accidental Tide Gauge: A GPS Reflection Case Study From Kachemak Bay, Alaska. IEEE Geoscience and Remote Sensing Letters, 10:1200–1204, 2013.

L. Li and S. P. Simonovic. System dynamics model for predicting floods from snowmelt in north american prairie watersheds. Hydrological Processes, 16:2645–2666, 2002.

B. Lin, S. J. Katzberg, J. L. Garrison, and B. A. Wielicki. Relationship between GPS signals reflected from sea surfaces and surface winds: Modeling results and comparisons with aircraft measurements. Journal of Geophysical Research-Oceans, 104:20713–20727, 1999.

J. S. Lofgren, R. Haas, and J. M. Johansson. Monitoring coastal sea level using reflected GNSS signals. Advances in Space Research, 47:213–220, 2011a.

J. S. Lofgren, R. Haas, H. G. Scherneck, and M. S. Bos. Three months of local sea level derived from reflected GNSS signals. Radio Science, 46, 2011b.

N. R. Lomb. Least-Squares Frequency-Analysis of Unequally Spaced Data. Astrophysics and Space Science, 39:447–462, 1976.

M. Marti-Neira. A Passive Reflectometry and Interferometry System (PARIS) - Application to Ocean Altimetry. Esa Journal-European Space Agency, 17:331–355, 1993.

D. Masters, P. Axelrad, and S. Katzberg. Initial results of land-reflected GPS bistatic radar measurements in SMEX02. Remote Sensing of Environment, 92:507–520, 2004.

J. L. McCreight, E. E. Small, and K. M. Larson. Snow depth, density, and SWE estimates derived from GPS reflection data: Validation in the western U.S. Water Resources Research, 50:6892–6909, 2014.

V. L. Mironov, R. D. De Roo, and I. V. Savin. Temperature-Dependable Microwave Dielectric Model for an Arctic Soil. IEEE Transactions on Geoscience and Remote Sensing, 48:2544–2556, 2010.

P. Misra and P. Enge. Global Positioning System: Signals, Measurements and Performance Second Edition. Lincoln, MA: Ganga-Jamuna Press, 2006.

C. Z. Mooney, R. D. Duval, and R. Duval. Bootstrapping: A nonparametric approach to statistical inference. Sage, 1993.

N. Najibi and S. G. Jin. Physical Reflectivity and Polarization Characteristics for Snow and Ice-Covered Surfaces Interacting with GPS Signals. Remote Sensing, 5:4006–4030, 2013.

National Coordination Office. Current and Future Satellite Generations. Website, 2016. URL `http://www.GPS.gov/systems/gps/space/`. checked: 04/11/2016.

F. G. Nievinski and K. M. Larson. Forward modeling of GPS multipath for near-surface reflectometry and positioning applications. GPS Solutions, 18:309–322, 2014a.

F. G. Nievinski and K. M. Larson. Inverse Modeling of GPS Multipath for Snow Depth Estimation-Part I: Formulation and Simulations. IEEE Transactions on Geoscience and Remote Sensing, 52: 6555–6563, 2014b.

F. G. Nievinski and K. M. Larson. Inverse Modeling of GPS Multipath for Snow Depth Estimation-Part II: Application and Validation. IEEE Transactions on Geoscience and Remote Sensing, 52: 6564–6573, 2014c.

F. G. Nievinski and K. M. Larson. An open source GPS multipath simulator in Matlab/Octave. GPS Solutions, 18:473–481, 2014d.

E. G. Njoku and D. Entekhabi. Passive microwave remote sensing of soil moisture. Journal of Hydrology, 184:101–129, 1996.

E. G. Njoku and P. E. Oneill. Multifrequency Microwave Radiometer Measurements of Soil-Moisture. IEEE Transactions on Geoscience and Remote Sensing, 20:468–475, 1982.

E. G. Njoku, W. J. Wilson, S. H. Yueh, S. J. Dinardo, F. K. Li, T. J. Jackson, V. Lakshmi, and J. Bolten. Observations of soil moisture using a passive and active low-frequency microwave airborne sensor during SGP99. IEEE Transactions on Geoscience and Remote Sensing, 40:2659–2673, 2002.

Johan Norberg. GNSS Antenna Comparison for Bistatic Applications. PhD thesis, Lulea University of Technology, 2011.

N. Rodriguez-Alvarez, X. Bosch-Lluis, A. Camps, M. Vall-llossera, E. Valencia, J. F. Marchan-Hernandez, and I. Ramos-Perez. Soil Moisture Retrieval Using GNSS-R Techniques: Experimental Results Over a Bare Soil Field. IEEE Transactions on Geoscience and Remote Sensing, 47: 3616–3624, 2009.

N. Rodriguez-Alvarez, X. Bosch-Lluis, A. Camps, A. Aguasca, M. Vall-Ilossera, E. Valencia, I. Ramos-Perez, and H. Park. Review of crop growth and soil moisture monitoring from a ground-based instrument implementing the Interference Pattern GNSS-R Technique. Radio Science, 46, 2011a.

N. Rodriguez-Alvarez, A. Camps, M. Vall-llossera, X. Bosch-Lluis, A. Monerris, I. Ramos-Perez, E. Valencia, J. F. Marchan-Hernandez, J. Martinez-Fernandez, G. Baroncini-Turricchia, C. Perez-Gutierrez, and N. Sanchez. Land Geophysical Parameters Retrieval Using the Interference Pattern GNSS-R Technique. IEEE Transactions on Geoscience and Remote Sensing, 49:71–84, 2011b.

N. Rodriguez-Alvarez, A. Aguasca, E. Valencia, X. Bosch-Lluis, A. Camps, I. Ramos-Perez, H. Park, and M. Vall-Llossera. Snow Thickness Monitoring Using GNSS Measurements. IEEE Geoscience and Remote Sensing Letters, 9:1109–1113, 2012a.

N. Rodriguez-Alvarez, X. Bosch-Lluis, A. Camps, I. Ramos-Perez, E. Valencia, H. Park, and M. Vall-llossera. Vegetation Water Content Estimation Using GNSS Measurements. IEEE Geoscience and Remote Sensing Letters, 9:282–286, 2012b.

G. Ruffini, F. Soulat, M. Caparrini, O. Germain, and M. Martin-Neira. The Eddy Experiment: Accurate GNSS-R ocean altimetry from low altitude aircraft. Geophysical Research Letters, 31 (12), 2004.

J. C. Shi and J. Dozier. Estimation of snow water equivalence using SIR-C/X-SAR, part I: Inferring snow density and subsurface properties. IEEE Transactions on Geoscience and Remote Sensing, 38:2465–2474, 2000a.

J. C. Shi and J. Dozier. Estimation of snow water equivalence using SIR-C/X-SAR, part II: Inferring snow depth and particle size. IEEE Transactions on Geoscience and Remote Sensing, 38:2475–2488, 2000b.

S. Sitch, C. Huntingford, N. Gedney, P. E. Levy, M. Lomas, S. L. Piao, R. Betts, P. Ciais, P. Cox, P. Friedlingstein, C. D. Jones, I. C. Prentice, and F. I. Woodward. Evaluation of the terrestrial carbon cycle, future plant geography and climate-carbon cycle feedbacks using five Dynamic Global Vegetation Models (dgvms). Global Change Biology, 14:2015–2039, 2008.

E. E. Small, K. M. Larson, and J. J. Braun. Sensing vegetation growth with reflected GPS signals. Geophysical Research Letters, 37(12), 2010.

E. E. Small, K. M. Larson, and W. K. Smith. Normalized Microwave Reflection Index: Validation of Vegetation Water Content Estimates From Montana Grasslands. IEEE Journal of Selected Topics in Applied Earth Observations and Remote Sensing, 7:1512–1521, 2014.

F. Soulat, M. Caparrini, O. Germain, P. Lopez-Dekker, M. Taani, and G. Ruffini. Sea state monitoring using coastal GNSS-R. Geophysical Research Letters, 31(21), 2004.

M. E. Tiuri, A. H. Sihvola, E. G. Nyfors, and M. T. Hallikainen. The Complex Dielectric-Constant of Snow at Microwave-Frequencies. IEEE Journal of Oceanic Engineering, 9:377–382, 1984.

F. T. Ulaby and M. A. Elrayes. Microwave Dielectric Spectrum of Vegetation-part II: Dual-Dispersion Model. IEEE Transactions on Geoscience and Remote Sensing, 25:550–557, 1987.

F. T. Ulaby and E. A. Wilson. Microwave Attenuation Properties of Vegetation Canopies. IEEE Transactions on Geoscience and Remote Sensing, 23:746–753, 1985.

W. Wan, K. M. Larson, E. E. Small, C. C. Chew, and J. J. Braun. Using geodetic GPS receivers to measure vegetation water content. GPS Solutions, 19:237–248, 2015.

J. R. Wang and T. J. Schmugge. An Empirical-Model for the Complex Dielectric Permittivity of Soils as a Function of Water-Content. IEEE Transactions on Geoscience and Remote Sensing, 18:288–295, 1980.

A. W. Western, S. L. Zhou, R. B. Grayson, T. A. McMahon, G. Bloschl, and D. J. Wilson. Spatial correlation of soil moisture in small catchments and its relationship to dominant spatial hydrological processes. Journal of Hydrology, 286:113–134, 2004.

Wikipedia. Radiation pattern of antenna. Website. URL `https://en.wikipedia.org/wiki/RadiationPattern`. checked: 04/11/2016.

V. Zavorotny, D. Masters, A. Gasiewski, B. Bartram, S. Katzberg, P. Axelrad, and R. Zamora. Seasonal polarimetric measurements of soil moisture using tower-based GPS bistatic radar. Igarss 2003: IEEE International Geoscience and Remote Sensing Symposium, Vols I - Vii, Proceedings, pages 781–783, 2003.

V. U. Zavorotny and A. G. Voronovich. Bistatic GPS signal reflections at various polarizations from rough land surface with moisture content. In International Geoscience and Remote Sensing Symposium (IGARSS), IEEE, pages 2852–2854, 2000a.

V. U. Zavorotny and A. G. Voronovich. Scattering of GPS signals from the ocean with wind remote sensing application. IEEE Transactions on Geoscience and Remote Sensing, 38:951–964, 2000b.

V. U. Zavorotny, K. M. Larson, J. J. Braun, E. E. Small, E. D. Gutmann, and A. L. Bilich. A Physical Model for GPS Multipath Caused by Land Reflections: Toward Bare Soil Moisture Retrievals. IEEE Journal of Selected Topics in Applied Earth Observations and Remote Sensing, 3:100–110, 2010.